TECHNISCHE UNIVERSITÄT MÜNCHEN
TUM School of Medicine and Health

# Increased claustrum volume and aberrant microstructure in preterm-born neonates

Antonia Dorothea Neubauer

Vollständiger Abdruck der von der TUM School of Medicine and Health
der Technischen Universität München
zur Erlangung einer Doktorin der Medizin (Dr. med.)
genehmigten Dissertation.

Vorsitz: Prof. Dr. Lutz Renders

Prüfende der Dissertation:

1. Priv.-Doz. Dr. Christian Franz Sorg
2. apl. Prof. Dr. Esther Rieger-Fackeldey, Ph.D.
3. apl. Prof. Dr. Mark Mühlau

Die Dissertation wurde am 20.02.2024 bei der Technischen Universität München eingereicht und durch die TUM School of Medicine and Health am 07.08.2024 angenommen.

## Abstract

The human claustrum is a small, highly connected gray matter structure in the forebrain between insula and putamen. The claustrum development overlaps with subplate neurons and pre-oligodendrocytes. As both transient cell populations are highly vulnerable to hypoxic-ischemic events related to preterm birth, the claustrum might also be at risk. While an impaired claustrum microstructure was shown in preterm-born adults, this study examined the claustrum structure in neonates.

To achieve automated claustrum segmentation in T2-weighted neonatal brain MRI, a deep learning approach was developed by transfer learning from adult scans. Data between gestational age 29.3 to 45.1 weeks were provided by the developing Human Connectome Project. The model was trained on 20 manual segmentations, tested on ten subjects, and applied in 528 scans which passed visual control afterwards. We evaluated the claustrum development and impact of preterm birth regarding the following metrics: macrostructure in terms of absolute and total brain volume (TBV-) relative claustrum volume, microstructure in terms of mean diffusivity (MD) and fractional anisotropy (FA), and structural covariance with other brain regions. To compare preterm- and term-born neonates, 83 subjects of each group were opposed under age-equivalent conditions.

Automated segmentation achieved a median Dice similarity coefficient of 80.0 %, a volumetric similarity of 95.9 %, and a Hausdorff distance of 1.12 mm, which was significantly superior to inter-rater reliability regarding Dice similarity coefficient ($p < 0.005$) and volumetric similarity ($p = 0.047$), indicating an accurate and efficient approach. Codes and models were published on GitHub. We found that the absolute ($p < 0.001$) and TBV-relative claustrum volume ($p = 0.029$) were significantly increased in preterm-born neonates. While the claustrum MD was significantly increased ($p = 0.004$), the claustrum FA was significantly decreased ($p < 0.001$) after preterm birth. The microstructural covariance was partly altered in subcortical and cortical regions.

To conclude, preterm birth lead to impaired claustrum structure and aberrant proportions suggesting an altered development. The volume increase combined with scattered microstructure might refer to increased extracellular matrix and aberrant connectivity with possible clinical relevance for cognitive performance.

## Zusammenfassung

Das menschliche Claustrum ist ein schmales, stark vernetztes Kerngebiet im Vorderhirn zwischen Inselrinde und Putamen. Die Claustrumentwicklung überschneidet sich mit transienten Zellpopulationen wie Subplateneuronen und Präoligodendrozyten. Da beide Populationen vulnerabel gegenüber Hypoxie und Ischämie bei Frühgeburtlichkeit sind, ist möglicherweise auch das Claustrum gefährdet. So wurde im Claustrum frühgeborener Erwachsener eine veränderte Mikrostruktur nachgewiesen. Diese Studie untersucht das Claustrum in Neugeborenen.

Um die Claustrumsegmentierung in T2-gewichteten Neugeborenen-MRTs zu automatisieren, haben wir eine Künstliche Intelligenz (KI) über Transferlernen von Erwachsenenscans entwickelt. Die Daten des developing Human Connectome Projects umfassen Scans von der 29.3 zur 45.1 Schwangerschaftswoche. Die KI wurde mit 20 manuellen Segmentierungen trainiert, mit zehn Scans getestet und an 528 Scans mit anschließender visueller Kontrolle angewandt. Die Claustrumentwicklung und der Einfluss von Frühgeburtlichkeit wurden anhand folgender Werte untersucht: das absolute und relative Claustrumvolumen im Verhältnis zum totalen Gehirnvolumen (TBV); die Mikrostruktur anhand der durchschnittlichen Diffusivität (mean diffusivity = MD) und der fraktionellen Anisotropie (FA); die Kovarianz mit anderen Gehirnregionen. Jeweils 83 Früh- und Termgeborene wurden unter altersäquivalenten Bedingungen verglichen.

Die KI erreichte einen medianen Dice Similarity Coefficient von 80,0 %, eine Volumenübereinstimmung von 95,9 % und eine Hausdorff Distance von 1,12 mm und war damit signifikant besser als die Inter-rater Reliabilität bezüglich Dice Similarity Coefficient ($p < 0.005$) und Volumenübereinstimmung ($p = 0.047$). Der Code ist auf GitHub verfügbar. Das absolute ($p < 0.001$) und TBV-relative Claustrumvolumen ($p = 0.029$) waren in Frühgeborenen signifikant vergrößert, die Claustrum-MD war signifikant erhöht ($p = 0.004$) und die Claustrum-FA signifikant erniedrigt ($p < 0.001$). Die mikrostrukturelle Kovarianz war in Teilen der subcortikalen und cortikalen Regionen verändert.

Frühgeburtlichkeit führte zu einer veränderten Claustrumstruktur und Kovarianz mit anderen Regionen, die auf eine abweichende Entwicklung hinweisen kann. Die Volumenzunahme zusammen mit der aufgelockerten Mikrostruktur können durch eine Zunahme der Extrazellulärmatrix und veränderte Konnektivität zustande kommen, die möglicherweise eine klinische Konsequenz im Rahmen der kognitiven Entwicklung haben können.

## Table of contents

## List of Tables

## List of Figures

## List of abbreviations

| | |
|---|---|
| AI | Artificial intelligence |
| CC By | Creative Commons Attribution 4.0 International (https://creativecommons.org/licenses/by/4.0/) |
| CNN | Convolutional neural network |
| CPU | Central processing unit |
| DA | Data augmentation |
| dHCP | Developing Human Connectome Project |
| dMRI | Diffusion-weighted magnetic resonance imaging |
| Draw-EM | Developing brain Region Annotation With Expectation-Maximization |
| DSC | Dice similarity coefficient |
| FA | Fractional anisotropy |
| FDR | False discovery rate |
| FT | Full term-born subjects |
| GA | Gestational age in weeks |
| GABA | γ-aminobutyric acid |
| GLM | General linear model |
| GM | Gray matter |
| GPU | Graphics processing unit |
| HD95 | 95th percentile of the Hausdorff distance |
| HI | Hypoxia-ischemia |
| IQR | Interquartile range |
| KI | Künstliche Intelligenz |
| MD | Mean Diffusivity |
| MRI | Magnetic resonance imaging |
| non-TL | Non-transfer learning |
| OL | Oligodendrocyte |
| pre-OL | Pre-oligodendrocyte |
| PT | Preterm-born subjects |
| QC | Quality control |
| ReLU | Rectified linear unit |
| SD | Standard deviation |
| SPN | Subplate neuron |
| T1w | T1-weighted |
| T2w | T2-weighted |
| TBV | Total brain volume |
| TE | Echo time |
| TL | Transfer learning |
| TR | Repetition time |
| VS | Volumetric similarity |
| WM | White matter |

# 1 Introduction

The claustrum, a small, subcortical gray matter structure of the forebrain, is difficult to access for research because of its size and intricate shape. With improved technical capabilities like high image resolution and computational power for deep learning approaches in radiology, the claustrum became available in large-scale imaging studies. In the following, the importance of the claustrum, background knowledge about brain development in general and claustrum maturation in particular, and the relevance and adverse impact of preterm birth will be presented. The basics of MRI techniques and artificial intelligence are explained.

The study is composed of two parts, first, the implementation of automated claustrum segmentation in neonatal brain MRI by deep learning and transfer learning, and second, the analysis of the segmentations regarding claustrum development and comparison of claustrum macro- and microstructure in preterm- and term-born neonates. Finally, a brief combined discussion and conclusion are given. To the best of our knowledge, this project examined the effect of preterm birth on the claustrum structure in newborns for the first time.

## 1.1 The claustrum

The claustrum is a small brain structure named for "hidden away" or the Latin form of "enclosure" (Bruguier et al., 2020; Crick and Koch, 2005). Although the claustrum was already described in the middle of the 18th century by Félix Vicq d’Azyr, its role is not fully understood (Crick and Koch, 2005; Johnson and Fenske, 2014; Smith et al., 2020). This section will give an overview of the current knowledge about the claustrum anatomy and function. The claustrum development will be discussed in the context of brain development in section 1.2.4.

### 1.1.1 Claustrum anatomy and physiology

The claustrum is a small, sheet-like gray matter structure of the mammalian forebrain between insula and striatum surrounded by white matter, namely the external and extreme capsule (Puelles, 2014) (Figures 1 and 2). A correlate in reptiles and birds is debatable (Puelles, 2014; Watson and Puelles, 2017). The claustrum can be subdivided into different parts based on gene expression patterns: first, the bigger principal claustrum is lying under the insular cortex comprising a smaller subplate part that lies a bit deeper than the residual part (Watson and Puelles, 2017); second, the dorsal endopiriform nucleus also described as ventral claustrum was recently defined as part of the claustrum complex (Smith et al., 2020, 2018). These

regions share genetic markers like Nurr1, Nr4a2, and Gng2 (Arimatsu et al., 2003; Mathur, 2014; Smith et al., 2018; Watson and Puelles, 2017) while the ventral endopiriform nucleus expresses other genes (Smith et al., 2018).

The claustrum microstructure is composed of fibers and cell bodies without a clear border to the surrounding white matter and is traversed by fiber tracts (Bernstein et al., 2016; Mathur, 2014). The cells show different forms from ovoid to polygonal somata and comprise two main neuron types, around 85 % glutamatergic projection neurons and around 15 % aspiny, GABAergic interneurons (Goll et al., 2015; Mathur, 2014). Interneurons can be further distinguished by the expression of proteins like parvalbumin and calbindin (Bruguier et al., 2020). The projection neurons show connections mainly to cortical interneurons, and some to other projection neurons in the cortex, probably in the frame of a feedforward inhibition (Goll et al., 2015). Besides glutamate and GABA, serotonin might also play a role as a transmitter (Baizer, 2001; Barrett et al., 2020; Mathur, 2014). The claustrum gets glutamatergic input from cortical layer 6 and probably also from layers 2-5 to interneurons and projection cells (Benarroch, 2021; Smith et al., 2018). Its own projection neurons innervate all cortical layers (Smith et al., 2018) or at least layers 1, 4, and 6 (Benarroch, 2021).

In relation to its volume, the claustrum is the best connected region of the brain (Torgerson et al., 2015). In detail, the claustrum is organized dorso-ventrally in functional zones: each part shows intra-segmental connectivity and is connected reciprocally to specific cortical regions (Jackson et al., 2020; Milardi et al., 2015). While the dorsal part is linked to sensory-motor areas, the middle and ventral parts, including the dorsal endopiriform nucleus, are more strongly connected to the prefrontal associative cortex and to the cingulate gyrus as part of the limbic system (Jackson et al., 2020; Milardi et al., 2015; Smith et al., 2018; White et al., 2018). In addition, the claustrum receives input from limbic structures like the hippocampus and amygdala as well as the thalamus and dorsal raphe (Jackson et al., 2020; Mathur, 2014). Potentially, there is a connectivity circuit from associative and limbic cortical areas to the contralateral claustrum and from the latter to the ipsilateral cortex (Mathur, 2014; Smith et al., 2018). Interclaustral connections are also described (Milardi et al., 2015). A strong structural connection to the overlying anterior insula was refused in recent studies (Qadir et al., 2018; Watson and Puelles, 2017). Though, connections between the dorsal endopiriform nucleus and anterior insula were described (Qadir et al., 2018).

Due to its small volume and intricate structure, the claustrum is not mentioned in common brain atlases for MRI application (Makropoulos et al., 2014, 2018a).

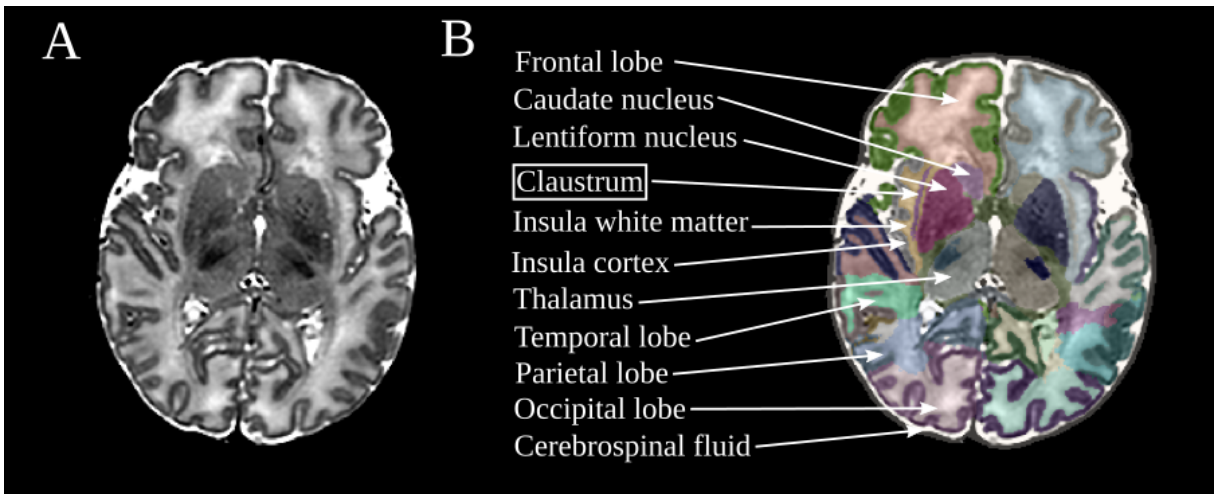


***Figure 1: Brain of a term-born male newborn.***

*(A) shows an axial slice of a T2-weighted MRI scanned at the gestational age of 41 weeks. (B) shows the same slice with overlaid labels of the Draw-EM atlas and a prepared claustrum segmentation with labels for the right hemisphere.*

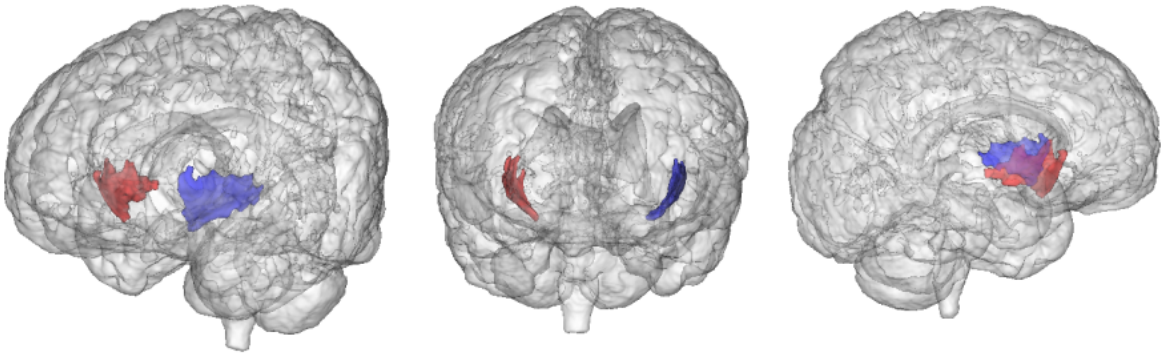

***Figure 2: Model of the claustrum in a transparent brain of a term-born male newborn.***

*From left to right, the brain, scanned at the gestational age of 38 weeks, is shown from the left front, from the front, and the right side. Thus, the red claustrum is the right one, and the blue claustrum is the left one.*

### 1.1.2 Claustrum function

The claustrum function is still speculative (Smith et al., 2020). Due to the exceptional connectivity, Crick and Koch suggested a role in consciousness (2005). Several studies proposed the claustrum as a region of multisensory integration (Reviewed in Mathur, 2014) or as a coordinator of cortical areas (Smith et al., 2012). Recent studies outline two non-exclusive functional domains: On the one hand, the claustrum could play a role in attention

and arousal modulation (Goll et al., 2015; Mathur, 2014; Smith et al., 2020; White et al., 2018). It is active in task-switching and attention-guiding processes as a potential part of the salience network (Jackson et al., 2020; Krimmel et al., 2019). The cingulate-claustrum connection was more active in sophisticated tasks, suggesting a task-load-dependent effect on top-down action control (White et al., 2018). The claustrum could suppress distracting stimuli by its inhibitory impact on the cortex (Smith et al., 2020).

On the other hand, the claustrum might play a role in slow-wave sleep coordination (Narikiyo et al., 2020; Smith et al., 2020). Narikiyo et al. (2020) observed a higher claustrum activity during slow-wave sleep and impaired slow-wave sleep in animals with altered claustrum, indicating a modulatory effect.

From a clinical point of view, the claustrum might play a role in mental, neurological, and developmental disorders (Torgerson et al., 2015). There is evidence for an altered claustrum structure in patients with schizophrenia (Bernstein et al., 2016). The claustrum might also be affected in autism (Davis, 2008). Moreover, several studies proposed an association with epileptic seizures (Reviewed in Benarroch, 2021; Kurada et al., 2019). Finally, the claustrum microstructure is aberrant in very preterm-born adults associated with lower cognitive performance (Hedderich et al., 2021). These findings support a basic cognitive and clinically relevant function of the claustrum.

## 1.2 Brain development

The brain changes over the whole lifespan (Courchesne et al., 2000). The following sections focus on the early stages starting from intra-uterine brain maturation, further postnatal development, important transient cell populations, and early claustrum development.

### 1.2.1 Intra-uterine brain maturation

The time of gestation is partitioned into two intervals, the embryonic and fetal phases. While the embryonic phase covers the first eight post-conceptional weeks (equals the period till GA 10 weeks), the fetal period lasts for around 30 weeks.

At day 13 of the embryonic phase, E13, a rostro-caudal structure is present in a two-layered embryo and gastrulation starts. This process results in a three-layered embryo composed of entoderm, mesoderm, and ectoderm, while ectodermic cells in the midline will develop into neural progenitors guided by gene expression patterns. Subsequently, neurulation takes place or more specifically the neuronal plate develops a fold which becomes a groove, and finally a

tube with closed pores at the end of the third post-conceptional week. Overlapping with neurulation, this tube starts to form brain vesicles: pros-, mes- and rhombencephalon. The first will further divide into tel- and diencephalon and the last will differentiate into met- and myelencephalon. The cavity within the vesicles will become the ventricular system. The first excitatory neurons are produced around E42 in the ventricular system while inhibitory cortical interneurons arise in the ganglionic eminences. At the end of the embryonic phase, a basic brain organization with several regions is established conducted by protein gradients. (Stiles and Jernigan, 2010)

The gyrification starts in the fetal period and continues after birth (Stiles and Jernigan, 2010; Zilles et al., 2013): The first emerging sulci, after the fissura longitudinalis cerebri, are primary sulci in primary cortices followed by secondary sulci in associative cortices and finally tertiary sulci to increase the brain surface. Simultaneously, the microscopic maturation proceeds. Two directions dominate cellular migration in the developing brain, radial and tangential trajectories (Raybaud et al., 2013; Stiles and Jernigan, 2010). The radial migration consists of neurons from the ventricular zone to the cortex guided by a scaffolding of radial glial cells (Stiles and Jernigan, 2010). The tangential trajectory is populated by cells from the ganglionic eminences to the cortex or basal ganglia guided by molecule levels (McQuillen and Ferriero, 2005; Stiles and Jernigan, 2010). When these cells arrived in the cortex, they differentiate and their axons and dendrites grow (Stiles and Jernigan, 2010). Beyond that, there are smaller tracks, e.g., cells transfer from the claustrum anlage in the lateral pallium to the dorsal endopiriform nucleus in the ventral pallium or into the subplate (Watson and Puelles, 2017).

Regarding the developing brain in the coronal view, there appears a cellular stratification. These layers emerge from the inner to outer position (Hoerder-Suabedissen and Molnár, 2015): Ventricular zone, subventricular zone, intermediate zone and subplate, cortical plate, and marginal zone. Thereby, the cortical layers are formed from the inner to outer position (VI-I) conducted by Cajal-Retzius cells (Stiles and Jernigan, 2010). Around or more than 50 % of all neurons will die physiologically by programmed cell death (Stiles and Jernigan, 2010).

In another classification, the telencephalon is divided into pallium and subpallium which are precursors of later cortical and subcortical structures with minor mingling. The pallium is organized in four rings: medial pallium directly next to the fissura longitudinalis cerebri

between the two hemispheres; dorsal pallium which occupies the largest part of the prospective telencephalon; lateral pallium as the origin of the claustrum anlage together with some subplate neurons, insular cortex, and dorsal endopiriform nucleus; finally, the ventral pallium as an antecedent of the ventral endopiriform nucleus and the olfactory cortex. (Binks et al., 2019)

Regarding brain connectivity, cortico-thalamic connections develop at gestational age (GA, also called post-menstrual age) 12-20 weeks guided by subplate neurons (Hoerder-Suabedissen and Molnár, 2015; McQuillen and Ferriero, 2005). The maturation of axons also depends on the proper differentiation of oligodendrocytes (Volpe, 2019). The role of the subplate neurons and (pre-)oligodendrocytes will be explained in more detail in section 1.2.3. The functional connectivity patterns including the default mode network exist already in neonates at term before functional maturation is finished (Doria et al., 2010).

### 1.2.2 Postnatal brain development

Brain development continues after birth. In the early postnatal period, there is still a high proliferation of glial progenitors which will become astrocytes and oligodendrocytes. These cells interact reciprocally with neurons, influencing axonal integration and cell survival. On the one hand, axons start abundant connections with their environment, and on the other hand, a selection takes place so that up to 50 % of connections and glial cells disappear. Concurrently, the connectivity, cell proliferation and death, and the maturation of the vascular system are influenced by the sensory input of the newborn. The genesis of neurons is reduced to minimal cell formation in the subventricular zone and dentate gyrus. Transient cell populations like the marginal zone, the subplate, and neuronal progenitors dissolve. In summary, the networks develop into individual, more functional neuronal circuits. (Stiles and Jernigan, 2010)

Brain development appears during the whole life span. The total brain volume increases till around 13 years (Backhausen et al., 2021; Bethlehem et al., 2022). While the white matter volume increases for several decades, probably due to myelination, cortical and some subcortical gray matter regions decrease from childhood to adulthood (Backhausen et al., 2021; Stiles and Jernigan, 2010).

### 1.2.3 Transient cell populations

Two large transient cell populations, subplate neurons (SPNs) and pre-oligodendrocytes (pre-OLs), appear in the intra-uterine developing brain and play a vital role in the pre- and perinatal period (Hoerder-Suabedissen and Molnár, 2015; Volpe, 2019, 1996). Their development is closely related to the claustrum development (see section 1.2.4).

#### 1.2.3.1 Subplate neurons

The subplate is a transient structure of brain maturation that forms a layer directly under the cortex (sub-plate). Subplate neurons (SPNs) rank among the earliest born cell populations (Hoerder-Suabedissen and Molnár, 2015). The excitatory cells emerge in the ventricular zone, probably in the subventricular zone, and GABAergic SPNs arise in the ganglionic eminence and the rostro-medial telencephalic wall is also discussed as an origin (Hoerder-Suabedissen and Molnár, 2015; McQuillen and Ferriero, 2005). A vague initiation of the subplate starts at around the GA of 12 weeks in terms of a presubplate stage as a cell-sparse, heterogeneous layer together with the marginal zone (Hoerder-Suabedissen and Molnár, 2015; Kostovic and Rakic, 1990). The proper subplate formation follows on till around GA 13 with an upper, fiber- and cell rich part and a lower cell-sparse part (Hoerder-Suabedissen and Molnár, 2015; Kostovic and Rakic, 1990). Thereafter, the subplate increases further, achieves its largest extent till around GA 20, and gets more differentiated till around GA 35 (Kostovic and Rakic, 1990). The increase is dominated by axonal ingrowth leading to a subplate size four times larger than the cortex (Hoerder-Suabedissen and Molnár, 2015; Kostovic and Rakic, 1990). After GA 35, the subplate starts to dissolve over a couple of months by programmed cell death which might be induced by retraction of connectivity and changed gene expression (Hoerder-Suabedissen and Molnár, 2015; Luhmann et al., 2018). It seems likely that some neurons to an unknown extent survive as interstitial white matter cells (Luhmann et al., 2018). On a cellular level, the subplate is very heterogeneous and contains fibers, an extensive extracellular matrix, neurons, and immature glial cells (Hoerder-Suabedissen and Molnár, 2015; Luhmann et al., 2018, 2009). SPNs mainly receive glutamatergic and GABAergic input, they are partly modulated by a cholinergic system and might also express receptors for glycine, dopamine, serotonin, and several neuropeptides (Barrett et al., 2020; Kanold and Luhmann, 2010; Luhmann et al., 2018). Furthermore, the subplate includes radially and tangentially migrating neurons on their way to a cortical destination (Hoerder-Suabedissen and Molnár, 2015; Luhmann et al., 2018).

The subplate plays an important role in brain maturation. SPNs guide the ingrowth of thalamic afferents into the cortex (Hoerder-Suabedissen and Molnár, 2015; Kanold and Luhmann, 2010). In detail, thalamic axons connect temporarily to SPNs as the cortex, including the destination layer 4, is formed later and will be transiently connected to SPNs, too (Ghosh et al., 1990). Around GA 30, this interconnection via SPNs is gradually replaced by direct connections between thalamic and cortical neurons (Kostović and Judaš, 2010). Moreover, glutamatergic projection neurons of the subplate influence neurons, which migrate radially to the cortex, and they induce the maturation of inhibitory connections in the cortex (Kanold and Shatz, 2006; Luhmann et al., 2018) while GABAergic SPNs synchronize the cortical activity (Kanold and Luhmann, 2010). Thereby, the subplate integrates spontaneous and sensory-driven activity in the maturation of thalamo-cortical, cortico-thalamic, and intra-cortical connections (Molnár et al., 2020). Moreover, the maturation of cortical columns depends on SPNs, e.g., in the primary visual cortex (Kanold and Luhmann, 2010; Kanold and Shatz, 2006). SPNs also prohibit an excretory function of extracellular matrix promoting cortical pathfinding (Hoerder-Suabedissen and Molnár, 2015). As mentioned above, most of the SPNs will dissolve by apoptosis and the function of the remaining neurons is still unclear but a role in psychiatric disorders was proposed (Hoerder-Suabedissen and Molnár, 2015). The consequences of an impaired subplate will be discussed in section 1.3.2.

#### 1.2.3.2 Pre-oligodendrocytes

The second large transient cell population comprises pre-oligodendrocytes (pre-OL). The progenitors of this lineage are visible at GA 20-24 weeks (Volpe, 2019). These cells develop to pre-OLs with a peak amount around GA 24-32 (Back et al., 2001). At term, 50 % of pre-OLs became immature oligodendrocytes (OLs) which start axon ensheathment at GA 30 (Volpe, 2019). Pre-OLs are postmigratory cells that are able to proliferate (Back, 2017). Post-term, these cells differentiate to mature OLs which provide myelination sheets around axons for a higher nerve conduction velocity (Volpe, 2019). Thus, this cell population is important for axon maturation and correct cortical development as well as gray matter development in a secondary effect (Kinney and Volpe, 2018; Volpe, 2019). The consequences of impaired pre-OLs will be discussed in section 1.3.2.

### 1.2.4 Claustrum development in the context of subplate neurons and pre-oligodendrocytes

The claustrum, a small gray matter structure of the forebrain, is a derivative of the lateral pallium (Binks et al., 2019; Watson and Puelles, 2017). Detected in animal studies, excitatory claustrum cells emerge relatively early during brain maturation in the ventricular zone and reach the claustrum primordium via radial migration (Hoerder-Suabedissen and Molnár, 2015; Puelles, 2014; Watson and Puelles, 2017). The inhibitory interneurons might arise subpallially (Puelles, 2014), probably in the ganglionic eminence like cortical inhibitory neurons (McQuillen and Ferriero, 2005).

The claustrum primordium acts as an origin of four cellular migration trajectories (Puelles, 2014): First, some cells of the claustrum migrate ventrally and form the dorsal endopiriform nucleus (Binks et al., 2019; Watson and Puelles, 2017). This nucleus settles in the ventral pallium next to the ventral endopiriform nucleus which is a derivative of the ventral pallium itself (Watson and Puelles, 2017); second, some cells form the caudal endopiriform nucleus; third, there are hints of a tangentially migratory flow from the early claustrum to the subplate region (Watson and Puelles, 2017); fourth, Arimatsu cells transfer to the parietal cortex (Puelles, 2014).

Subsequently, younger cells migrate radially through the claustrum anlage to form the insular cortex (Puelles, 2014; Watson and Puelles, 2017). This progress leads to a passive displacement of the superficial claustrum primordium to a subcortical location (Watson and Puelles, 2017). Earlier assumptions that claustrum and insula belong to the same structure were refused because of separated circuitries, orthogonal dendritic organization, distinct gene expression patterns, i.e., claustrum specific markers (Nr4a2, Gng2, and Cbln2) instead of typical layer 6a marker (Rprm) in the claustrum neurons, and the formation of the extreme capsule, an interjacent range of white matter between claustrum and insula, in some species like humans (Puelles, 2014).

The claustrum development is interconnected with two transient cell populations, namely subplate neurons (SPN) and pre-oligodendrocytes (pre-OL). The claustrum is related to SPNs at various levels: The subplate plays a vital role in the formation of connections and cortical organization (Hoerder-Suabedissen and Molnár, 2015; Kanold and Luhmann, 2010; Luhmann et al., 2018). There is little knowledge about the development of claustral connections but the claustrum is highly connected to cortical regions, suggesting that claustrum maturation might

be directly or indirectly dependent on SPNs by developing connectome coordination (Bruguier et al., 2020). Second, the claustrum and subplate share some characteristics. Both structures contain very early-born cell populations in comparison with other neurons of the same compartment, respectively (Bruguier et al., 2020; Hoerder-Suabedissen and Molnár, 2015; Watson and Puelles, 2017). The cells partly share gene expression patterns like Nr4a2/Nurr1 and Satb2 whereby the exact genes depend on the species (Bruguier et al., 2020; Watson and Puelles, 2017). Additionally, the microstructure of the claustrum and subplate have in common that both contain glutamatergic projection neurons to spread cortical and subcortical regions and GABAergic interneurons (Bruguier et al., 2020; Hoerder-Suabedissen and Molnár, 2015; Luhmann et al., 2018; Milardi et al., 2015; Torgerson et al., 2015). Furthermore, the smaller, medial part of the claustrum is also called subplate part due to the distinct expression of markers like in the proper subplate (Bruguier et al., 2020; Puelles, 2014; Watson and Puelles, 2017). As mentioned above, some claustral cells seem to migrate tangentially into the subplate (Watson and Puelles, 2017). At this juncture, it is not clear whether or to what extent claustrum neurons undergo programmed cell death like SPNs (Bruguier et al., 2020). To sum up, claustrum and subplate development and properties are closely related suggesting a mutual evolutionary origin of both structures (Bruguier et al., 2020).

The second important transient cell population is pre-OLs. This cell row is notable for white matter maturation (Volpe, 2019). However, they are likely relevant for the physiological development of the up- and downstream connected gray matter regions, too (Kinney and Volpe, 2018). Thus, the highly connected claustrum is probably also depending on pre-OLs (Hedderich et al., 2021).

## 1.3 Prematurity

Preterm birth pathologically terminates intra-uterine development too early. It is a frequent incident related to risks for various short and long-term effects described in the following.

### 1.3.1 Prevalence and causes

Preterm birth is defined as a live birth before the GA of 37 weeks is completed (Blencowe et al., 2012; WHO, 2012; Volpe, 2019). Very preterm means birth before GA 32 and extreme preterm means birth before GA 28 (Blencowe et al., 2012). Term-born neonates are born between GA 37 and 42 weeks and a birth GA ≥42 weeks is called post-term (Blencowe et al.,

2012). With a worldwide prevalence of around 11 %, prematurity affects around 15 million newborns per year (Blencowe et al., 2013, 2012; Chawanpaiboon et al., 2019; Purisch and Gyamfi-Bannerman, 2017). While some northern European countries show a frequency of 5 % preterm births, lower-income countries tend to have a higher rate (Blencowe et al., 2012). Based on medical advances like newborn intensive care units, the number of surviving preterm-born neonates increased over the last 50 years and the minimal duration of gestation with long-term newborn survival decreased to a survival rate of 50 % at GA 23 to 24 weeks (Glass et al., 2015).

Preterm births can be caused by spontaneous or provider-initiated reasons like fetal or maternal indication (Blencowe et al., 2012; Purisch and Gyamfi-Bannerman, 2017). Several studies examined risk factors of preterm birth and observed an association with a family history of previous preterm births, preterm labor, multiple pregnancy, artificial reproductive technologies, maternal anatomical conditions, e.g., uterine anomalies or shortened cervical length, maternal circumstances like smoking, low socioeconomic status, black race, low body mass index or higher age, pathological influences like the hypertensive disease of pregnancy, intrauterine growth restriction or infections, and low paternal age (Blencowe et al., 2012; Goldenberg et al., 2008; Purisch and Gyamfi-Bannerman, 2017; Sartorius and Nieschlag, 2010). However, preterm birth also emerges without known risk factors (Purisch and Gyamfi-Bannerman, 2017).

### 1.3.2 Consequences of preterm birth

Preterm birth is a risk factor for various short- and long-term complications described in the following. A brief insight into therapeutic options is given afterwards.

#### 1.3.2.1 Acute problems after preterm birth

Prematurity leads to infant morbidity and death: It contributes to 75 % of all deaths in the neonatal period and there is a correlation between lower birth age and inferior prospects (Purisch and Gyamfi-Bannerman, 2017; Volpe, 2019). Birth at GA 32 weeks occurs with around 95 % survival and birth at GA 24 weeks with around 63 % (Volpe, 2019). Apart from that, preterm birth is related to morbidity, e.g., hemorrhagic events, hypoxia-ischemia (HI), infection, e.g., sepsis or necrotizing enterocolitis, bronchopulmonary dysplasia leading to a respiratory distress syndrome, and retinopathy as a possible long-term consequence (Purisch and Gyamfi-Bannerman, 2017; Twilhaar et al., 2018b). HI accounts for the largest fraction of

neonatal deaths (Millar et al., 2017). Adverse environmental conditions encompass, e.g., stress exposure in intensive care units and malnutrition (Twilhaar et al., 2018b).

Millar et al. (2017) proposed three pathophysiological pathways: First, an excitotoxic process might cause cell death by glutamate guided over-activation of cells, procured by receptors like NMDA and AMPA. Second, oxidative stress lowers energy availability resulting in higher intracellular calcium and free radicals which can lead to adverse lipid peroxidation. Third, inflammation, e.g., caused by necrotic tissue, leads up to invading microglia which release cytokines, glutamate, NO, and free radicals potentially amplifying the other pathways. Further domains with a potentially governing function in brain alterations after preterm birth are alterations in blood pressure regulation and blood-brain barrier (Millar et al., 2017). It is likely that some or all suggested pathways interact with each other (Millar et al., 2017). However, preterm-born neonates are a heterogeneous group with a wide range in birth age, complications, and outcome (Ward and Beachy, 2003).

#### 1.3.2.2 Brain alteration

Among other factors discussed above, pre- and perinatal brain maturation depends on two large transient cell populations, subplate neurons (SPNs) and pre-oligodendrocytes (pre-OLs). As discussed in 1.2.3, SPNs are relevant for the development of thalamocortical connections and cortex organization (Ghosh et al., 1990; Hoerder-Suabedissen and Molnár, 2015; Kostovic and Rakic, 1990; Luhmann et al., 2018). Due to their pivotal role in brain maturation, it has been argued that altered SPNs lead to altered brain structures which are present after preterm birth (Kanold and Luhmann, 2010; McClendon et al., 2017; McQuillen and Ferriero, 2005; Volpe, 2019, 1996). The subplate is active in the period of preterm birth and reaches its maximal extent at GA 20-35 weeks (Hoerder-Suabedissen and Molnár, 2015; Kostovic and Rakic, 1990). There are hints of the specific vulnerability of SPNs, probably GABAergic neurons to a higher extent, by hypoxic-ischemic (HI) events (Kanold and Luhmann, 2010; Kinney et al., 2012; McClendon et al., 2017; McQuillen and Ferriero, 2005). However, the actual extent and effect of HI on SPNs and if the impact is specific to these cells is debatable (Luhmann et al., 2018; McClendon et al., 2017; Millar et al., 2017). The reason for SPN sensitivity is not clear so far but it could be due to a relatively high expression of glutamate receptors (Kanold and Luhmann, 2010; Luhmann et al., 2018) which might increase the liability to excitotoxic pathways (Millar et al., 2017) or because of an adverse initial position as claimed secretory region (Millar et al., 2017). Previous studies revealed that

altered SPNs can prevent the ingrowth of thalamic afferents into the cortex (Ghosh et al., 1990) and the differentiation of cortical layers (Hoerder-Suabedissen and Molnár, 2015). Thereby, the time of the injury influences the affected region and function (McQuillen and Ferriero, 2005). Additionally, a pathological persistence of SPNs could lead to neurological and psychiatric disorders like epilepsy and schizophrenia (Hoerder-Suabedissen and Molnár, 2015; Molnár et al., 2020).

Another important transient cell population is the lineage of oligodendrocytes (OLs). As mature OLs provide myelination around axons in the central nervous system, their accurate maturation is the basis of functioning networks and presumably for proper axonal differentiation and development of the cerebral cortex (Volpe, 2019). Previous studies have detected an enhanced vulnerability of OL progenitors, i.e., pre-OLs, in prematurity with their highest amount in the developing brain at GA 24-32 weeks (Back et al., 2005; Volpe, 2019). Back and Volpe (2018) suggested that cellular characteristics of pre-OLs, more precisely a high expression of glutamate receptors like SPNs, critically low resistance against free radicals in contrast to a high accumulation of these reactive molecules, and an immature status with increased sensitivity for cytokines, might account for high liability. Direct damage of OLs, e.g., by HI or indirect damage via altered SPNs or connections is also imaginable (Volpe, 2019). Pre-OLs show a compensating proliferation after a derogating event but have a deficit in completing the maturational trajectory to functional OLs (Buser et al., 2012; Volpe, 2019). Thus, impaired pre-OLs result in hypomyelination and might lead to altered development of up- and downstream gray matter of the affected fiber tracts (Kinney and Volpe, 2018).

Prematurity is associated with macro- and microstructural changes in the whole brain (Ball et al., 2012; de Kieviet et al., 2012; Inder et al., 2005; Kelly et al., 2023; Meng et al., 2016; Nosarti et al., 2008; Schmitz-Koep et al., 2021a). However, brain alterations show high variability between individuals (Dimitrova et al., 2020). White matter (WM) injury is very common after preterm birth (Inder et al., 2005, 1999; Kinney and Volpe, 2018; Woodward et al., 2006). The magnitude varies between macroscopic necrotic lesions and cysts like in severe periventricular leukomalacia and impaired microstructure which can both be detected by MRI: Macroscopic changes include delimitable necrotic foci and a reduced WM volume (de Kieviet et al., 2012; Inder et al., 1999; Makropoulos et al., 2016; Nosarti et al., 2008; Salmaso et al., 2014; Schmitz-Koep et al., 2021a; Woodward et al., 2006); on a microscopic

level, a reduced fractional anisotropy in fiber tracts indicates altered connectivity, probably reflecting lower fiber density and reduced myelination, in preterm-born humans (Ball et al., 2012; Menegaux et al., 2020; Meng et al., 2016; Vangberg et al., 2006; Volpe, 2019, 2009). Impairment in gray matter (GM) regions can be separated into cortical and subcortical structures: Regarding the cortex, a mostly reduced GM volume is apparent and only some regions like the cingulate or right middle temporal gyrus might show an increased volume (Inder et al., 2005, 1999; Nosarti et al., 2008; Salmaso et al., 2014). Additionally, previous studies found an increased gyrification (Hedderich et al., 2019) and a decreased cortical complexity (Hedderich et al., 2020) of the cerebral cortex in preterm-born adults. It has previously been observed that subtypes of GABAergic interneurons might be reduced in the cortex after preterm birth suggesting a connection to a higher incidence of seizures (Salmaso et al., 2014). Recent examinations found that some subcortical structures, e.g., thalamus, striatum, and cholinergic basal forebrain, show a smaller volume after preterm birth, too (Aanes et al., 2019; Ball et al., 2012; Grothe et al., 2017; Inder et al., 2005; Makropoulos et al., 2016; Meng et al., 2016; Nosarti et al., 2008; Schmitz-Koep et al., 2021b). Thereby, the microstructure of examined subcortical GM regions is partly impaired which is manifested in an increased mean diffusivity, e.g., in the thalamus (Ball et al., 2012).

In contrast to decreased white and gray matter, the ventricles tend to be larger than in term-born humans (Inder et al., 2005; Makropoulos et al., 2016; Salmaso et al., 2014). Several studies propose a causal link between alterations in WM/GM and a lower cognitive performance or a reduced intelligence quotient (de Kieviet et al., 2012; Hedderich et al., 2020, 2019; Menegaux et al., 2020; Meng et al., 2016; Woodward et al., 2006) and a relation to motor outcome (Woodward et al., 2006). The combination of WM alteration and related neuron impairment is called encephalopathy of prematurity (Volpe, 2009). Aberrant macro- and microstructure are apparent in preterm-born neonates, but also in child- and adulthood (de Kieviet et al., 2012; Hedderich et al., 2021; Nosarti et al., 2008; Schmitz-Koep et al., 2021a). Furthermore, the functional connectivity might be altered after preterm birth (Bäuml et al., 2015).

#### 1.3.2.3 Impaired claustrum microstructure in preterm-born adults

Due to the overlap of the claustrum with vulnerable subplate neurons and pre-oligodendrocytes (see section 1.2.4), Hedderich et al. (2021) investigated the claustrum

macro- and microstructure in very preterm-born and very low birth weight adults: There was no difference in total-intracranial-volume-relative claustrum volume compared to term-born adults scanned at the same age. However, they found an impaired microstructure in terms of an increased mean diffusivity in the claustrum of very preterm-born or very low birth weight adults, suggesting a decreased claustrum cellularity after preterm birth. Further, they found a correlation between altered microstructure and decreased intelligence quotient suggesting a functional relationship. (Hedderich et al., 2021)

#### 1.3.2.4 Long-term consequences of body and lifestyle

Preterm birth, especially very or extreme prematurity, remains a substantial risk factor for disability in terms of motor and cognitive perturbation (Twilhaar et al., 2018b; Volpe, 2019; Woodward et al., 2006). Motor deficits range from cerebral palsy in 5-10 % to deficits in fine motor skills (Millar et al., 2017; Volpe, 2019). Cognitive disturbances are found apart or together with attention, behavior, and socialization difficulties in 25-50 % (Volpe, 2019).

Concerning mental abilities, on average, preterm-born adults have a lower intelligence quotient of around 12 points (Twilhaar et al., 2018b, 2018a; Wolke et al., 2019). Cognitive and language performance tends to be lower in boys than in girls (Skiöld et al., 2014). They show an inferior mean socioeconomic status and less family foundation (Wolke et al., 2019). Beyond that, preterm-born humans have a higher risk for specific mental disorders, like attention-deficit/hyperactivity disorder, anxiety, autism spectrum disorders, depressive and bipolar affective disorder, and psychosis and schizophrenia, than term-born controls (Johnson et al., 2010; Jones et al., 1998; Nosarti et al., 2012; Wolke et al., 2019).

Next to neurostructural alteration, preterm birth is associated with body changes. Preterm-born adults show a smaller height and an initially lower body mass index than term-born adults at the same age (Euser et al., 2008; Saigal et al., 2006). Moreover, preterm birth is related to cardiovascular diseases (Tauzin, 2015).

#### 1.3.2.5 Therapeutic options of preterm-born neonates

So far, there are sparse tangible therapeutic interventions to improve the outcome of preterm-born neonates (Millar et al., 2017). The only licensed therapy is to treat neonates suffering hypoxia-ischemia by induced hypothermia around 33°C body or at least head temperature which can affect the brain beneficially on the cellular and molecular levels (Choi et al., 2012; Millar et al., 2017; Shah et al., 2007). In general, preterm-born newborns are treated with continuous positive airway pressure, mechanical ventilation, and surfactant application

depending on the demand by immature lung status, and antenatal steroids are given in prospective premature birth (Glass et al., 2015). As environmental enrichment is associated with better long-term outcomes, the idea arises to implement stimulating conditions and special advancement for affected children or to find imitating molecules of related pathways (Salmaso et al., 2014; Volpe, 2019). Further approaches could be to influence the Wnt-β-catenin pathway for improved maturation of oligodendrocytes or application of fibroblast growth factors to promote excitatory neurons *(Salmaso et al., 2014)*. Erythropoietin and improved nutrition might have a beneficial impact on white matter alterations *(Volpe, 2019)*. Another attempt is to use stem cells in the forms of neural and glial progenitors to substitute cell loss after brain injury *(Salmaso et al., 2014)*. Apart from that, the main aim should be the prevention of prematurity to reduce infant mortality and long-term morbidity in a sustainable way (Purisch and Gyamfi-Bannerman, 2017).

## 1.4 Magnetic resonance imaging (MRI)

In the following, the technical basics of structural and diffusion magnetic resonance imaging (MRI) are explained with emphasis on T2-weighted structural imaging, mean diffusivity, and fractional anisotropy in diffusion-weighted MRI (dMRI) as these are the main sequences in our study.

### 1.4.1 MRI technique

Magnetic resonance imaging (MRI) is a comparatively new imaging technique. In contrast to common techniques like X-ray and computer tomography, it works without ionizing radiation. Instead, it is based on physical properties on the atomic level, the nuclear magnetic resonance, and it became an inherent part of clinical and research applications.

On the atomic level, the MRI signal is predicated on the nuclei of hydrogen atoms. Such nuclei consist of one proton, which is positively charged. A basic property of protons is the spin, i.e., a continuous rotation with constant frequency. The combination of both features, electric charge and spin, induce magnetic properties of the proton. Thus, these particles are sensible for magnetic fields and align their rotation axis depending on external influences. This alignment is called precession and it proceeds with a specified frequency, the Lamor frequency, which is directly proportional to the external magnetic field $B_0$. Finally, the rotation axes of the proton spins are oriented in parallel, or antiparallel to some extent, to $B_0$.

In principle, the detection of H-nuclei in big molecules is conceivable, but the common settings focus on H-nuclei in water molecules. (Weishaupt et al., 2009)

MR tomographs contain several coils for individual functions: 1) to establish a magnetic field $B_0$ which is around 60,000 times stronger than the earth's magnetic field (e.g., 3 Tesla); 2) to cause an incline of the strength of $B_0$ along the longitudinal axis of the tomograph in terms of a gradient; 3) to send a radio frequency impulse for spin deflection and 4) for voltage detection 5) further sending or detecting coils as required. As $B_0$ (1) is always activated, the spins of hydrogen nuclei of an input object align once they are close enough to the magnetic field. This effect is called longitudinal magnetization (T1). The gradient coil (2) allows a space-resolved excitation with a selected radio frequency pulse of the radio frequency coil (3). The pulse mostly deflects the spins of protons when the radio frequency matches the Lamor frequency. As the latter depends on the strength of the magnetic field, the radio frequency pulse affects one specific slice in the graded magnetic field. Thereby, the spins tilt by a flip angle of 90° which equals the transversal magnetization (T2). It is possible to adjust a smaller flip angle for more time efficiency. (Weishaupt et al., 2009)

The contrast of a structural image depends on the molecular composition of the tissue and on scanning conditions. Concerning the latter, a distinction is made between T1-, T2-weighted, and proton density sequences. There are two important parameters, repetition time (TR) and echo time (TE). Usually, there are made many recordings of each slice to get a more accurate image in the end. Thereby, TR represents the gap between two radio frequency pulses to stimulate the same slice and TE defines the time interval from radio frequency pulse emission to signal detection. To gain a T1-weighted image, the emphasis is put on the longitudinal relaxation which occurs by energy release of the radio frequency-stimulated spin to the environment (spin-grid relaxation). The contrast originates by choosing a low TR (<600 ms) when some tissues have aligned to $B_0$ while the spins in other regions are still deflected and only give a low signal. As opposed to this, a T2-weighted image focuses on dephasing due to the interplay between the "H-nuclei magnets" (spin-spin relaxation). TR is long to eliminate the effect of different longitudinal relaxation times. Additionally, TE is chosen longer (> 60 ms) to differentiate between tissues that preserve the transversal deflection and still give a high signal after TE while other tissues already lost their transversal magnetization. With a high TR and a low TE, T1 and T2 effects are minimized and the signal represents the proton density. The spatial resolution of an image slice results from supplementary gradients, a phase

coding in one dimension and a frequency coding in the second dimension. The signal can be plotted in a k-space with frequency on the x-axis and phase on the y-axis. To gain the final image, it is reconstructed by Fourier transformation. Structural MRI in humans achieves a spatial resolution of around 0.5 mm isotropic voxel size, which conform to three-dimensional pixels with a side length of 0.5 mm in each dimension, and a low resolution in time due to acquisition circumstances. (Weishaupt et al., 2009)

Before such an image, e.g., of a brain, can be analyzed, it usually passes quality control and gets excluded if it contains artifacts or is impaired differently. After this step, a preprocessing pipeline follows with brain extraction, image denoising, and probably spatial normalization always depending on the aim (Makropoulos et al., 2018b; Smith, 2004). Subsequently, a surface or volume-based atlas can be applied to segment the brain into different tissues and bigger structures (Klein et al., 2010).

In practice, MRI shows some limitations. The acquisition takes a long time in a range from minutes to more than one hour (Hughes et al., 2017). In the process, a participant has to lie in a narrow tube preferably without movement. These conditions are especially critical in uncooperative subjects like small children who might get sedated for successful scanning (Ball et al., 2012; Batalle et al., 2019; Rutherford et al., 2004). Furthermore, the movement of coils generates loud sounds so participants should wear ear protection (Weishaupt et al., 2009). A contra-indication of MRI is metal implants as they can interact with the magnetic field (Weishaupt et al., 2009). Altogether, MRI acquisition is more costly than faster computed tomography scans or X-ray and especially challenging in newborns (Hughes et al., 2017) but it allows a relatively high-resolution insight into the developing brain in vivo without radiation based on physical tissue properties.

### 1.4.2 Diffusion MRI

Diffusion-weighted MRI (dMRI) is a specialized MR imaging technique. It examines water diffusion, or more precisely the movement of the protons in the water molecules, in tissue. Thereby, dMRI detects tissue properties on a molecular level. Due to Brownian motion, small particles move continuously depending on the temperature. The movement of free water occurs in a random direction, which is called isotropic diffusion. However, in biological systems, it is restricted by boundaries like membranes, nuclei, and cell organelles. When this restriction is vectored in a special orientation, it is called anisotropic diffusion, e.g., in white matter with axon bundles. (Beaulieu, 2002)

The principle of dMRI is to expose tissue to magnetic fields and radio frequency pulses in a way that a signal emerges when the particles left their place between a dephasing and a rephasing gradient. Again, there exists a basic magnetic field $B_0$ and a radio frequency pulse is applied. The tissue parts get activated differently depending on the strength of the magnetic field in this slice. The gradient of this magnetic field is flipped after a short break and the radio frequency pulse is repeated with the same frequency. Thus, the radio frequency pulse within the second graduated magnetic field should compensate for the disparity after the radio frequency pulse in the first graduated magnetic field. Afterwards, the radio frequency emission gets detected with a latency of TE. (Mori and Barker, 1999)

However, dMRI has a lower resolution than structural MRI in a range of mm (Mori and Zhang, 2006). The practical application of dMRI includes analyses of diffusion metrics and diffusion tensor imaging with fiber tractography (Le Bihan, 2003; Mori and Zhang, 2006). We focus on mean diffusivity (MD) and fractional anisotropy (FA) in our study. MD reflects the mean-squared shift of water molecules (Le Bihan, 2003). A restricted diffusion, leading to a lower MD, reflects more obstacles like cell membranes (Le Bihan, 2003). Thus, MD is commonly interpreted as a measure of cellularity (Ball et al., 2012; Batalle et al., 2019; Hedderich et al., 2021). FA represents how directional the water movement is (Le Bihan, 2003; Mori and Zhang, 2006). The anisotropy rises in tissue with directional membranes like in white matter fiber tracts (Beaulieu, 2002; Le Bihan, 2003). Axonal myelination might increase the FA further (Beaulieu, 2002).

## 1.5 Artificial intelligence

Artificial intelligence (AI) is a broad and growing field in radiology and research in general (Bluemke et al., 2020; England and Cheng, 2019). In the following sections, some technical terms and, more specifically, the background of the AI approach of this study will be explained.

### 1.5.1 Artificial neural network

Machine learning algorithms learn rules by experience instead of applying given directives like common programs do (Jordan and Mitchell, 2015). Artificial neural networks are a machine learning approach based on cross-linked variables similar to biological neural networks with connected neurons. The idea is relatively young and was first presented in 1943 by Warren McCulloch and Walter Pitts (McCulloch and Pitts, 1943; Russell and Norvig,

2016). In the 1950s, scientists like John McCarthy experimented practically and in theory to evolve network-based programs that can solve increasingly difficult problems (Russell and Norvig, 2016). A basic model for neural information storage and organization is the perceptron by Rosenblatt (1958). In the late 1970s, convolutional neural networks (CNN) with two-dimensional input and filters as learning parameters came up (Schmidhuber, 2015).

There are many subtypes of AI approaches, i.e., classification (Campanella et al., 2019), regression (Iglovikov et al., 2018), and segmentation (Li et al., 2021), as well as different learning strategies, i.e., supervised, unsupervised, and reinforcement learning (England and Cheng, 2019; Jordan and Mitchell, 2015; Russell and Norvig, 2016). Apart from this, models can be distinguished by their architecture. The famous neural networks are one option besides decision tree, k-nearest neighbor, support vector machines, and others (Hastie et al., 2009). In our study, we apply a deep neural network, i.e., a convolutional neural network, for neonatal claustrum segmentation trained with supervised learning.

Deep learning models contain several layers between input and output levels, so-called hidden layers. Each layer can have an individual shape in terms of the count of nodes or data dimensions. In addition, there are differences in connections between these nodes: fully connected, non-fully connected, and residual networks differ in count and range of links. Empirically, deep learning is a common AI approach for processing complex or extensive data like images (LeCun et al., 2015).

Computations in neural networks are composed of multiplication. The requested complexity arises from an activation function. This function supplies non-linearity between the network layers. One famous option is the Rectified linear unit (ReLU) which returns the value itself if the input is positive and zero if it is negative or zero (LeCun et al., 2015). Other activation functions are sigmoid, tanh, or logistic functions (Hastie et al., 2009; LeCun et al., 2015).

Another important instruction for training is the loss function. This function calculates the error by comparing the output with the ground truth and subsequently, its derivative determines how to improve the model (LeCun et al., 2015). The parameters get optimized layer by layer starting from behind which is called backpropagation (LeCun et al., 2015). One big limitation of neural networks is overfitting which means, the model adapted perfectly to the training data but can not generalize to new data (England and Cheng, 2019). Thus, the model should be trained and tested carefully.

### 1.5.2 Convolutional neural network

Convolutional neural networks (CNN) belong to a certain type of neural network. They deal with more-dimensional input like images. In contrast to the common conception of neural networks with learning parameters as simple numbers, the learning part of CNNs are filters. These filters, also called kernels, are matrices with an eligible shape. Throughout the processing, these kernels move with a defined step size, also called stride, "over" the input. Each unit of the filter is multiplied by the corresponding image unit below in terms of a dot product. The result is written in a new matrix, the feature or activation map. This matrix is filled with each step of the filter on the input image. In the end, there exist as many feature maps as filters. The kernel size, e.g., 3x3 or 5x5, usually exceeds a height and width of one. Thus, with striding over the input matrix, the count of dot products is less than the width of the image. Consequently, the output matrix decreases. This phenomenon can be prevented by padding which adds lines and columns of pixels around the input image. These accessory values are often zeros but they can be regulated in a more sophisticated way, too. In all, a convolutional layer comprises a specified number of filters that convert one input to a stack of feature maps which equals the output of this layer. (O'Shea and Nash, 2015)

While training, each filter learns to recognize an individual feature. These characteristics are represented in the values of the filter matrix. The dot product will be higher if the underlying part of the image shows the quested pattern. Thus, the feature map reveals in which part of the image the feature is expressed more or less. The filters of the first layer are usually simple edge detectors. With increasing depth, the kernels become more complex. For example, they detect specified combinations of edges or even entire structures. (LeCun et al., 2015)

A CNN incorporates different types of layers. A convolutional layer is always concatenated with an activation function for non-linearity like layers in other neural networks (see 1.5.1). Directly after this sequence or after a repetition for one or more times, there usually follows a pooling layer. A pooling layer aims to generalize important characteristics by attenuating information about the precise appearance and orientation of the image content. This step compresses the matrix and simultaneously maintains relevant features of the input. A common method is max-pooling where the input matrix is divided into squares of a defined size and the maximum value of each tile attends to the output matrix. A square size of 2x2 halves the height and width of the input. In all, such a down-sampling stack of convolutional layers, activation functions, and pooling layers is called an encoder. (LeCun et al., 2015)

In contrast to encoders, decoders enlarge a matrix. They take the output of an encoder and regenerate it to the original input size. Depending on the settings, upsampling layers can use different techniques to interpolate the input. In this process, the matrix regains the initial shape but is lacking in details of the image of the beginning. To sustain that information, skip connections are employed. They tie layers with equal sizes of matrices. A current method for skip connections simply copies and concatenates the arrays of the encoder and decoder into one array which is the input of the next layer of the decoder. (Drozdzal et al., 2016)

The application of CNNs is multifarious. A widespread use is for segmentation which could also be described as pixel-wise or voxel-wise classification (England and Cheng, 2019): the model labels each unit as the region of interest or not. For this function, an encoder and a decoder are connected to a U-net structure often with skip connections between them (Gabr et al., 2020; Li et al., 2021; Ronneberger et al., 2015).

# 2 Hypotheses

This work integrates two projects: first, a method optimization of automated claustrum segmentation in neonatal brain MRI; second, the analysis of the claustrum macro- and microstructure in preterm- and term-born neonates.

## 2.1 Reliable automatic claustrum segmentation in neonatal brain MRI

Due to the intricate shape and small size of the claustrum, the structure is not registered in common neonatal MRI atlases (Alexander et al., 2019; Makropoulos et al., 2018a, 2014). Furthermore, to the best of our knowledge, there is no standardized segmentation algorithm available for neonates. Manual segmentation needs neuroanatomical expertise and is very time-consuming. To fill this lack, we hypothesized that automated segmentation by deep learning with transfer learning from adult scans is efficient and accurate in claustrum segmentation in neonatal brain MRI.

Overall, the claustrum was traced in 558 neonatal brain MRIs of the developing Human Connectome Project by manual segmentation in 30 scans and by a subsequently trained and optimized artificial intelligence (AI) in 528 scans. The code and models for the AI approach were made publicly available (https://github.com/hongweilibran/claustrum_multi_view).

## 2.2 Impaired claustrum structure in preterm-born neonates

The claustrum is a highly connected gray matter structure in the mammalian forebrain (Jackson et al., 2020; Milardi et al., 2015; Smith et al., 2018; Torgerson et al., 2015). Its perinatal development is closely related to transient cell populations, i.e., subplate neurons (SPNs) (Bruguier et al., 2020; Hoerder-Suabedissen and Molnár, 2015; Watson and Puelles, 2017) and pre-oligodendrocytes (pre-OLs) (Kinney and Volpe, 2018). Both cell populations are vulnerable to hypoxic-ischemic events (Back and Volpe, 2018; Kinney et al., 2012; McQuillen and Ferriero, 2005; Volpe, 2019, 1996) which are common incidents in prematurity (McClendon et al., 2017). Thus, Hedderich et al. (2021) proposed that this impairment influences claustrum development and showed that claustrum microstructure is altered in preterm-born adults. However, to the best of our knowledge, no previous study has investigated the claustrum structure in human newborns. Based on the stated developmental relationships and observations in adults, we hypothesized that claustrum structure is already impaired in preterm-born neonates.

To address this question, we compared the claustrum macro- and microstructure of 83 preterm- and an equally sized group of term-born neonates at term equivalent age. We analyzed the claustrum in respect of its development in a spectrum of 377 term-born subjects and a longitudinal examination of 53 double-scanned preterm-born subjects. The claustrum macrostructure included absolute and total brain volume-relative claustrum volume in T2-weighted brain MRI and the microstructure was measured by mean diffusivity and fractional anisotropy derived from diffusion-weighted imaging. The correlation between the claustrum and other brain regions was compared between preterm- and term-born neonates.

# 3 Materials

To investigate the claustrum in preterm- and term-born neonates, we built on a current, large-scale, public dataset from the developing Human Connectome Project (dHCP).

## 3.1 Developing Human Connectome Project

In our study, we included all 558 scans of the second data release 2019 of the developing Human Connectome Project (dHCP) under the ethical commitment of the UK Health Research Authority (www.developingconnectome.org). The dHCP aims to map the brain in more than 1,000 fetal and neonatal scans to facilitate research of the developing human brain in a multi-sequence evaluation of structural, resting-state functional, and diffusion MRI for connectome exploration (Hughes et al., 2017). Recruitment and scanning took place at the Evelina Newborn Imaging Centre, St Thomas' Hospital in London, UK (Hughes et al., 2017). Exclusion criteria for participating were metal implants, high medical risk, or parental language difficulties but not risk of neurodevelopmental disorder (http://www.developingconnectome.org/study-inclusion-and-exclusion-criteria/). A paper of consent signed by the parents was requested before scanning (Hughes et al., 2017). Scanning was conducted in natural sleep, except for six subjects who were indicated, with an acquisition protocol optimized for neonatal subjects by hard- and software adaption with a 32-channel head coil in a Philips Achieva 3T (Hughes et al., 2017). T1w and T2w structural MRI, functional and diffusion MRI were acquired, preprocessed, visually controlled, and released with sparse additional information about birth age, birth weight, sex, singleton/multiple status, scan age, radiology score (medical assessment of a neuroradiologist) and sedation condition (https://github.com/BioMedIA/dHCP-release-notes) (Hughes et al., 2017; Makropoulos et al., 2018b). In our analysis, we focus on T2w structural MRI for macrostructural analysis and diffusion-weighted MRI for microstructural analysis. The 558 structural scans include 377 term-born subjects and 128 preterm-born subjects (Table 1 and Figure 3).

***Table 1: Characteristics of the T2-weighted and diffusion-weighted scans provided by the developing Human Connectome Project.***

| MRI sequence | Reconstructed voxel size ($mm^3$) | Subjects (male) | Scans which passed the QC | Median scan age (GA) | Range of scan age (GA) |
|---|---|---|---|---|---|
| T2-weighted | 0.5*0.5*0.5 | 505 (283) | 558 | 40.6 | 29.3-45.1 |
| Diffusion MRI | 1.5*1.5*1.5 | 445 (249) | 490 | 40.4 | 29.3-45.1 |

GA = Gestational age in weeks, QC = Quality control.

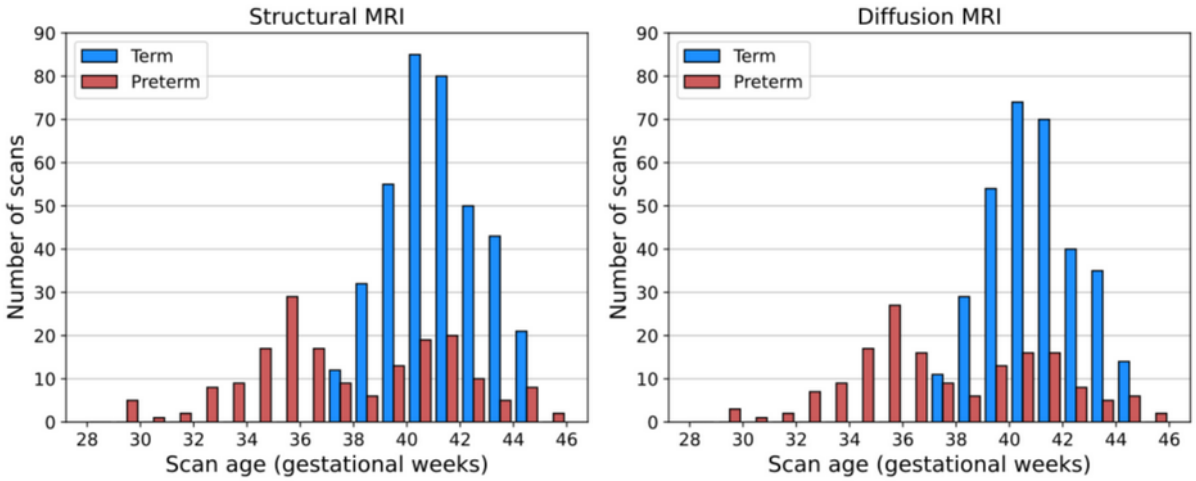


***Figure 3: Number of structural and diffusion-weighted scans of preterm- and term-born neonates of the second data release of the developing Human Connectome Project.***

*The structural scans include 558 T2-weighted scans, 378 from term-born neonates and 180 from preterm-born neonates. The diffusion-weighted scans comprise 490 scans, 327 from term-born neonates and 163 from preterm-born subjects.*

## 3.2 Structural MRI

Due to the immature developmental stage of the neonatal brain, the contrast appearance in MRI differs from that of adults (Alexander et al., 2017). Thus, the preferred image sequence for neonates is T2w scans and the dHCP focuses on this modality instead of typically preferred T1w images in adults. The second data release of the dHCP comprises 558 T2w scans of 505 neonates with a median (range) birth age of gestational age (GA) 39.1 weeks (24.3-42.3 weeks) and a median scan age of GA 40.6 weeks (29.3-45.1 weeks). Details of age and sex distribution are presented in Table 1 and Figure 3.

T2w scans were acquired in axial and sagittal planes with a Turbo Spin Echo sequence (repetition time (TR) = 12 s, echo time (TE) = 156 ms, SENSE factor (axial) = 2.11, SENSE

factor (sagittal) = 2.58) with an overlapping resolution of 0.8*0.8*1.6 $mm^3$ and a reconstructed resolution of 0.5*0.5*0.5 $mm^3$ (Makropoulos et al., 2018b). Scans were preprocessed with rigid motion correction (Cordero-Grande et al., 2018), bias correction, and specialized reconstruction (Kuklisova-Murgasova et al., 2012; Makropoulos et al., 2018b). Afterwards, a Brain Extraction Tool was applied (Smith, 2002). Additionally, the brain was automatically segmented with Draw-EM (Developing brain Region Annotation With Expectation-Maximization) into 87 regions by the dHCP (Makropoulos et al., 2018b, 2014). Based on this atlas, the total brain volume (TBV; the sum of gray and white matter including the brainstem excluding cerebrospinal fluid, ventricles, and extracranial background) was calculated and regions were defined for comparison with the claustrum.

## 3.3 Diffusion MRI

Diffusion-weighted imaging is challenging in non-cooperative neonatal subjects as it is vulnerable to motion (Bastiani et al., 2019a; Hutter et al., 2018). Thus, the provided diffusion-weighted images (dMRI) comprise a subset of the preceding structural MRI subjects which passed partly automated diffusion quality control (Bastiani et al., 2019b). The second data release of the dHCP includes 490 scans of 445 neonates with a median (range) birth age of GA 39.0 weeks (24.6-42.3 weeks) and a median scan age of GA 40.4 weeks (29.3-45.1 weeks). Details of age and sex distribution are presented in Table 1 and Figure 3.

The scans were acquired with High Angular Resolution Diffusion Imaging by a monopolar spin-echo echo-planar imaging Stejksal-Tanner sequence (TR = 3.8 s, TE = 90 ms, in-plane resolution = 1.5 mm, slice thickness = 3 mm, slice overlap = 1.5 mm) (Bastiani et al., 2019a; Hutter et al., 2018; Makropoulos et al., 2018b). Several b-values (400, 1000, and 2600 $s/mm^2$) and four phase encoding directions led to 300 volumes per subject (Bastiani et al., 2019a). Data were processed by correction for eddy current, susceptibility-induced distortions, and motion by the dHCP (Bastiani et al., 2019a). A super-resolution algorithm reconstructed an isotropic resolution of 1.5 mm (Bastiani et al., 2019a).

# 4 Claustrum segmentation in neonatal MRI

To record the claustrum macro- and microstructure for each subject, individual claustrum segmentations are needed. As the claustrum is an intricate and small structure, there is no standard automatic method for segmentation or registration so far.

## 4.1 Methods

The following sections describe evaluation metrics for segmentation, manual annotation, and optimized automated claustrum segmentation in T2-weighted neonatal brain MRI.

### 4.1.1 Segmentation evaluation metrics

For this study, the claustrum is segmented in 558 T2-weighted neonatal brain MRIs. In the first approach, the annotations were conducted manually. As this is a very time-consuming task, we used these samples to train a convolutional neural network (CNN) to achieve automated segmentation. We evaluate the performance of the CNN by comparing the automated segmentation with manual results with three metrics.

First, the Dice similarity coefficient (DSC) is a standard metric to detect the spatial overlap between two three-dimensional segmentations A and B (Dice, 1945; Taha and Hanbury, 2015):

$$DSC = \frac{2 \cdot |A \cap B|}{|A| + |B|} \tag{1}$$

Second, the Hausdorff distance (HD) is a metric for the surface distance between segmentations A and B of a small region (Karimi and Salcudean, 2020; Taha and Hanbury, 2015):

$$HD(A, B) = max\{\sup_{x \in A} \inf_{y \in B} d(x, y), \sup_{y \in B} \inf_{x \in A} d(x, y)\} \tag{2}$$

Thereby, d(x, y) equals the Euclidean distance of x and y while sup labels the supremum and inf the infimum. To reduce the impact of outliers, we used the 95th percentile of the Hausdorff distance (HD95) (Mendrik et al., 2015).

Third, the volumetric similarity (VS) measures the volume conformity where $V_A$ and $V_B$ are the volumes of two segmentations A and B:

$$VS = 1 - \frac{|V_A - V_B|}{V_A + V_B} \quad (3)$$

### 4.1.2 Manual segmentation

We segmented right and left claustrum in 30 T2-weighted scans with ITK-SNAP (version 3.6.0) (Yushkevich et al., 2006) (Free download: http://www.itksnap.org/pmwiki/pmwiki.php?n=Downloads.SNAP3) on a Wacom Intuos M tablet (Wacom Co., Ltd., Kazo, Saitama, Japan) as a basis for later automated segmentation. To objectify the manual approach, the region was assessed in axial and coronal view at optimal image contrast following a structured segmentation protocol (Supplement A) which is a modified version of the protocol for adults (Hedderich et al., 2021). Manual segmentation took around 35 minutes per subject. After training in adults and neonates, the rater (A. N.) segmented the claustrum in 30 subjects under close supervision of an experienced neuroradiologist (D. H.). Time-delayed, ten subjects were segmented for a second time by the same rater and additionally by another rater (J. W.) to calculate intra- and inter-rater reliability. The subjects were chosen randomly.

### 4.1.3 Automated segmentation

To reduce the manual workload and to provide a consistent claustrum segmentation, the efficient automated claustrum segmentation in adults (Li et al., 2021) was modified and optimized for newborns by transfer learning.

#### 4.1.3.1 Additional data pre- and post-processing

The 30 randomly chosen subjects which were segmented manually were separated into a training set with 20 scans and a test set with the ten scans used for intra- and inter-rater reliability. The remaining 528 scans were assigned to the correction set. Correction set means these scans did not pass a pure manual segmentation but a manual correction after the automated segmentation. An overview is given in Figure 4 and Table 2.

For standardized input properties, images were preprocessed in addition to the dHCP processing. In the beginning, scans were transformed into numpy arrays with SimpleITK. The gained image arrays were, first, treated with z-score normalization to gain a mean intensity of zero and a unit standard deviation in each image. Intensities smaller than thresh equals ten conform to the image parts around the brain. These values are not relevant for brain presentation and do not pour into the calculation of the mean in the normalization method. Segmentation arrays with different labels for the right and left claustrum were simplified to

the same label for both. The orientation control acquired an axial and a coronal array for each input. Second, the arrays were cropped to a uniform shape of 200 x 200 pixels. Third, the first and last 25 % of slices were skipped by an empirical decision to exclude slices that do not cover the claustrum to shorten the processing time.

The model predictions are finally post-processed to reverse the preprocessing steps. First, the segmentation map is padded to its original size to revert the cropping in the pre-processing sequence. Second, labeling in the first and last 25 % of the slices are categorized as artifact and consequently removed as proposed by Li et al. (2021). For further analyses, right and left claustrum segmentations were separated by dividing the automated segmentation into halves and renaming the label in one half.

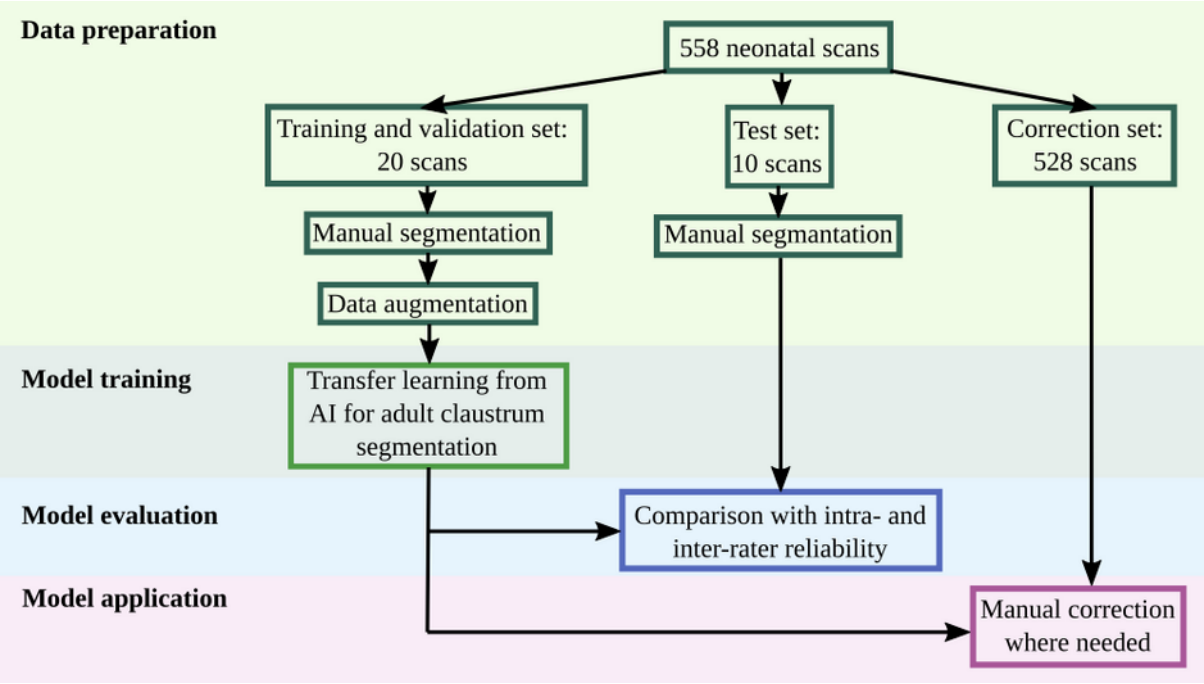


***Figure 4: Overview of four workflow steps.***

*From the top to the bottom: 1) data preparation with separation in training, test, and correction set; 2) model training by transfer learning from adult scans; 3) model evaluation on a test set and comparison with human reliability; and 4) model application in a large cohort. Figure inspired by Neubauer et al. (2022), used under CC By. AI = artificial intelligence.*

***Table 2: Overview of the three datasets, training, test, and correction set.***

| | **Training set** | **Test set** | **Correction set** |
|---|---|---|---|
| Number of Scans (male) | 20 (13) | 10 (7) | 528 (297) |
| Mean scan age (range) in gestational weeks | 39.9 (36.1–42.6) | 40.4 (38.7–42.3) | 40.0 (29.3–45.1) |
| Number of scans of preterm-born neonates | 3 | 0 | 177 |

#### 4.1.3.2 Model architecture

For this study, we applied the same AI architecture as for automated claustrum segmentation in adult brain MRI (Li et al., 2021).

**Two-dimensional network.** The approach is based on a convolutional neural network (CNN) built on a U-net structure (Figure 5) which is typical for image segmentation tasks (Litjens et al., 2017). The "U" refers to the composition of an encoder and a decoder consecutively. The encoder consists of two convolutional layers (kernel-size = 3, stride = 1) with a rectified linear unit (ReLU) as a non-linear activation function (LeCun et al., 2015):

$$\text{ReLU:}\quad f(x) = max(0, x) \tag{4}$$

A max-pooling layer with a pool size of 2x2 is appended respectively. This pattern recurs three times and works as a down-sampling part. In parallel, the amount of filters of the convolutional layers is rising after each pooling layer: 32, 64, 96, 128, 256. With a preprocessed input size of 200x200x1, the first convolutional layer with 32 filters outputs a stack of 32 feature maps, 200x200x32. The output of the next convolutional layer has the same shape. After the first max-pooling function, which halves the height and width of each feature map, it becomes 100x100x32. At the bottom of the encoder, the shape is 12x12x256.

The second part follows in an inversely up-sampling manner to regain the initial size for an equivalent prediction. Each up-sampling layer is attended by two successive convolutional layers with a gradually decreasing amount of filters. Four skip connections assure that primary image information is still available for the label prediction after the sampling procedure. They link layers of similar size from encoder to decoder. After completed up-sampling, a zero-padding layer adjoins some voxels to compensate fading effects of max-pool layers with odd input shapes. The added final convolutional layer with a sigmoid activation function reveals one value for each voxel of the input slice. Values higher than a threshold of 0.4 are set to label 1, and smaller amounts are set to label 0. This threshold showed visually superior results than 0.5 in adults and neonates. The output is a segmentation with the

presumable claustrum traced with label 1 with the original shape of 200x200x1. For training, Adam optimization is applied. Overall, one u-shaped, single-view model contains 2,494,529 trainable parameters in 19 convolutional layers.

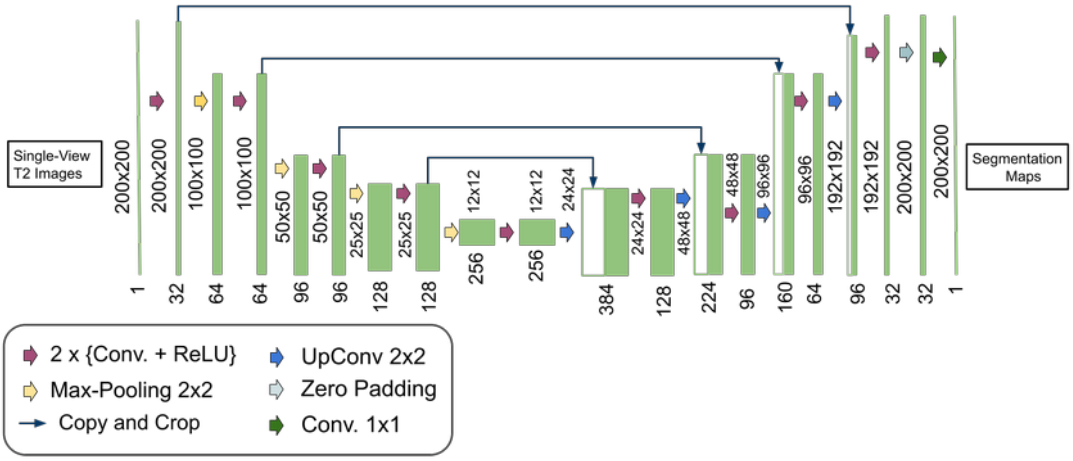


***Figure 5: Architecture of the 2D convolutional neural network.***

*An image slice is fed into the network and a segmentation map of the claustrum is the output. In between, image features are extracted by convolutional layers (Conv.) linked by rectified linear units (ReLU) and Max-Pooling layers. The second half includes upconvolutional layers (UpConv) instead of Max-Pooling. Copy and Crop label the skip connections. Figure reproduced from the Online Supplement of Neubauer et al. (2022), used under CC By.*

**Loss function.** The loss function is an essential part of the training process by regulating the optimization of parameters. During training, the network predicts the label of training images. This automated segmentation compared with the ground truth, a manual segmentation, results in a specific loss. Depending on its value the parameters are slightly adapted for improved automated segmentation and a lower loss in the future. A common cross entropy loss is inept for the unbalanced classes of the claustrum and non-claustrum voxels in each slice. The applied Dice loss can handle the data unbalance (Li et al., 2021; Milletari et al., 2016):

$$Dice\ Loss = \frac{-2 \cdot |A \circ B| + s}{(|A| + |B|) + s} \tag{5}$$

A and B represent the 2D manual segmentation and automated segmentation while ◦ stands for an entry-wise product and |+| stands for an entry-wise sum of both matrices. To avoid dividing by zero, s is set to one if otherwise, the denominator was zero.

**Multi-view model.** Based on the hypothesis that claustrum segmentation profits from the evaluation in different orientations, Li et al. (2021) proposed a multi-view learning approach involving axial and coronal views. Therefore, three axial and three coronal models were

trained separately and combined in the end to a multi-view model to reduce outliers of single models.

**Characteristics of transfer learning.** Transfer learning (TL) is a way to accelerate the learning process by building on a pre-trained model (Ghafoorian et al., 2017; Pan and Yang, 2010; Shin et al., 2016). The previous model shares the model architecture and solves Task A, claustrum segmentation in T1-weighted adult brain MRI, while the new model will adapt it for Task B, claustrum segmentation in T2-weighted developing neonatal brain MRI (Figure 6). Thus, we load the weights of a pre-trained model from Task A and train it with data from Task B. Thereby, basic image detection features can be adopted instead of learning from randomly initialized weights (Shin et al., 2016).

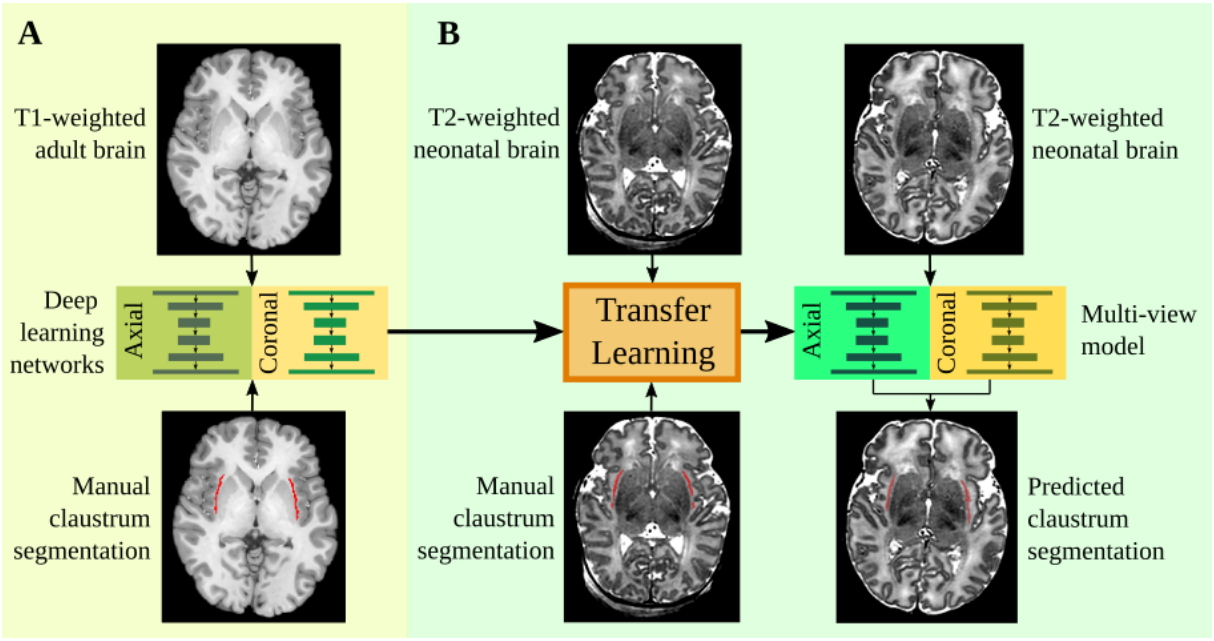


***Figure 6: Overview of the transfer-learning task.***

*(Task A) An axial and a coronal model trained for claustrum segmentation in T1-weighted adult brain MRI are the foundation for (Task B) the training with T2-weighted neonatal brain MRI and corresponding manual segmentations. This results in an axial and a coronal model (actually, three axial and three coronal models), combined in a multi-view model, predicting the claustrum in unseen neonatal MRI. Figure inspired by Neubauer et al. (2022), used under CC By.*

**Pretrained model.** The pre-trained model equals the model for claustrum segmentation in adult MRI. Detailed methods and results of the pre-trained model are presented by Li et al. (2021). The axial and coronal pre-trained models were trained and tested with 181 T1-weighted adult brain MRI and their corresponding manual segmentations. The data were part

of the Bavarian Longitudinal Study and included images from four different scanners with a reconstructed isotropic voxel size of 1 $mm^3$. The manual segmentation of the dorsal and ventral claustrum in these subjects was performed by an experienced neuroradiologist (D. H.) guided by a structured segmentation protocol with axial and coronal evaluation. The models were trained without data augmentation. (Li et al., 2021)

The model achieved VS, HD95, and DSC of 93.3 %, 1.41 mm, and 71.8 %, respectively. In comparison with intra-rater reliability, the automated segmentation reached comparable VS and superior HD95 and DSC indicating slightly superior performance than expert annotation. (Li et al., 2021)

#### 4.1.3.3 Technical approach

The model was trained with the following hardware and software:

As machine learning models contain a vast number of parameters, they need high computational power for the training process. Graphics processing units (GPU) are optimized for the parallelization of calculations. A Linux server running Ubuntu 20.04 with 64 GB random-access memory in Garching with access via the Leibnitz Rechenzentrum was provided by the Technical University of Munich. The training was performed on one NVIDIA Titan-V GPU with 12 GB memory. It took around 12 minutes to train a model with 4200 images with a size of 200x200 pixels for 30 epochs.

The code was running in an anaconda environment (version 4.6.11) with python (version 3.7). Additional installations were tensorflow-gpu (version 2.1.0), SimpleITK (version 2.0.2) for processing MRI files, scikit-learn (version 0.24.0) for k-fold cross validation, imgaug (version 0.4.0) to access common data augmentation methods, and pandas (version 1.2.0) for our test code. The GPU was accessed with CUDA.

The neonatal claustrum segmentation models were trained and tested by the author under the close supervision and support of Hongwei Bran Li. Complementary code for training and testing and the neonatal models were published on GitHub (https://github.com/hongweilibran/claustrum_multi_view).

Hyperparameters include the number of epochs, describing for how many times the model gets optimized with the training set; the batch size as the number of images which are considered at once before the model weights get updated according to the loss; the learning rate which defines the step size for updating the model weights; and optionally further adjustments like random seed for reproducible results. For hyperparameter optimization, we

used five-fold cross-validation to gain an independent validation set without losing data for a separated validation set. Therefore, the training set was split into five equal parts. Four sections, i.e., 80 %, were used as a training set, and the remaining fraction, 20 %, was used as a validation set. This apportionment was repeated till all parts were validation set for one time. Given a training set of twenty images, we gained five models where each was trained with 16 scans and validated on four scans.

Hyperparameters and stopping criteria were selected as follows: To choose the optimal number of epochs, we trained an axial and a coronal five-fold cross-validation model for 30 and for 50 epochs, respectively. We found no significant difference in all three metrics tested with a Wilcoxon signed-rank test (VS: p-value = 0.21, HD95: p-value = 0.45, DSC: p-value = 0.78) but the training for 30 epochs was more time-efficient (Figure 7). Thus, we chose 30 epochs for training with transfer learning. The batch size was set to 60 as such a big value tended to a more stable training process than a small batch size while a bigger batch size needed more working memory. The learning rate of 0.0002 was chosen empirically like in Li et al. (2021). We did not use the random seed for our experiments.

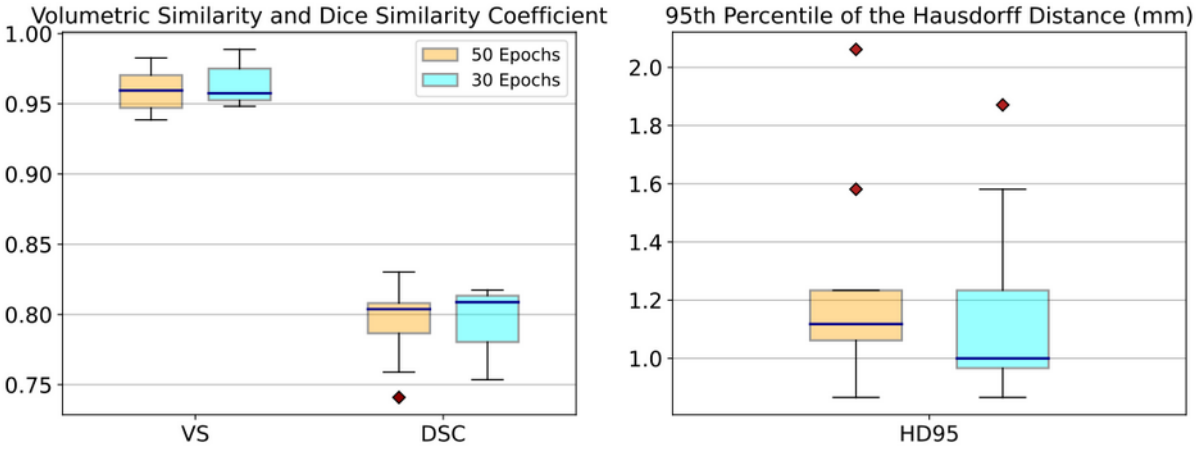


***Figure 7: Comparison of two transfer learning models trained for 50 and 30 epochs.***

*Both were trained with scale, rotate, shift, and shear as data augmentation methods. DSC = Dice Similarity Coefficient, HD95 = 95$^{th}$ percentile of the Hausdorff Distance, VS = Volumetric Similarity.*

#### 4.1.3.4 Data augmentation

To enlarge the training set without further manual annotation, we examined data augmentation (DA). The selected transformations were imported from the python library imgaug (version 0.4.0). In detail, we tested moderate scaling, rotation, shearing, shift, and modified grayscale

intensities and added the altered images to the original training set resulting in a doubled amount of training data. While the first four methods were applied to images and segmentations, the grayscale function was solely applied to the images before the other methods were conducted. In all cases, one axial and one coronal model were trained with 16 scans of one fold of the five-fold cross-validation for 50 epochs, and the performance was assessed with the remaining four scans as a validation set, respectively.

Models without data augmentation were trained for 50 epochs based on empirical values. Taking into consideration that we increased the training set, a reduction of epochs was reasonable. To test this hypothesis, an axial and a coronal model were trained with the same fold as before but for 30 epochs and tested on the same validation set (see 4.1.3.3 and Figure 7).

#### 4.1.3.5 Comparison of transfer learning with non-transfer learning

We trained non-transfer learning (non-TL) models as an alternative design to transfer learning and compared their performance. Non-TL means a model is trained from scratch. The model architecture is filled with random parameters in the beginning. Then, the model is exclusively trained with data corresponding to the task.

The non-TL models build on the same architecture as presented by Li et al. (2021). Ultimately, it is the same approach as for adults (Li et al., 2021) but with a smaller, neonatal training set, data augmentation, and adjusted hyperparameters in a developing cohort. The batch size and learning rate were identical to the TL approach, which was 60 and 0.0002, respectively, to provide a comparable procedure. Likewise, the same data augmentation methods, scale, rotate, shift, and shear, were applied. However, training from scratch can not profit from the general image analysis features of pre-trained models. Consequently, it takes more epochs to learn the needed traits for similar performance. The optimal number of epochs was chosen with an axial and a coronal model of five-fold cross-validation, trained with 16 images, respectively. The weights of these models were continuously saved after 25 epochs of training. DSC, VS, and HD95 were calculated with the corresponding validation set of four images (Figure 8). As all scores stabilized between 250 and 300 epochs, we chose 275 epochs for non-TL training.

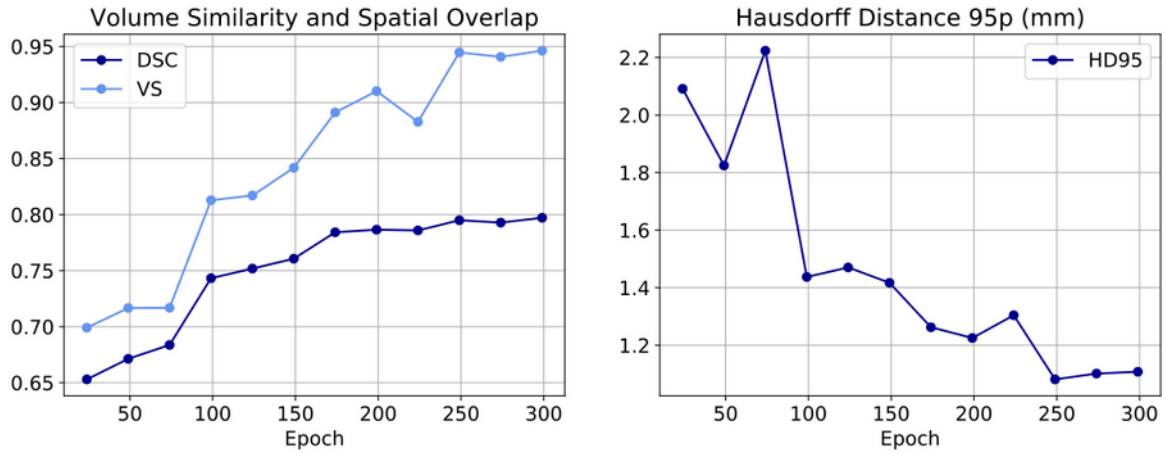


***Figure 8: Non-transfer learning model performance over 300 epochs.***

*A coronal and an axial non-transfer learning model were trained with 16 images of the first fold of five-fold cross-validation for 300 epochs, respectively, to find a period with high accuracy and low computational cost. The mean Dice similarity coefficient (DSC) and the volumetric similarity (VS) were calculated and plotted for the validation set of four scans. Both scores straightened between epochs 250 and 300. The Hausdorff Distance (HD95) behaved similarly. The mean, 275 epochs, was chosen as optimum for the non-transfer learning approach. Figure reproduced from the Online Supplement of Neubauer et al. (2022), used under CC By.*

Subsequently, five axial and five coronal five-fold cross-validation models were trained. A Wilcoxon signed-rank test was conducted to compare these results with five-fold cross-validation of TL models regarding VS, HD95, and DSC.

#### 4.1.3.6 Applicability evaluation in a large-scale dataset

To assess the model performance in a large cohort of neonates, the optimized multi-view model was applied to the remaining data, the so-called correction set comprising 528 scans (scan age range: GA 29.3–45.1 weeks). Subsequently, the automated segmentations were controlled visually and corrected where needed. The corrected versions were compared with the original automated segmentations regarding DSC, HD95, and VS for right and left claustrum together and separately.

Regarding the model performance distribution in the correction set sorted by scan age, we hypothesized that the young scan age with related immature neuroanatomy distracts the model 4.2.4. This could be due to the older subjects in the training set (scan age range: GA 36.1–42.6 weeks) in comparison with the younger subjects in the correction set with dropped accuracy (GA < 35.0 weeks, see 4.2.4). To verify the theory, we expect a higher multi-view model

performance in these youngest subjects when the models are trained with scans from this age. Thus, we replaced two neonates of the training set, both were scanned at GA 40.9 weeks, by two younger subjects, who were scanned at GA 29.9 and 29.3 weeks. The resulting multi-view model was tested on the five subjects with the lowest DSC by the former non-age-stratified multi-view model. To ensure that the accuracy remains stable in the older neonates, the age-stratified trained model was also tested on the original test set (scan age range: GA 38.7–42.3 weeks). The performance of the multi-view models with and without age-stratified training sets were compared on the original test set with a Wilcoxon signed-rank test.

## 4.2 Results

To reduce laborious manual annotations, a deep learning approach with transfer learning was developed and optimized for automated segmentation of the neonatal claustrum in T2-weighted brain MRI.

### 4.2.1 Data augmentation results

To evaluate which combination of data augmentation (DA) methods is profitable, we plotted volumetric similarity (VS), Dice similarity coefficient (DSC), and 95th percentile of the Hausdorff distance (HD95) of one axial and one coronal five-fold cross-validation model, respectively, in Figure 9 in comparison with TL without DA. We found that all DA models showed minor differences. While TL without DA reached the highest median VS of 97.1 %, the DA models vary between 95.6 % ("+ Shear and Contrast") and 96.0 % ("Scale, Rotate, Shift" and "+ Shear"). The median DSC of all DA approaches lies within a small range of 80.2-80.5 % superior to TL without DA. While the highest 75th percentile is achieved by "+ Shear and Contrast", the highest 25th percentile is attained by "+ Shear". "+ Shear and Contrast" reached the lowest median HD95 of 1.06 mm. However, the interquartile range of "+ Shear" (median: 1.12 mm) was smaller in terms of more stable performance and the model without multiply contrast takes less computational power. Thus, we decided to use shift, scale, rotate, and shear, and random order was set to True for a larger variability.

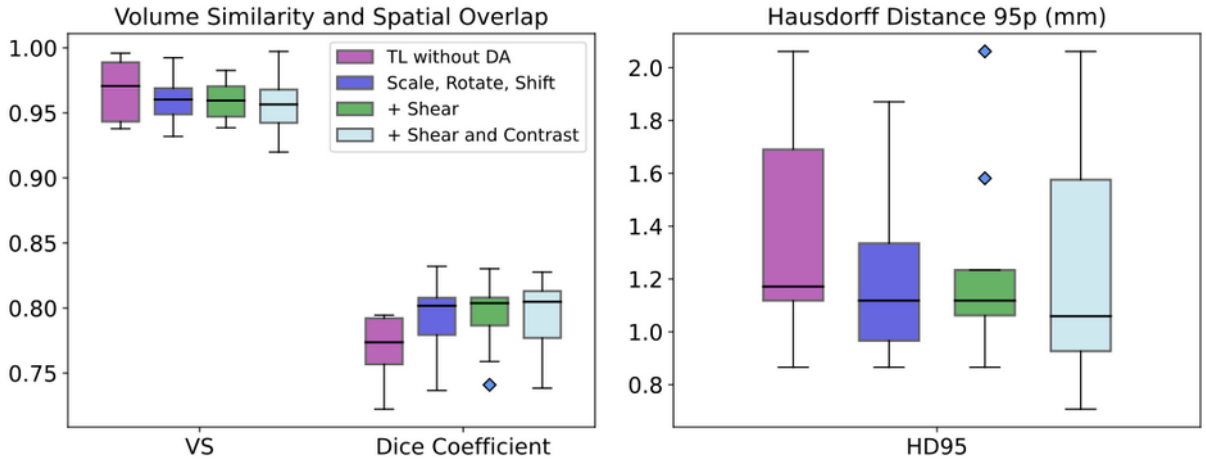


***Figure 9: Comparison of transfer learning (TL) without data augmentation (DA) and three approaches with DA.***

*The methods three and four build on method two. The models were trained for 50 epochs, respectively. Figure reproduced from the Online Supplement of Neubauer et al. (2022), used under CC By. HD95 = 95$^{th}$ percentile of the Hausdorff Distance, VS = Volumetric Similarity.*

To assess if the models trained with the chosen DA methods and 30 epochs are superior in comparison with models trained without DA trained for 50 epochs, we trained all axial and coronal five-fold cross-validation models, respectively. The Wilcoxon signed-rank test showed no difference for VS but significantly improved HD95 and DSC with DA (Table 3). Consequently, we trained our further models with DA.

***Table 3: Comparison of five-fold cross-validation models with and without data augmentation.***

| Metrics | VS (%) Median, [IQR] | HD95 (mm) ↓ Median, [IQR] | DSC (%) Median, [IQR] | Epochs | Training (hours) |
|---|---|---|---|---|---|
| TL without DA | 94.6, [89.0, 98.3] | 1.12, [0.87, 1.58] | 76.1, [72.2, 79.2] | 50 | 1.6 |
| TL with DA | 95.3, [92.8, 97.8] | 1.06, [0.87, 1.52] | 78.9, [75.4, 80.8] | 30 | 2.0 |
| p-value | 0.132 | **0.007** | **<0.001** | -- | -- |

*Data augmentation (DA) and non-data augmentation approaches used transfer learning (TL) from adult scans. Significant p-values ($p < 0.05$) are labeled in bold. Table adapted from the Online Supplement of Neubauer et al. (2022), used under CC By. ↓ means that smaller values indicate better performance. DSC = Dice Similarity Coefficient, HD95 = 95$^{th}$ percentile of the Hausdorff Distance, IQR = interquartile range, VS = Volumetric Similarity.*

### 4.2.2 Accuracy of automated segmentation

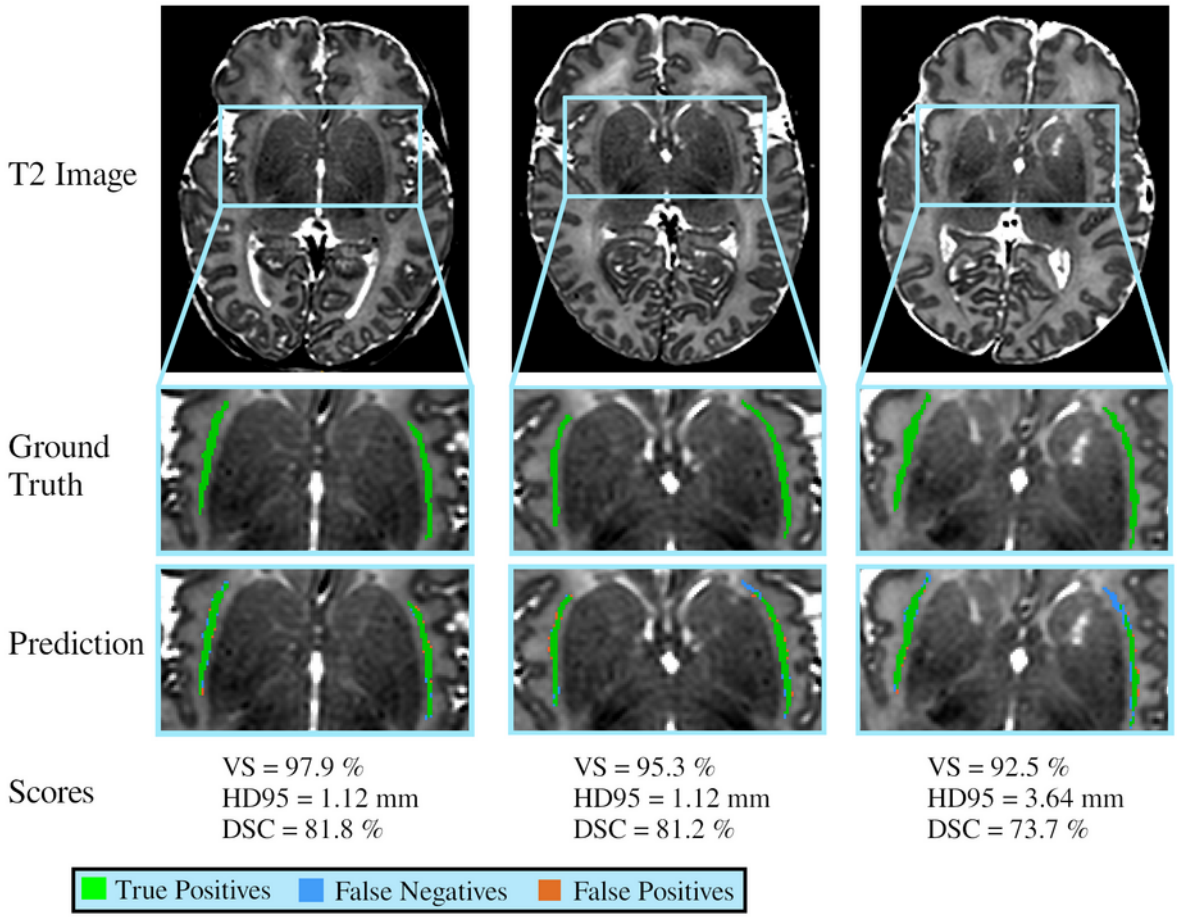


***Figure 10: Three examples of the claustrum segmentation in neonatal T2-weighted brain MRI.***

*The prediction corresponds to the automated segmentation masks. The green, blue, and orange pixels, represent true positives, false negatives, and false positives, respectively, in comparison with the manual segmentation (Ground truth). The scans are sorted by the Dice similarity coefficient (DSC). Figure reproduced from Neubauer et al. (2022), used under CC By. HD95 = 95th percentile of the Hausdorff distance, VS = Volumetric similarity.*

For a first impression of the automated segmentations, Figure 10 provides three visual examples sorted by DSC. Testing the multi-view model trained on 20 scans from the training set on ten scans of the test set, manual segmentation (ground truth) and automated segmentation (prediction) show a high agreement with a median VS of 95.9 %, an HD95 of 1.12 mm, and a DSC of 80.0 %. Figure 11 reveals two adverse outliers concerning VS and HD95 and one for DSC. However, there was no case of a fundamental failure to basically detect right and left claustrum which would lead to low DSC and high HD95. The results suggest a high accuracy of the automated claustrum segmentation.

Due to the small and sheet-like structure, even trained humans show some variance in claustrum segmentation. For this reason, the model performance was compared with intra- and inter-rater reliability in the test set, i.e., the variance of one rater or the variability between two human raters, with a Wilcoxon signed-rank test (Table 4). Regarding intra-rater reliability, there was no significant difference for VS ($p = 0.959$) while HD95 ($p = 0.011$) and DSC ($p = 0.005$) of one human rater were significantly more reliable than the automated segmentation. In comparison with inter-rater reliability, the automated segmentation showed comparable HD95 ($p = 0.203$), superior VS ($p = 0.047$), and superior DSC ($p < 0.005$). The findings indicate a higher model performance than two human raters in a partly subjective task.

Besides, automated segmentation is far more time efficient and can pare down the human workload. While compiling an automated segmentation takes around six seconds on one NVIDIA Titan-Xp graphics processing unit (12 GB Random Access Memory) and around one minute on an NVIDIA GeForce GTX 1650 (4 GB Random Access Memory), a pure manual segmentation takes 30 to 90 minutes depending on the rater and the experience. Including a visual control of the automated segmentations, which took around 3.5 minutes per subject by a trained rater, the time advantage is still enormous and the procedure assures high quality. This observation suggests that training a model is worthwhile for big cohorts like the developing Human Connectome Project (dHCP) (Hughes et al., 2017).

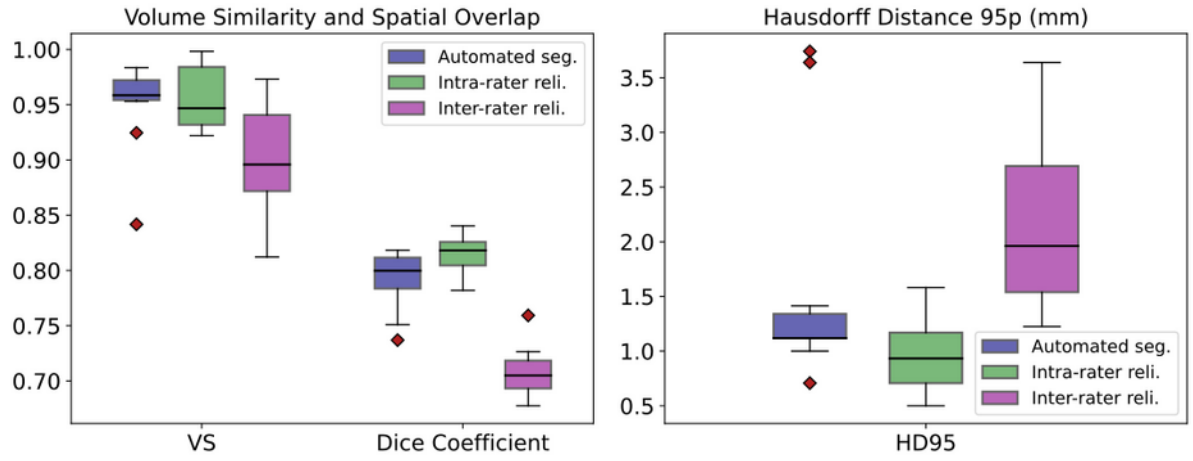


***Figure 11: Comparison of automated segmentation (seg.) with intra- and inter-rater reliability (reli.).***

*While the intra-rater reliability is significantly superior to automated segmentation regarding Hausdorff distance (HD95) and Dice similarity coefficient, the automated segmentation is superior to inter-rater reliability concerning volumetric similarity (VS) and Dice similarity coefficient. Figure reproduced from Neubauer et al. (2022), used under CC By.*

***Table 4: Results of manual and automated claustrum segmentation.***

| Metric, median [IQR] | A) Automated segmentation | B) Intra-rater reliability | C) Inter-rater reliability | p-value (A vs. B) | p-value (A vs. C) |
|---|---|---|---|---|---|
| VS (%) | 95.9 [95.4, 97.2] | 94.7 [93.2, 98.4] | 89.6 [87.2, 94.1] | 0.959 | **0.047** |
| HD95 (mm) ↓ | 1.12 [1.12, 1.34] | 0.93 [0.71, 1.17] | 1.96 [1.54, 2.69] | **0.011** | 0.203 |
| DSC (%) | 80.0 [78.4, 81.2] | 81.8 [80.5, 82.6] | 70.5 [69.3, 71.8] | **0.005** | **<0.005** |

*Wilcoxon signed-rank test between volumetric similarity (VS), 95th percentile of the Hausdorff distance (HD95), and the Dice similarity coefficient (DSC) of automated segmentation (A) and intra- (B) and inter-rater reliability (C), respectively. For each score, the interquartile range (IQR) is shown in square brackets. Significant p-values are labeled in bold. Table reproduced with slight adjustment from Neubauer et al. (2022), used under CC By. ↓ means that smaller values indicate better performance.*

### 4.2.3 Comparison of transfer and non-transfer learning results

To compare transfer learning (TL) and non-transfer learning (non-TL), we performed five-fold cross-validation for axial and coronal views. While the TL approach was superior regarding the VS (p = 0.050), the non-TL models achieved significantly lower HD95 (p = 0.016) (Figure 12 and Table 5). There was no significant difference regarding the DSC (p = 0.452). In total, TL and non-TL showed comparable results.

***Table 5: Comparison of transfer learning with non-transfer learning.***

| Metrics | VS (%) Median, [IQR] | HD95 (mm) ↓ Median, [IQR] | DSC (%) Median, [IQR] | Training Time (hours) [number of epochs] |
|---|---|---|---|---|
| Non-TL | 93.5, [91.0, 95.7] | 1.00, [0.71, 1.27] | 79.4, [76.5, 80.4] | 17.5 [275] |
| TL | 95.3, [92.8, 97.8] | 1.06, [0.87, 1.52] | 78.9, [75.4, 80.8] | 2.0 [30] |
| p-value | **0.050** | **0.016** | 0.452 | -- |

*Transfer (TL) and non-transfer learning (non-TL) performance of five axial and five coronal five-fold cross-validation models, respectively, was compared with a Wilcoxon signed-rank test. Significant p-values (p≤0.05) are labeled in bold. Table reproduced from Neubauer et al. (2022), used under CC By. ↓ means that smaller values indicate better performance. DSC = Dice similarity coefficient, HD95 = 95th percentile of the Hausdorff distance, IQR = interquartile range, VS = Volumetric similarity.*

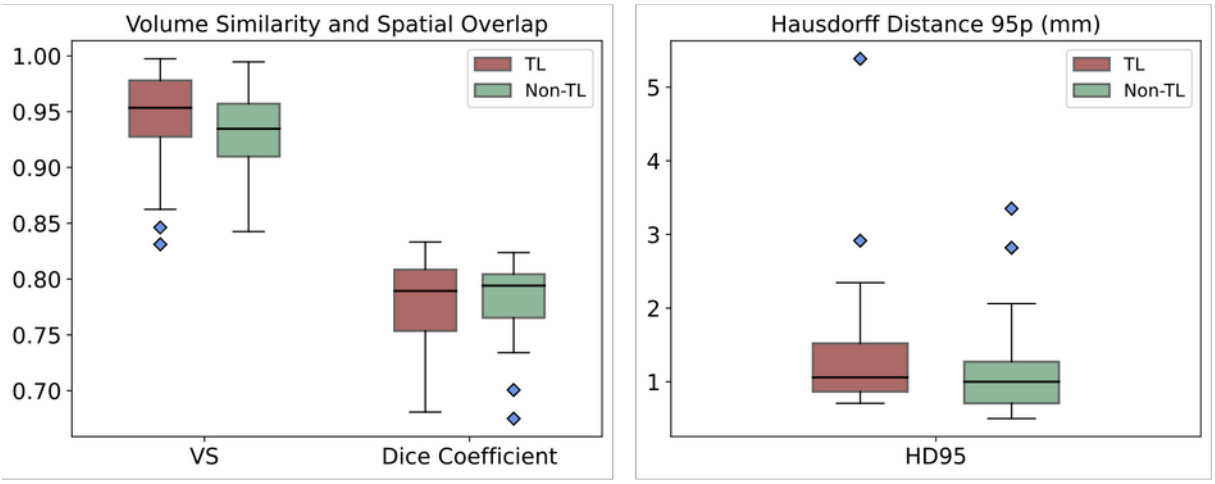


***Figure 12: Comparison of transfer and non-transfer learning.***

*Comparison of five-fold cross-validation models trained with transfer learning (TL) for 30 epochs and trained with non-TL for 275 epochs. Figure reproduced from Neubauer et al. (2022), used under CC By. HD95 = 95th percentile of the Hausdorff distance, VS = Volumetric similarity.*

Though, the biggest difference between transfer and non-transfer learning is the training time. As the non-TL models were trained for 275 epochs, it took around nine times as long as the TL models which were trained for 30 epochs. TL saves time and computational power. Thus, it is more efficient than non-TL with similar performance.

Another interesting finding is the disparate decrease of training and validation Dice loss. The courses of one axial TL model and one axial non-TL model, both trained and validated with the same fold of five-fold cross-validation, are presented in Figure 13. The TL model was exceptionally trained for 275 epochs to illustrate the trend in the full range. The non-TL model possesses a short sharp decline of both losses for the first two epochs. Thereafter, both values show a concave progression. After 30 epochs, the training loss and validation loss of the non-TL model equal 0.94. After the training is completed with 275 epochs, the training loss is 0.57 and the validation loss is a bit higher at 0.70. The TL model adapts faster and undercuts a training loss of 0.20 after eleven epochs while the non-TL model shows a loss of 0.95 at this juncture. The decrease of the TL training loss slows down after this sharp decline and achieves 0.15 after 30 epochs and 0.08 after 275 epochs. The TL validation loss shows a similar process but on a higher level. It reaches 0.48 after 30 epochs and 0.46 after 275 epochs. Overall, training and validation loss of TL are lower than the losses of non-TL at all

observation points, suggesting a clearer distinction of the claustrum and non-claustrum regions by the TL approach.

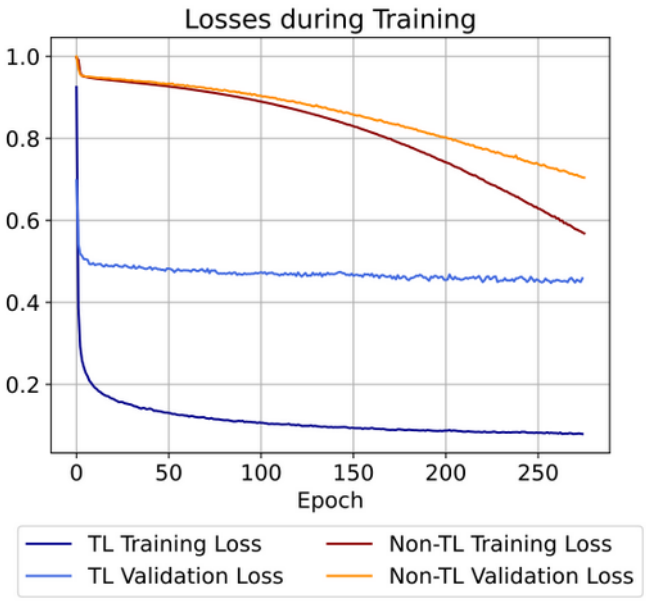


***Figure 13: Dice loss during transfer and non-transfer learning.***

*The Dice loss decreased during the training of one axial transfer learning (TL) model and one axial non-TL model. For reasons of clearness, the TL-model was also trained for 275 epochs although it was only trained for 30 epochs for practical application. Figure reproduced from the Online Supplement of Neubauer et al (2022), used under CC By.*

Regarding the DSC, HD95, and VS of the validation set in synopsis with the Dice loss, the performance remained static after 30 epochs of TL or 275 epochs of non-TL. These results are in accord with the TL loss progress while the non-TL loss did not saturate in the proposed training period (Figure 13). These findings suggest a divergence between Dice loss and DSC. The Dice loss builds on the preliminary model output where a float is assigned to each voxel. In the next step, these floats pass a certain threshold (in this study the threshold was set to 0.4). While higher numbers denote the voxel as claustrum, lower numbers declare the voxel as background. So even if the labels are set correctly in the end, the model could be optimized further for a clearer distinction of claustrum and non-claustrum, i.e., values closer to 0 for non-claustrum and values closer to 1 for claustrum. In contrast, the DSC is based on the binary values, 0 for background and 1 for claustrum, of the segmentation mask without gradient. A further aspect is that the Dice loss is calculated for each slice whereas the DSC considers the volume. As the claustrum delineation is especially challenging in edge regions, the slice-wise calculation might lead to outliers with low accuracy for slices in the claustrum

periphery although the three-dimensional agreement was acceptable. To resume, TL seems to provide a presumably more differentiated segmentation by shorter training and a comparable performance to non-TL.

Supervised learning requires annotated data for training but manual claustrum segmentation in MRI needs expert knowledge and is very time-consuming. Therefore, we analyzed the needed amount of data for effective transfer learning to reduce the manual effort of coming projects. In detail, we trained an axial model with two scans and tested it on our test set of ten images. Afterwards, we expanded the training set with two images, resulting in four images for training, and calculated the scores of the test set like before. We continued this process till we reached a training set of 20 images conforming to our original training set (Figure 14). By training with two scans, the model achieved a DSC of 39.7 %, a VS of 51.2 %, and an HD95 of 27.3 mm. Even training with four subjects provided >85 % of the performance with 20 scans regarding DSC and VS. All three scores improved up to twelve images in the training set. Beyond that, there only remained a minimal shift of DSC up to 18 images. The findings suggest that a training set with around 16 scans and corresponding annotations can be sufficient to obtain a high quality segmentation result.

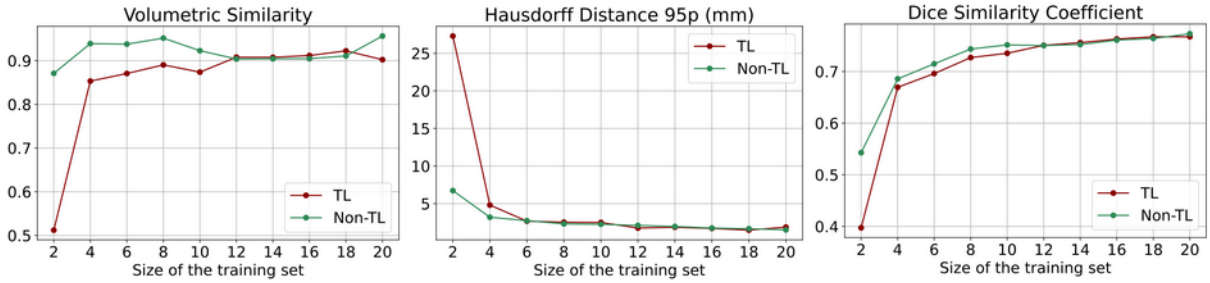


***Figure 14: Comparison of the model performance after training with transfer learning (TL) and non-TL with different sizes of the training set.***

*Non-TL led to superior results in training sets smaller than twelve scans. There was hardly a difference in bigger training sets. While TL models were trained for 30 epochs, non-TL models were trained for 275 epochs. Figure reproduced from the Online Supplement of Neubauer et al. (2022), used under CC By.*

To test if DA impacts the needed amount of training data, we repeated the experiment with TL with and without DA. While the DA model shows a flat rise with at least four scans (DSC = 66.9 %), the model without DA needs eight scans for training to achieve a similar DSC (65.6 %) (Figure 15), indicating that DA can reduce the required amount of training data. The model performance stagnated by training with more than 16 scans for both methods regarding

VS and HD95. The mean results with DA were superior to training without DA regarding DSC and VS and similar for HD95 for most of the training sets, suggesting a beneficial effect of DA application probably beyond the reduction of training images.

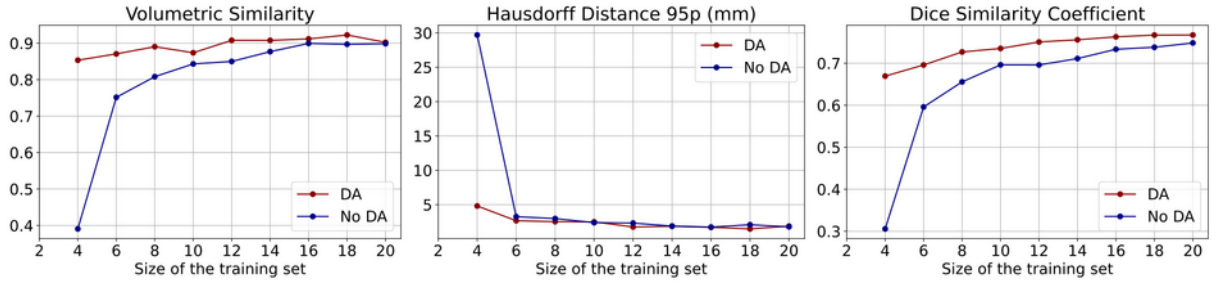


***Figure 15: Comparison of the model performance after transfer learning with and without data augmentation (DA) for different training set sizes.***

*Training with DA led to higher accuracy in all metrics while the gap decreased for volumetric similarity and Dice similarity coefficient, and disappeared for the Hausdorff distance with the increasing training set. Figure reproduced from the Online Supplement of Neubauer et al. (2022), used under CC By.*

### 4.2.4 Large-scale applicability of the multi-view model

The proposed multi-view transfer-learning model was only trained on 20 scans. To assess the generalizability of this approach, the multi-view model was applied to the correction set, comprising 528 scans that were not part of the training or test set (558 dHCP scans minus 20 training scans minus 10 test scans). The scans were acquired in a range of GA 29.3-45.1 weeks. A visual control with manual correction where necessary was performed in all automated segmentations. The procedure was based on the segmentation protocol of manual segmentation with axial and coronal assessment (Supplement A). It was performed with ITK-Snap (version 3.6.0) (Yushkevich et al., 2006). The agreement between predicted and corrected segmentation was calculated (Figure 16A). For right and left claustrum together, the median [interquartile range = IQR] DSC was 97.7 % [96.3 %, 98.6 %], the median HD95 was 0.0 mm [0.0 mm, 0.5 mm] and the median VS was 98.5 % [97.4 %, 99.3 %]. The HD95 plot shows a slim distribution as only minor adaptions were made and we calculated the 95$^{th}$ percentile of the Hausdorff distance instead of the maximal distance between automated segmentation and the corrected version. Most of the scans underwent minor corrections, indicating an accurate segmentation by the multi-view model in the majority of cases.

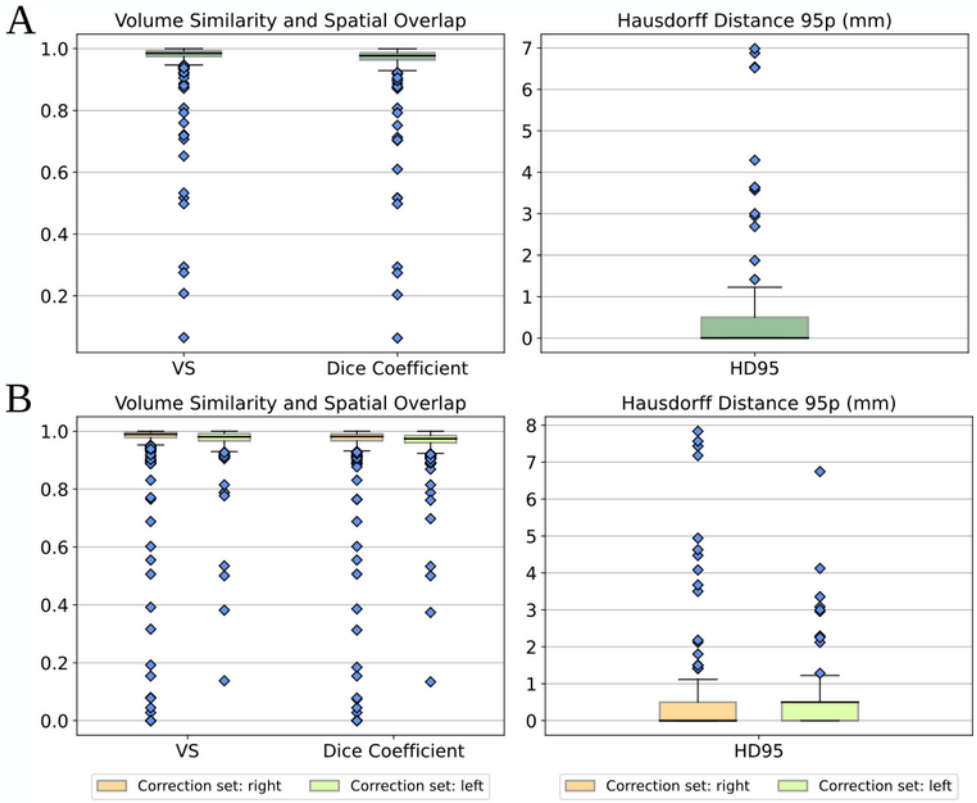


***Figure 16: Accordance between automated segmentation of the multi-view model and subsequent manual correction.***

*(A) for right and left claustrum together and (B) for right and left claustrum separately. In most of the 528 cases, the agreement was very high. In some subjects, detection of the right and left claustrum was incomplete. Figure adjusted from Neubauer et al. (2022), used under CC By. HD95 = 95th percentile of the Hausdorff distance, VS = Volumetric similarity.*

***Table 6: Accuracy of the multi-view model in detecting the right and left claustrum.***

| **Metrics** | **VS (%) Median, [IQR]** | **HD95(mm)↓ Median, [IQR]** | **DSC (%) Median, [IQR]** |
|---|---|---|---|
| Right claustrum | 98.9, [97.8, 99.6] | 0.00, [0.00, 0.50] | 98.2, [96.7, 99.1] |
| Left claustrum | 98.1, [96.6, 99.2] | 0.50, [0.00, 0.50] | 97.4, [96.6, 99.2] |
| p-value | **<0.0001** | -- | **<0.0001** |

*The automated segmentation and the subsequently performed correction were compared in 528 scans, respectively. A Wilcoxon signed-rank test was performed to test for significant differences between the hemispheres. The accuracy was higher for the right claustrum than for the left. Significant p-values are labeled in bold letters. Table reproduced from the Online Supplement of Neubauer et al. (2022), used under CC By. ↓ means that smaller values indicate better performance. DSC = Dice similarity coefficient, HD95 = 95th percentile of the Hausdorff distance, IQR = Interquartile range, VS = Volumetric similarity.*

To test whether there is an accuracy difference between automated segmentations of the right and left claustrum, the metrics, VS, HD95, and DSC, of the correction set were compared, respectively (Figure 16 B). As the deep learning model did not distinguish between right and left, a short python script (version 3.8.10) assigned all putative claustrum annotations in the right half of the scan to the right claustrum and labels in the other half of the scan to the left claustrum. The performance in the right claustrum was significantly higher than in the left claustrum regarding VS ($p < 0.0001$) and DSC ($p < 0.0001$) (Table 6). In total, the accuracy gap is small, suggesting a minor side bias.

However, there were few subjects in the dHCP cohort with low performance. Masks with distinct deficits in detecting a full claustrum or explicit parts of it in several continuous slices by visual evaluation were inscribed. In three cases, the right claustrum was not detected at all and the left claustrum was hardly labeled (see Table 7). Furthermore, there were nine scans with rarely traced right claustrum and seven scans with deficient identification of the right and left claustrum, particularly in the right dorso-rostral region. In rare cases, the model traced too much. There were examples of small groups of annotated voxels in the insula, putamen, and small hypointense areas in the frontal or occipital temporal lobe. There was no case of widespread tracing of non-claustrum regions. Overall, there were 14 scans with a DSC < 81.8 % which equals the mean intra-rater reliability. This conforms to 2.7 % of the correction set. Figure 17 and Table 7 give examples of scans with low performance. The analysis indicates that the model performance is reliable for the most part but the user should be attentive to extraordinarily small volumes.

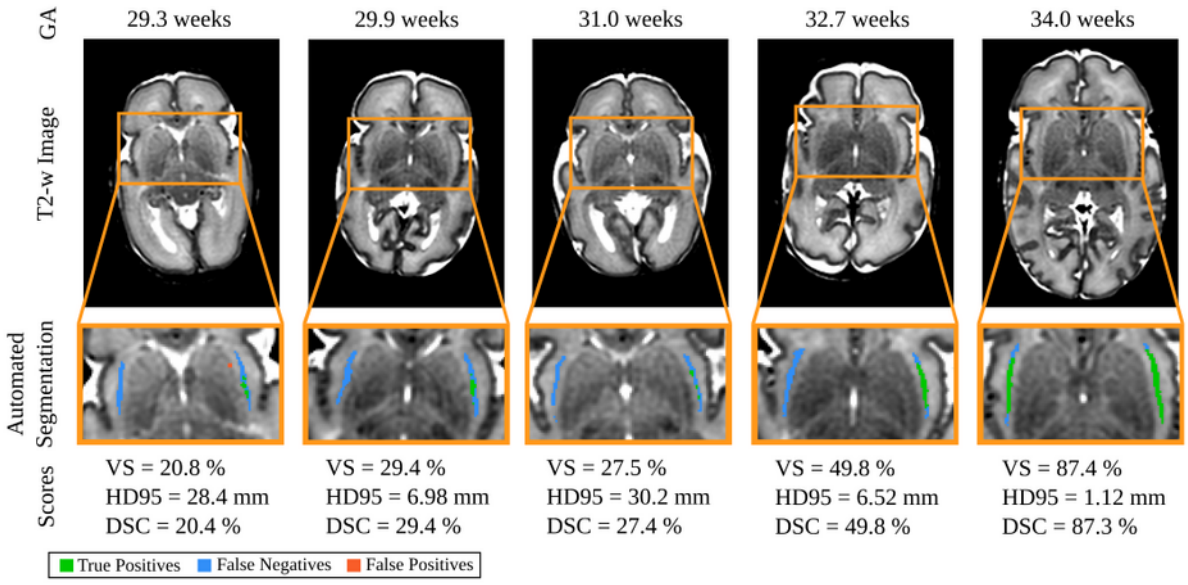


***Figure 17: Examples of the automated claustrum segmentation in very young neonates.***

*The five subjects are sorted by scan age. They were all scanned before gestational age (GA) 35 weeks. The Figure from the Online Supplement of Neubauer et al. (2022) was expanded by two examples, used under CC By. DSC = Dice similarity coefficient, HD95 = 95th percentile of the Hausdorff distance, VS = Volumetric similarity.*

***Table 7: Statistics of the five subjects with the lowest Dice similarity score (DSC) of the automated segmentation.***

| | **Scan age (GA)** | **Birth age (GA)** | **Birth weight (kg)** | **Gender (male/ female)** | **VS (%)** | **HD95 (mm) ↓** | **DSC (%)** |
|---|---|---|---|---|---|---|---|
| Mean (±SD) | 30.6 (±1.2) | 27.4 (±1.2) | 0.76 (±0.14) | 2/3 | 27 (±14) | 20 (±11) | 27 (±14) |
| Range (min-max) | 29.3-32.7 | 26.1-28.7 | 0.54-0.96 | - | 6.52-49.8 | 6.52-30.2 | 6.35-49.8 |

*The young scan age of all subjects was suspicious. ↓ means that smaller values indicate better performance. GA = gestational age in weeks, HD95 = 95th percentile of the Hausdorff distance, SD = standard deviation, VS = volumetric similarity.*

### 4.2.5 Superior accuracy with age-stratified training set

To analyze the reason for the accuracy drop in some scans, we plotted the performance along the scan age (Figure 18). We found that all scans with a DSC < 81.8 %, corresponding to the mean intra-rater reliability, were acquired before GA 35 weeks although not all subjects younger than GA 35 weeks showed a low performance. This finding is consistent for VS and HD95, suggesting an age-dependent performance of the deep learning approach. Remarkably, the scans of the training set only cover the range of GA 36.1-42.6 weeks, suggesting that the

performance is limited due to narrow training data. The five subjects with the lowest DSC (Table 7) were assigned to a new test set for a multi-view model with an age-stratified training set while the corrected version of the first automated segmentation was defined as ground-truth to test the new model. The new multi-view model achieved a median VS, HD95, and DSC of 84.9 %, 1.22 mm, and 70.4 %, respectively, in the five young subjects with the lowest performance of the former multi-view model, indicating a performance increase in young subjects after training with scans from this age (Figure 19 and Table 8).

To assure a stable high performance in older neonates, the new multi-view model was also tested on the original test set of ten subjects. Surprisingly, the VS was significantly higher (p=0.009) for the new multi-view model in comparison with the former multi-view model (Table 9). There was no significant difference for HD95 (p=0.091) and DSC (p=0.508). This finding suggests that training a model for a neonatal cohort generally profits from a wide age range in the training set.

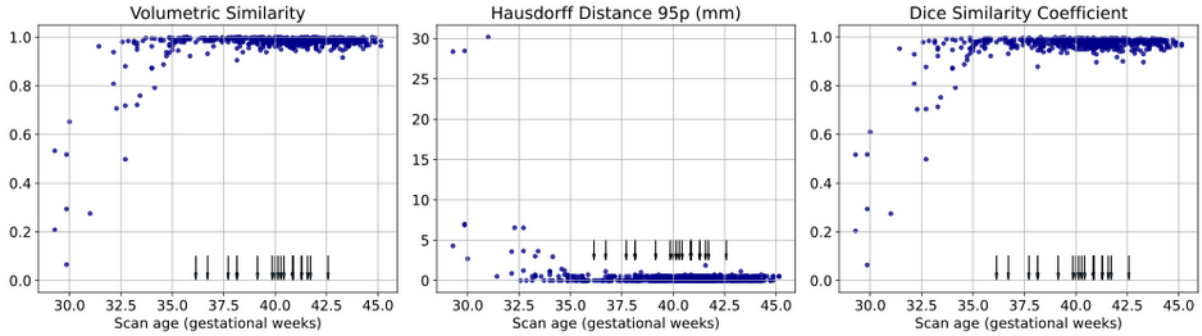


***Figure 18: Accuracy of automated segmentation plotted along scan age.***

*Automated segmentation was compared with their corrected versions, respectively. The down-head arrows label the scan age of the subjects in the training set. The accuracy dropped in some subjects younger than 35 gestational weeks which is outside of the training sample age range. Figure adapted from Neubauer et al. (2022), used under CC By.*

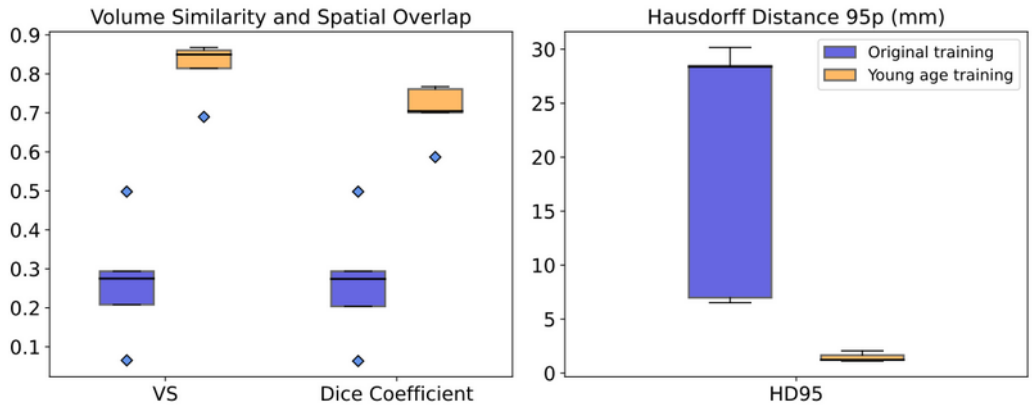


***Figure 19: Multi-view model performance without and with age-stratified training.***

*Performance of the multi-view model trained with the original training set and the new multi-view model trained with the same training set as the original models but two older neonates were replaced by two subjects scanned before 30.0 gestational weeks (Young age training). The accuracy is shown for the five subjects with the lowest Dice coefficient of the first model. The young age training led to higher performance in all three scores. Figure reproduced from the Online Supplement of Neubauer et al. (2022), used under CC By. HD95 = 95th percentile of the Hausdorff distance, VS = Volumetric similarity.*

***Table 8: Multi-view model performance after age-stratified training in young subjects.***

| Metrics | VS (%) Median, [IQR] | HD95(mm)↓ Median, [IQR] | DSC (%) Median, [IQR] |
|---|---|---|---|
| Original training set | 27.5, [20.8, 29.4] | 28.4, [6.98, 28.5] | 27.4, [20.4, 29.4] |
| Including young age scans | 84.9, [81.4, 86.0] | 1.22, [1.22, 1.66] | 70.4, [70.1, 76.1] |

*Comparison of a multi-view model trained on the originally defined training set and a multi-view model trained on the same size of samples including two young subjects scanned before 30.0 gestational weeks. The models were tested on the five subjects with the lowest performance of the originally trained algorithm. The sample size is too small for a reasonable Wilcoxon signed-rank test. However, superior performance of the multi-view model trained with two young subjects is clearly visible. ↓ means that smaller values indicate better performance. DSC = Dice similarity coefficient, HD95 = 95th percentile of the Hausdorff distance, IQR = Interquartile range, VS = Volumetric similarity.*

***Table 9: Multi-view model performance after age-stratified training in the original test set.***

| Metrics | VS (%) Median, [IQR] | HD95(mm)↓ Median, [IQR] | DSC (%) Median, [IQR] |
|---|---|---|---|
| Original training set | 95.9, [95.4, 97.2] | 1.12, [1,12, 1.34] | 80.0, [78.4, 81.2] |
| Including young age scans | 97.6, [95.7, 98.4] | 1.12, [1.02, 1.20] | 79.9, [77.8, 80.9] |
| p-value | **0.009** | 0.091 | 0.508 |

*Comparison of a multi-view model trained on the originally defined training set and a multi-view model trained on the same size of samples including two young subjects scanned before 30.0 gestational weeks. The latter showed significantly superior performance on the originally defined test set of ten scans, scanned between 38.7-42.3 gestational weeks, regarding volumetric similarity (VS). Table reproduced from the Online Supplement of Neubauer et al. (2022), used under CC By. ↓ means that smaller values indicate better performance. DSC = Dice similarity coefficient, HD95 = 95th percentile of the Hausdorff distance, IQR = Interquartile range, VS = Volumetric similarity.*

## 4.3 Discussion

Automated claustrum segmentation in neonatal brain MRI was successfully established with deep learning by transfer learning (TL) from adult scans. Standardized segmentation of the claustrum in neonatal brain MRI with atlases is not available because of the intricate claustrum shape and small size. The deep learning approach was optimized and evaluated in a large cohort. It yielded a high accuracy with minimal need for manual correction. The code was made publicly available (https://github.com/hongweilibran/claustrum_multi_view) to promote claustrum research in neonatal MRI by efficient segmentation. Automatic segmentation of other small brain structures could be established in parallel to this workflow.

### 4.3.1 Efficient claustrum segmentation

The developed algorithm achieved high accuracy in all three metrics, volumetric similarity (VS), Hausdorff distance (HD95), and Dice similarity coefficient (DSC). While the performance was inferior to intra-rater reliability regarding two scores, it outperformed inter-rater reliability regarding VS and DSC. This is especially relevant in large datasets which might be manually segmented by several raters if no automatic method was available. Consequently, the model trained with a small number of segmentations from one rater is more stable than annotations of two human raters. This effect is apparent despite both human raters followed the same segmentation protocol. All scores were superior to automated claustrum segmentation in T1-weighted adult scans with a DSC of around 72 %, respectively (Albishri et al., 2019; Li et al., 2021). This could be due to the higher image resolution in the neonatal scans, 0.5 vs. 0.7 mm or 1.0 mm isotropic voxel size, and the associated larger volume counted in voxels in neonates. Compared to whole gray or white matter segmentation with a DSC of 96 % and 95 %, respectively (Gabr et al., 2020), the claustrum segmentation achieved a lower performance. However, the accuracy is in accordance with other studies of small brain structures like the hypothalamus with a DSC of 51-84 % depending on the region of interest (Billot et al., 2020). Thus, according to circumstances, transfer learning showed successful performance in neonatal brain MRI.

Comparing the proposed TL approach with non-TL, both methods achieved comparable performance. While the non-TL model was superior regarding HD95, TL showed higher VS in five-fold cross-validation. By TL, the training time could be reduced to 11 % of non-TL. We could not observe an improvement by TL for small samples as proposed by van Opbroek

et al. (2015). Still, our findings are in line with other deep learning studies showing little or no accuracy improvement by TL (Karimi et al., 2020). In total, TL showed comparable performance and was far more time and energy efficient than non-TL, suggesting TL for new projects.

Only twelve scans were needed for stable performance of TL or non-TL models regarding all three evaluation metrics. This is less than in the adult study where 75 samples were needed for high performance (Li et al., 2021). The discrepancy could be partly attributed to a higher image resolution in the neonatal dataset leading to more slices for training. Another aspect might be data augmentation tested by a further experiment. Data augmentation could reduce the needed amount of training data and improved the model performance consistent with other studies (Billot et al., 2020; Chlap et al., 2021). Automated segmentation can immensely reduce the manual workload in large cohorts. Even with correction, there remains a large gain of time.

### 4.3.2 Age-dependent performance

The application of the multi-view model in a large-scale held-out correction set revealed accurate results in 97.4 % of the scans. Correction set means the automated segmentations were compared with manually corrected versions, respectively. This led to a higher accordance than the evaluation with the test set as the exact claustrum border is often ambiguous and the human rater can refer to the proposed annotation when correcting. Hence, only distinctly divergent labels were corrected although a pure manual segmentation might have varied more. The analysis revealed an accuracy drop in the youngest subjects. A possible explanation might be the more immature brain including less gyrification and a different contrast appearance due to ongoing macro- and microstructural brain development (Makropoulos et al., 2018a; Stiles and Jernigan, 2010). We recommend visual quality control at least for subjects younger than gestational age (GA) of 35 weeks or scans with a detected claustrum volume distinctly below average.

An age-stratified training set led to higher performance. A feature of the neonatal cohort in comparison with adults is that brain development substantially impacts the anatomy and MRI appearance of the subjects scanned in a time range of GA 29.3-45.1 weeks (Makropoulos et al., 2018a; Stiles and Jernigan, 2010). Because of the accuracy drop in the youngest subjects, a new multi-view model was trained with a training set including two subjects scanned before 30 gestational weeks. It achieved a significantly higher performance in a group of five

subjects scanned before GA of 33 weeks and in the originally defined test set with older neonates, supporting the theory that a broader training set is essential for a diverse task. We recommend an age-stratified training set for future deep learning projects in a developing cohort.

### 4.3.3 Strengths and limitations

Despite the efficient training and high performance of the developed automated claustrum segmentation in neonatal brain MRI, this study has some limitations: 1) claustrum segmentation generally is challenging even for human raters. The structure is small and intricate and thus, hard to delimitate even in high-resolution images. A structured segmentation protocol for manual segmentation and correction of automated segmentations diminishes the subjective impact; 2) the model performance dropped in preterm-born neonates scanned before GA of 35 weeks. The applicability analysis limited the extent of this decline. A subsequent age-stratification of the training set solved the problem and these new models are also available on GitHub. A close visual control in subjects younger than GA of 35 weeks is recommended; 3) the manual segmentations in the training and test set were conducted by one rater. This might lead to a personal bias in automated segmentations. However, the segmentation is consistent throughout the scans; 4) the model was exclusively trained with images from one scanner. A domain bias in terms of an accuracy drop in scans from other scanners has to be expected. For these cases, further transfer learning with a small number of scans from other scanners is imaginable.

To conclude, we successfully developed a multi-view deep learning model for automated claustrum segmentation in T2-weighted neonatal brain MRI by transfer learning from adult scans. The method was optimized by data augmentation, compared with non-transfer learning, and analyzed in terms of the needed amount of training data. The proposed multi-view transfer learning model was a bit inferior to intra-rater reliability but outperformed inter-rater reliability. It showed high accuracy in most of the subjects in a large neonatal cohort. The transfer learning approach showed comparable performance to non-transfer learning with more time-efficient training. Twelve scans were sufficient to train an accurate model. Finally, age-stratified training improved the overall model performance. Code and models are publicly available on GitHub.

# 5 Claustrum structure in preterm- and term-born neonates

Based on the previous findings of altered claustrum microstructure in preterm-born adults (Hedderich et al., 2021) and the overlap of the claustrum development with vulnerable transient cell populations, namely subplate neurons and pre-oligodendrocytes (Bruguier et al., 2020; Kinney and Volpe, 2018; Puelles, 2014; Volpe, 2019), we hypothesized that the claustrum structure is already altered in preterm-born neonates.

## 5.1 Methods

To investigate the claustrum structure in preterm and term-born neonates, the claustrum segmentations described above (section 4) were applied to acquire macro- and microstructural measures.

### 5.1.1 Overview and dataset selection

The underlying dataset of this study, the second data release of the developing Human Connectome Project (dHCP), is described in detail in section 3. At this point, the data selection for each analysis, i.e., a subset of the entire dataset, is explained (Table 10).

The main aim of this study is to analyze the impact of preterm birth on the claustrum structure in neonates. However, brain development is still ongoing after birth in the scan age range from GA 29.3 to 45.1 weeks (Makropoulos et al., 2016; Stiles and Jernigan, 2010). Thus, we prepend a context analysis of the claustrum development: first, in a spectrum of all available term-born neonates (Table 10B), and second, in preterm-born neonates who were scanned twice for a longitudinal survey (Table 10C).

Regarding the main analysis, to examine the impact of preterm birth on the claustrum structure, we compared preterm- and term-born neonates at scan age-equivalent terms. All preterm-born neonates scanned in the scan age range of term-born neonates from 37.4 to 44.9 gestational weeks were paired with term-born subjects with a minimal scan age gap for term-equivalent conditions. This selection resulted in 83 preterm- and 83 term-born subjects with T2 scans and 72 diffusion-weighted scans, respectively (Table 10D).

***Table 10: Overview of datasets and analyses.***

| Dataset/Analysis | | Image sequence | Term-born scans (male) | Mean scan age (±SD) in GA (weeks) | Preterm-born scans (male) | Mean scan age (±SD) in GA (weeks) |
|---|---|---|---|---|---|---|
| A | dHCP (second data release) | T2<br>dMRI | 378 (205)<br>327 (175) | 41.1 (±1.7)<br>40.9 (±1.7) | 180 (112)<br>163 (102) | 37.8 (±3.7)<br>37.6 (±3.6) |
| B | Context claustrum development 1: Claustrum structure across term-born spectrum | T2<br>dMRI | 377 (205)<br>326 (175) | 41.1 (±1.7)<br>40.9 (±1.7) | | |
| C | Context claustrum development 2: Preterm claustrum development (longitudinal) | 1st T2<br>2nd T2 | | | 53 (34)<br>53 (34) | 34.3 (±1.9)<br>41.2 (±1.5) |
| | | 1st dMRI<br>2nd dMRI | | | 45 (28)<br>45 (28) | 34.5 (±1.7)<br>41.3 (±1.5) |
| D | Main study: Impact of preterm birth | T2<br>dMRI | 83 (48)<br>72 (41) | 41.1 (±1.7)<br>40.9 (±1.7) | 83 (51)<br>72 (45) | 41.1 (±1.7)<br>41.0 (±1.7) |

*The Table shows the image number and scan age distribution of (A) the second data release of the developing Human Connectome Project (dHCP), (B) the spectrum of term-born neonates to examine the claustrum development, (C) longitudinally scanned preterm-born neonates to analyze the claustrum development after preterm birth, and (D) the comparison analysis of preterm- and term-born neonates. Table reproduced with slight adaptions from Neubauer et al. (2023), used under CC By. dMRI = diffusion-weighted MRI, GA = gestational age, SD = standard deviation.*

### 5.1.2 Macro- and microstructural metrics

The claustrum macrostructure was evaluated with two metrics, absolute and total brain volume (TBV-) relative claustrum volume. These measures were defined in a voxel-based manner, i.e., the absolute claustrum volume equals the sum of the individual voxels labeled as claustrum. TBV was defined as the sum of gray and white matter including the brainstem for each brain while cerebrospinal fluid and ventricles were excluded. TBV-relative claustrum volume equals the volume of the right and left claustrum divided by the TBV.

The claustrum microstructure was also evaluated with two measures, mean diffusivity (MD) and fractional anisotropy (FA). MD represents the mean squared diffusion of protons in the frame of water molecules possibly with an emphasis on the extracellular space (Beaulieu, 2002; Hedderich et al., 2021; Le Bihan, 2003). The unit of MD is $mm^2/s$. It is defined as the average of the three eigenvalues "$\lambda_{1-3}$" which equal the length of the eigenvectors (Basser and Pierpaoli, 1996):

$$MD = \frac{\lambda_1 + \lambda_2 + \lambda_3}{3} \quad (6)$$

The three eigenvectors represent the water diffusion in the three spatial dimensions (Basser et al., 1994).

FA depicts how directed the water diffusion takes place in each voxel. It has an arbitrary unit between 0, isotropic diffusion, and 1, anisotropic diffusion. Assuming that $\lambda_1$, $\lambda_2$, and $\lambda_3$ are the eigenvalues of the three dimensions, FA is charged by this formula (Mori and Zhang, 2006; Mukherjee et al., 2008; Pierpaoli and Basser, 1996):

$$FA = \frac{\sqrt{((\lambda_1 - \lambda_2)^2 + (\lambda_2 - \lambda_3)^2 + (\lambda_3 - \lambda_1)^2)}}{\sqrt{2 \cdot (\lambda_1{}^2 + \lambda_2{}^2 + \lambda_3{}^2)}} \quad (7)$$

The dHCP provides 490 preprocessed dMRI data (see section 3.3). We further processed the dataset to gain the desired maps. First, preprocessed 4D volumes, the corresponding brain masks, b-values, and b-vectors (post-eddy rotated gradient directions) were converted to MD and FA maps with FSL (version 6.0.4). In a second step, these maps were transformed to T2w space by rigid-body transformation prepared by the dHCP (Andersson et al., 2007; Bastiani et al., 2019a; Greve and Fischl, 2009; Jenkinson et al., 2002) in FSL with a trilinear interpreter. A subsequent quality check was performed on a sample basis. Finally, the claustrum masks were applied to the diffusion maps to gain claustrum MD and FA.

As the claustrum is a delicate structure with a large surface to white matter, two control measures were acquired (Figure 20). First, a claustrum frame was defined as the claustrum surrounding white matter of around two voxels. Second, the "claustrum-controlled" segmentation labels the inner voxels of the original claustrum segmentation enclosed by other claustrum voxels for at least 90 %.

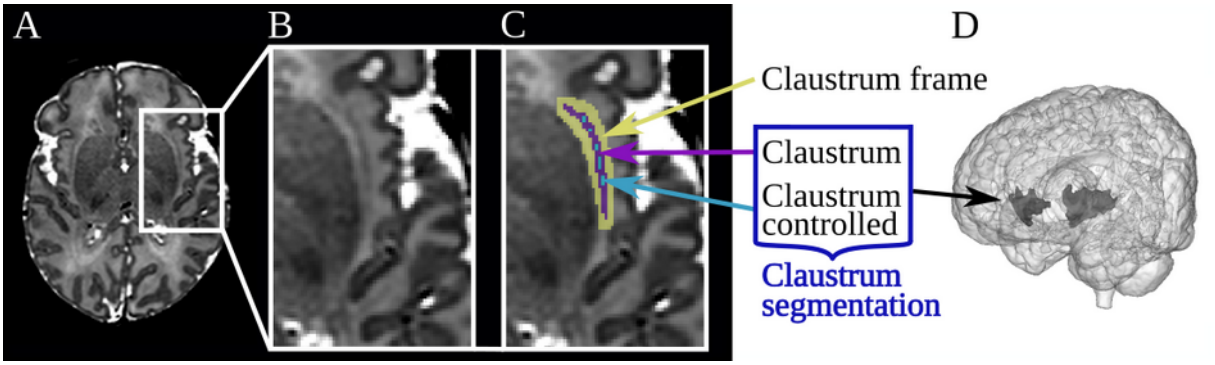


***Figure 20: Claustrum segmentation in neonatal brain MRI.***

*(A) Axial slice of a T2-weighted brain MRI of a term-born neonate at the gestational age of 38 weeks. (B) Enlarged image section of the left claustrum. (C) Left claustrum segmentation with control labels, claustrum frame and claustrum-controlled. (D) Rendered 3D brain with the annotated right and left claustrum. Figure reproduced from Neubauer et al. (2023), used under CC By.*

All other regional labels used in the following analyses were acquired from the Draw-EM coregistration provided by the dHCP (Makropoulos et al., 2018b, 2014).

### 5.1.3 Statistical analysis

The data analysis was separated into two parts, first, claustrum development, and second, the impact of prematurity. All investigations included four metrics, namely claustrum volume, TBV-relative claustrum volume, MD, and FA, which are described as "four claustrum metrics" in the following description.

First, as a context survey, we examined the claustrum development. We conducted a spectrum analysis including all term-born subjects scanned between GA 38 to 45 weeks in a general linear model approach (GLM) with the four claustrum metrics as dependent variables, respectively, scan age as the independent variable, and corrected for sex and birth age. Furthermore, a paired t-test was performed to compare the first and second scans of double-scanned preterm-born subjects regarding the four claustrum metrics, respectively. To estimate a selection bias, the subjects scanned twice were demographically compared with preterm-born subjects scanned once. Additionally, these two groups of preterm-born neonates were included in a linear mixed model analysis with the four claustrum metrics as dependent variables, respectively, scan age as the independent variable, and birth age, sex, and random intercepts for individual subjects as covariates of no interest. The analyses were performed for averaged right and left claustrum as an overview, and for right and left claustrum, separately.

Second, as the main analysis, we investigated the impact of preterm birth on the claustrum macro- and microstructure, i.e., the same four claustrum metrics as above, namely absolute and TBV-relative claustrum volume, MD and FA. To achieve scan age-equivalent conditions, all preterm-born neonates scanned in the scan age range of term-born neonates were included. Subsequently, each preterm-born subject was matched with a term-born subject with a minimal scan age gap. A GLM approach was applied with the four claustrum metrics as dependent variables, respectively. Preterm birth was the categorical independent variable and the model was corrected for scan age and sex. The analyses were performed for averaged right and left claustrum as an overview, and for right and left claustrum, separately.

The main analyses were further controlled: Concerning the selection of term-born controls for the comparison study of preterm- and term-born subjects, the term-born neonates included in this evaluation were compared demographically with the term-born subjects who were not included. In a second approach, the preterm-born neonates scanned in the scan age range of term-born neonates were compared with all available term-born neonates in a GLM correcting for scan age and sex. To test for specificity of the claustrum macrostructure alteration, the evaluation of TBV-relative claustrum volume was repeated with TBV-relative volumes of the thalamus and caudate nucleus in GLM analyses, respectively. To test for specificity of the microstructural claustrum alterations regarding the boundary area, the GLM approaches with claustrum MD and FA were repeated with claustrum-controlled segmentations (Figure 20C, light blue). To control for the general effects of preterm birth on gray matter microstructure, the GLM approach for claustrum MD and the approach for claustrum-controlled MD were repeated with the total gray matter MD, i.e., MD of cortical and subcortical GM, as further correcting variable. Additionally, the GLM approach for FA was replicated with further covariates, i.e., the lentiform nucleus (i.e., putamen and globus pallidus), insular cortex, and white matter area around the claustrum (i.e., the intersection of a boundary around the claustrum with a width of around two voxels on all sides with the insular white matter defined by the provided Draw-EM atlas; Figure 20C, yellow) to evaluate the mingling with surrounding structures.

Statistical analyses were conducted with R (version 3.6.3). Statistical significance was set to $p < 0.05$.

### 5.1.4 Claustrum covariance analysis

Moreover, we compared preterm- and term-born covariance of claustrum absolute and TBV-relative volume, MD, and FA, respectively, with the corresponding metrics of all regions registered in the Draw-EM atlas (Gousias et al., 2012; Makropoulos et al., 2014). The analysis was inspired by a previous claustrum correlation analysis in adults (Berman et al., 2020). The Pearson correlation coefficients r were calculated between the claustrum and all other gray and white matter regions, separated for the right and left claustrum. For comparison reasons, the r-scores were converted into z-scores by Fisher r-to-z-transformation. P-values were determined based on the difference between the preterm- and term-born z-scores. Subsequently, the p-values were adjusted by a false discovery rate correction for absolute and TBV-relative claustrum volume, MD, and FA, respectively, to revise for multiple testing. Statistical significance was set to $p < 0.05$. The observed z-scores and differences between preterm- and term-born neonates were visualized in brain plots created with the Visualization Toolkit vtk (version 9.1.0) in python (version 3.8.10) and with ITK-SNAP (version 3.6.0, https://www.itksnap.org) (Yushkevich et al., 2006). The python code for the plots was published on GitHub (https://github.com/cor2ni/3D_brain_plot).

## 5.2 Results

To investigate the claustrum in neonatal brain MRI, the scans were examined regarding two concerns: First, we conducted a background analysis of the structural claustrum development in term- and preterm-born neonates. Second, the claustrum macro- and microstructure were compared between these groups.

### 5.2.1 Context: Claustrum development

To examine the macro- and microstructural claustrum development as the contextual background of the impact of prematurity, we performed first, a spectrum analysis of term-born neonates and second, a longitudinal examination with preterm-born subjects scanned twice.

#### 5.2.1.1 Term-born neonates

To investigate the physiological macro- and microstructural development, we measured the absolute and total brain volume (TBV-) relative claustrum volume, claustrum MD, and FA. Macrostructure was analyzed in a spectrum of all available 377 term-born subjects (Table 10B). The scans were acquired between GA 38 to 45 weeks. The mean absolute and relative volume of the right and left claustrum of each subject were plotted along scan age (Figure 21), respectively. Regarding the absolute claustrum volume, the distribution suggested a volume increase with higher scan age. To confirm this assumption, we applied a GLM approach with mean claustrum volume as the dependent variable, scan age as the independent variable, and correction for birth age and sex. We found that the claustrum volume significantly increased with higher scan age (regression coefficient $r = 14.6$, $p < 0.001$, partial $\eta^2 = 0.11$). Thereby, the right claustrum showed a higher growth rate in this period than the left one ($r_{right} = 17.1$, $p_{right} < 0.001$, $r_{left} = 12.1$, $p_{left} < 0.001$) (Figure 22A). The result suggests continuously growing claustra in the observational period around term.

The TBV-relative claustrum volume, i.e., the volume of the right and left claustrum divided by the TBV, is a volume measure corrected for total brain growth. Thereby, TBV equals the sum of gray and white matter including the brainstem and excluding cerebrospinal fluid and ventricles. In parallel to the GLM approach for absolute claustrum volume, the TBV-relative claustrum volume was the dependent variable for this analysis. The TBV-relative claustrum volume significantly decreased from GA 38 to 45 weeks ($r = -0.048*10^{-3}$, $p < 0.001$, partial $\eta^2 = 0.15$). There was a stronger decline in the left TBV-relative claustrum volume in comparison with the right ($r_{right} = -0.000018$, $p_{right} < 0.001$, $r_{left} = -0.000030$, $p_{left} < 0.001$)

(Figure 22B). In summary, the results indicate a faster growth of TBV compared with the claustrum volume increase around term.

The microstructural claustrum development analysis followed the same approach. We included all diffusion-weighted scans available from term-born neonates comprising 326 subjects. The mean values of right and left claustrum MD and FA were plotted along scan age, respectively (Figure 21). The distribution of MD suggested an MD decrease with higher scan age. To quantify this trend, we deployed a GLM approach in parallel to the volume analysis with mean claustrum MD ($*10^{-3}$ mm²/s) as the dependent variable, scan age as the independent variable, and correction for birth age and sex. We found a significantly lower claustrum MD in older neonates ($r = -12.7*10^{-3}$, $p < 0.001$, partial $\eta^2 = 0.41$), suggesting a perinatal claustrum MD decrease. This also applies to the right and left claustrum separately ($r_{right} = -0.012$, $p_{right} < 0.001$, $r_{left} = -0.014$, $p_{left} < 0.001$) (Figure 22C). Setting the claustrum MD development in relation to the global cortical and subcortical gray matter MD shift, we added this general GM MD as an additional independent covariate in the GLM. The negative correlation between scan age and claustrum MD was still significant ($r = -13.8*10^{-3}$, $p < 0.001$, partial $\eta^2 = 0.44$). This indicates a claustrum MD change independently from other GM regions.

In contrast to the MD decrease, there is an FA increase apparent in the plot (Figure 21D). In parallel to MD analysis, we performed a GLM approach with mean claustrum FA of right and left claustrum as the dependent variable and scan age as the independent variable. The model was corrected for birth age and sex. The claustrum FA was significantly higher in older neonates ($r = 5.5*10^{-3}$, $p < 0.001$, partial $\eta^2 = 0.26$), suggesting an FA increase around term which was slightly more pronounced in the left claustrum ($r_{right} = 0.0050$, $p_{right} < 0.001$, $r_{left} = 0.0060$, $p_{left} < 0.001$) (Figure 22D). To test if the finding is a global trend in gray matter, we further controlled the analysis by adding general GM FA, i.e., mean FA of cortical and subcortical GM, as an independent covariate in the GLM. There was still a positive correlation between claustrum FA and scan age ($r = 9.1*10^{-3}$, $p < 0.001$, partial $\eta^2 = 0.37$), indicating that the observed claustrum FA shift is not completely explainable by general GM FA changes.

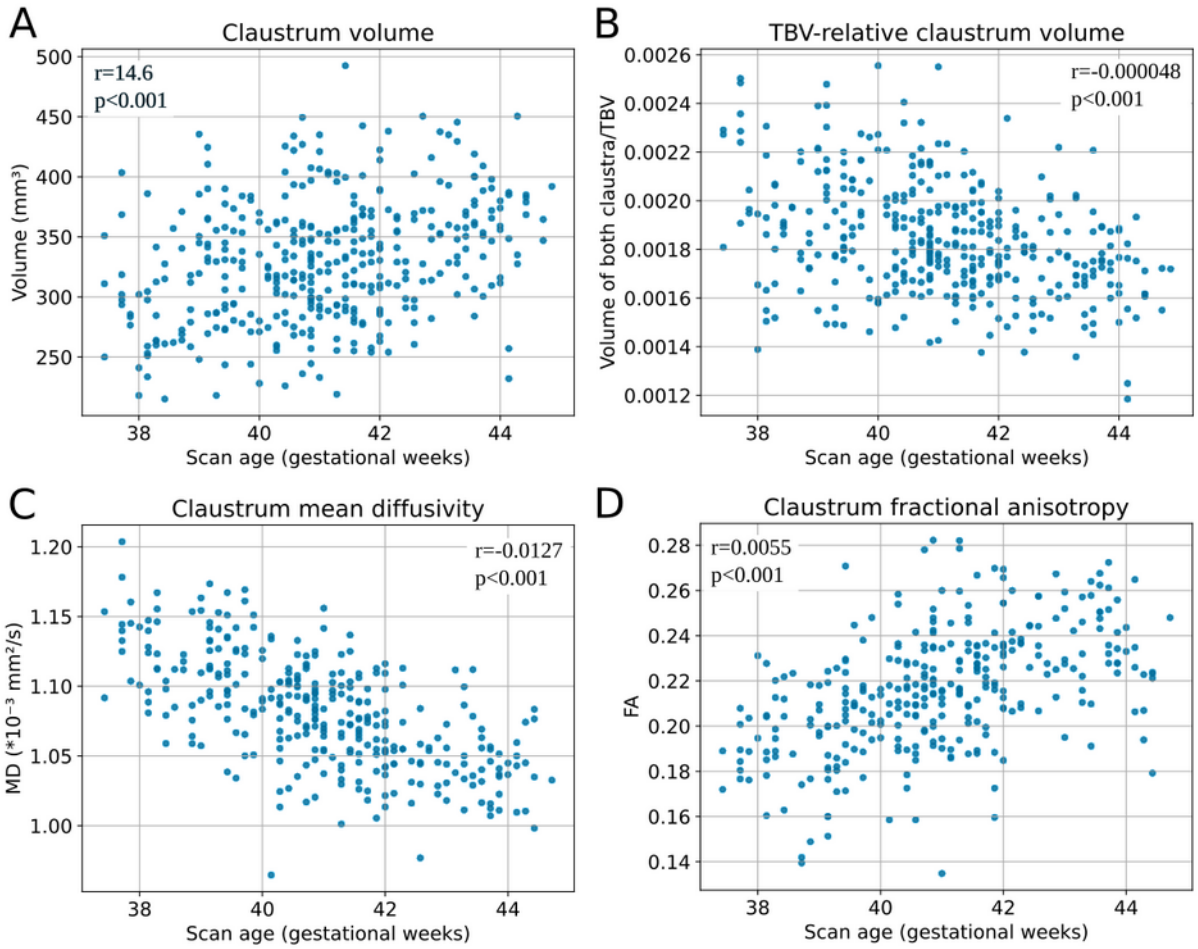


***Figure 21: Spectrum analysis in term-born neonates.***

*(A) The claustrum volume increased in a spectrum of 377 term-born neonates while (B) the total brain volume (TBV-) relative claustrum volume decreased with higher scan age. In a spectrum of 326 neonates, (C) the claustrum mean diffusivity (MD) decreased and (D) the claustrum fractional anisotropy (FA) increased. A general linear model approach revealed the regression coefficients r and p-values correcting for birth age and sex. Figure adapted from Neubauer et al. (2023), used under CC By.*

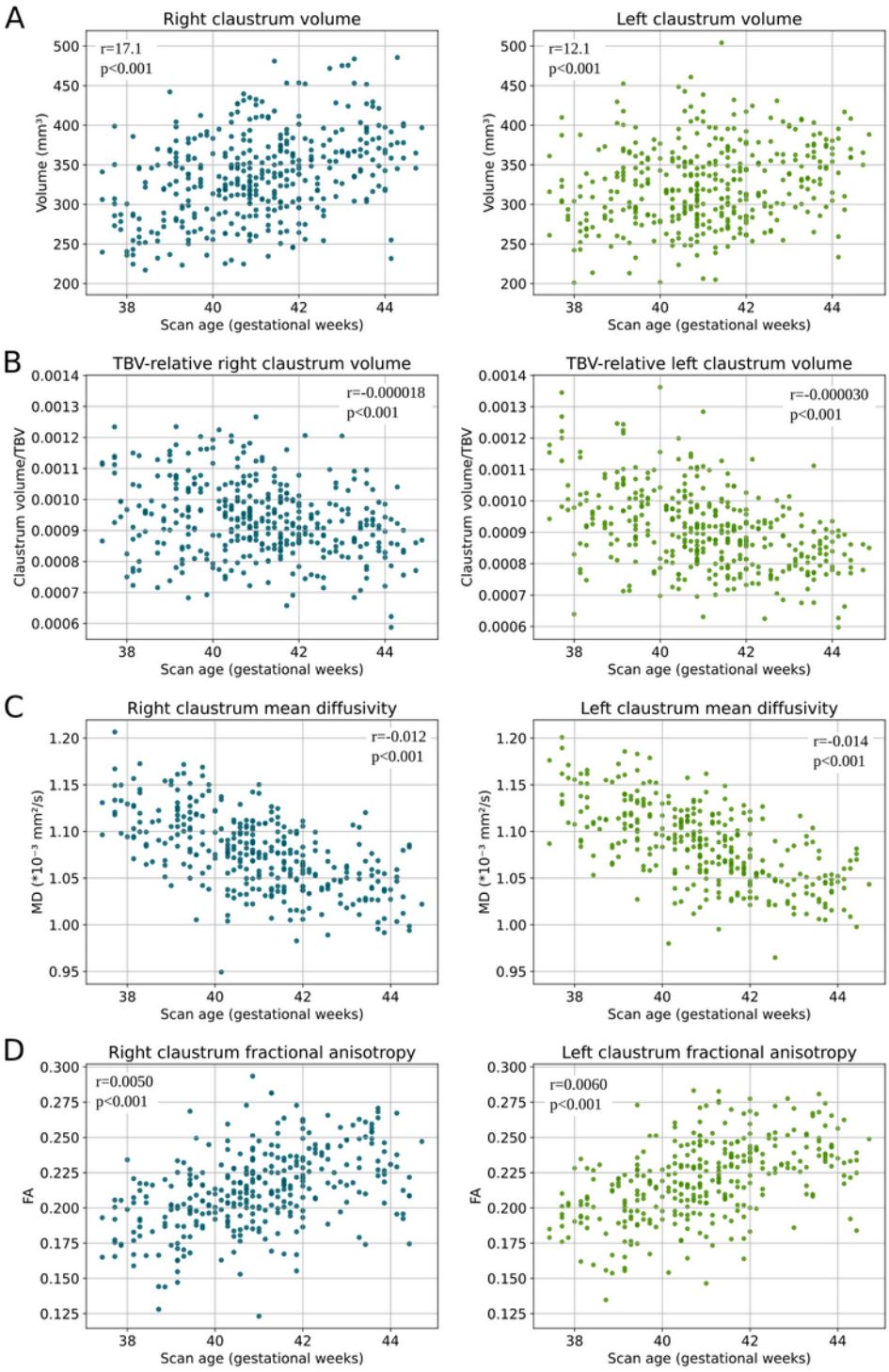


***Figure 22: Right and left claustrum structure in a spectrum of term-born neonates.***

*In a spectrum of 377 term-born neonates, (A) the absolute claustrum volume was rising and (B) the total brain volume (TBV-) relative claustrum volume was decreasing with increasing scan age. In a spectrum of 326 term-born neonates, (C) the claustrum mean diffusivity (MD) was decreasing, while (D) the claustrum fractional anisotropy (FA) was increasing with higher scan age. A general linear model approach revealed the regression coefficients r and p-values correcting for birth age and sex. Figure adapted from the Online Supplement of Neubauer et al. (2023), used under CC By.*

#### 5.2.1.2 Preterm-born neonates

To evaluate the macro- and microstructural claustrum development in preterm-born neonates, we performed a longitudinal study with all subjects who were scanned twice (Table 10C) and an embedding study with all preterm-born subjects. For neonates scanned twice, the first scans were acquired in the first days after birth while the second scans were acquired a few weeks later around term. Overall, the scans cover a range of GA 30 to 45 weeks. On average, subjects with two scans had a lower birth age and birth weight (Table 11). To assess the claustrum macrostructure, we plotted the absolute and TBV-relative claustrum volumes of the first and second scans of 53 subjects along scan age (Figure 23), respectively. The distribution suggested absolute claustrum volume increase with increasing scan age. We performed a paired t-test between the mean claustrum volume of the first and second scans of preterm-born neonates scanned twice. There was a significantly larger claustrum in the second scan (t-statistic = 14.1, $p < 0.001$), as well as in right and left claustrum separately ($t_{right} = 14.9$, $p_{right} < 0.001$, $t_{left} = 12.1$, $p_{left} < 0.001$) (Figure 24A), suggesting a claustrum growth in the early postnatal period. Additionally, we analyzed all available 180 scans of 128 preterm-born neonates with a linear mixed model approach controlling for sex, birth age, and random intercepts for individual subjects. Likewise, the claustrum volume increased over time (regression coefficient $r = 16.6$, $p < 0.001$) with a slightly higher growth rate in the right claustrum ($r_{right} = 17.8$, $p_{right} < 0.001$, $r_{left} = 15.1$, $p_{left} < 0.001$) (Table 12).

In contrast, the TBV-relative claustrum volume seems to decrease from the first to the second scan in many but not in all subjects. Again, we performed a paired t-test and linear mixed models in parallel to the absolute claustrum volume. There was a significant decrease between the TBV-relative claustrum volume of the first and second scan (t-statistic = -3.9, $p < 0.001$) with emphasis on the left side and no significant change on the right side ($t_{right} = -1.14$, $p_{right} = 0.26$, $t_{left} = -6.33$, $p_{left} < 0.001$) (Figure 24B). A linear mixed model with all 180 scans reproduced the results ($r = -0.000026$, $p < 0.001$) except for the fact, that there was also a significant minimal decrease of the TBV-relative right claustrum volume with increasing scan age ($r_{right} = -0.000008$, $p_{right} = 0.010$, $r_{left} = -0.000018$, $p_{left} < 0.001$) (Table 12). Together, the findings suggest that the claustrum volume, especially the left claustrum, increases slower than the TBV volume in the observational period. However, regarding the longitudinally scanned neonates, the TBV-relative claustrum volume increased in 34 % of the subjects

between the first and second scans. Why not all subjects show the same trend remains open at this place.

For the microstructural analysis, claustrum MD and FA of the first and second scans of 45 preterm-born subjects were plotted along scan age, respectively (Figure 23C and D). As for the macrostructural analysis, the subjects span a period from GA 30 to 45 weeks. To examine the MD development, we conducted a paired t-test between the mean claustrum MD of the first and second scans. We found a significant MD decrease in the second scans (t-statistic = -11.1, $p < 0.0001$) with only a small difference between right and left claustrum ($t_{right} = -9.24$, $p_{right} < 0.001$, $t_{left} = -11.6$, $p_{left} < 0.001$) (Figure 24C). The performed linear mixed model approach including 163 scans of 119 preterm-born subjects, correcting for birth age, sex, and random intercepts for individual neonates, reproduced the mean results ($r = -0.014$, $p < 0.001$) and the findings for right and left claustrum MD ($r_{right} = -0.014$, $p_{right} < 0.001$, $r_{left} = -0.015$, $p_{left} < 0.001$) (Table 12). The described MD decrease suggests an ongoing microstructural development of the claustrum around term.

To evaluate the FA development in preterm-born neonates, the same paired t-test and linear mixed model approaches were applied but with claustrum FA as the dependent variable. We found a significant increase of claustrum FA over time (t-statistic = 10.3, $p < 0.0001$) (Figure 23D) with a marginally higher increase of the left claustrum ($t_{right} = 9.39$, $p_{right} < 0.001$, $t_{left} = 10.4$, $p_{left} < 0.001$) (Figure 24D). The linear mixed model also showed an increasing claustrum FA over time ($r = 0.0067$, $p < 0.001$) with a slightly pronounced rise in the left claustrum FA ($r_{right} = 0.0062$, $p_{right} < 0.001$, $r_{left} = 0.0071$, $p_{left} < 0.001$) (Table 12). Combined with the MD decrease described above, the findings indicate a microstructural claustrum development in the postnatal period.

***Table 11: Demographic overview of preterm-born neonates.***

| **Preterm-born subjects *of the developing Human Connectome Project, second data release*** | **Subjects (Male)** | **Singles/ Multiples** | **Birth age in gestational weeks (Mean (± SD))** | **Birth weight in kg (Mean (± SD))** |
|---|---|---|---|---|
| Only one T2-weighted scan available | 76 (44) | 45 / 31 | 32.9 (±3.6) | 1.95 (±0.72) |
| Two T2-weighted scans available | 53 (34) | 34 / 19 | 32.0 (±3.0) | 1.69 (±0.66) |
| Only one diffusion scan available | 75 (46) | 46 / 29 | 32.9 (±3.5) | 1.92 (±0.72) |
| Two diffusion scans available | 45 (28) | 29 / 16 | 32.2 (±3.0) | 1.74 (±0.66) |

*Table adapted from the Online Supplement of Neubauer et al. (2023), used under CC By. SD=standard deviation.*

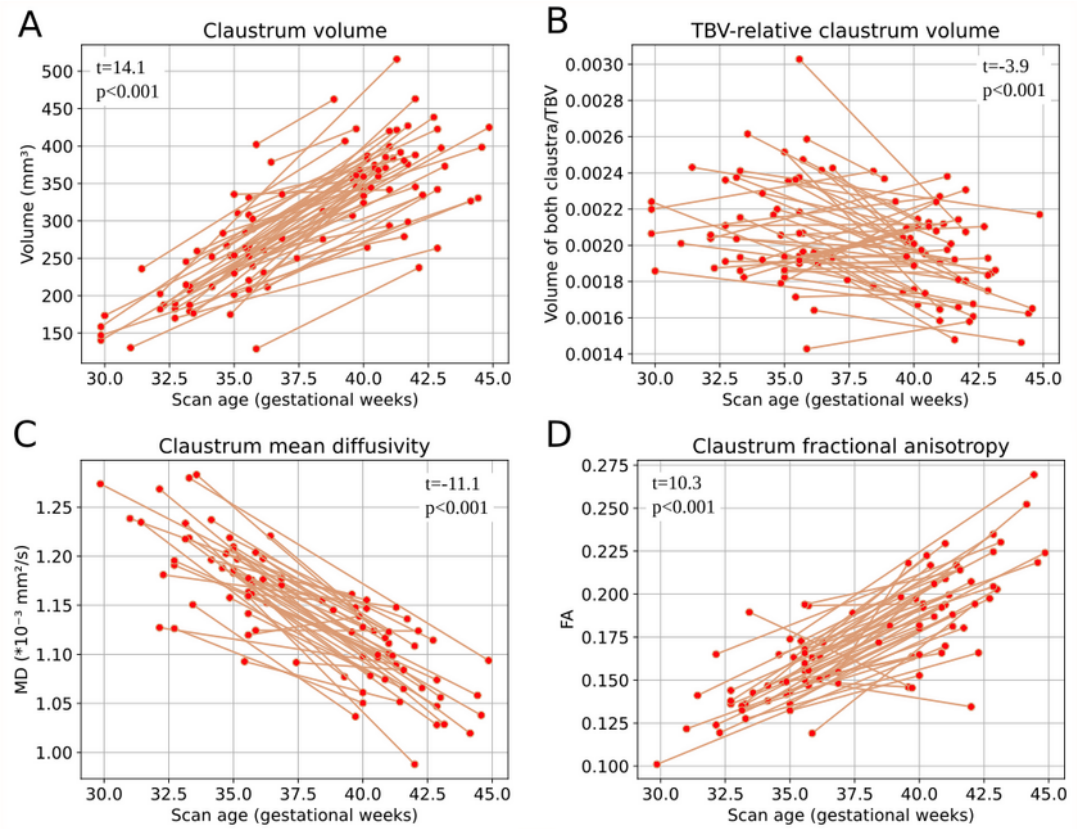


***Figure 23: Longitudinal analysis of preterm-born neonates.***

*(A) Analyzing 53 subjects scanned twice, the claustrum volume increased over time while (B) the total brain volume (TBV-) relative claustrum volume decreased, at least in several subjects, with higher scan age. (C) The claustrum mean diffusivity (MD) decreased and (D) the claustrum fractional anisotropy (FA) increased in 45 preterm-born neonates scanned twice. T-statistics and related p-values were calculated with paired t-tests, respectively. Figure adapted from Neubauer et al. (2023), used under CC By.*

***Table 12: Claustrum development in preterm-born neonates.***

| **Metric** | $r_{mean}$ | $p_{mean}$ | $r_{right}$ | $p_{right}$ | $r_{left}$ | $p_{left}$ |
|---|---|---|---|---|---|---|
| Claustrum volume (mm³) | 16.6 | **<0.001** | 17.8 | **<0.001** | 15.1 | **<0.001** |
| TBV-relative claustrum volume | -0.000026 | **<0.001** | -0.000008 | **0.010** | -0.000018 | **<0.001** |
| Claustrum MD ($10^{-3}$ mm²/s) | -0.014 | **<0.001** | -0.014 | **<0.001** | -0.015 | **<0.001** |
| Claustrum FA | 0.0067 | **<0.001** | 0.0062 | **<0.001** | 0.0071 | **<0.001** |

*The regression coefficients r and p-values were calculated with linear mixed models with 180 T2-weighted scans for absolute and TBV-relative claustrum volume, respectively, and 163 diffusion-weighted scans for claustrum mean diffusivity (MD) and fractional anisotropy (FA), respectively. The models were corrected for birth age, sex, and random intercepts for individual subjects. Significant p-values are written in bold letters. Table reproduced with little formatting from the Online Supplement of Neubauer et al. (2023), used under CC By. TBV = total brain volume.*

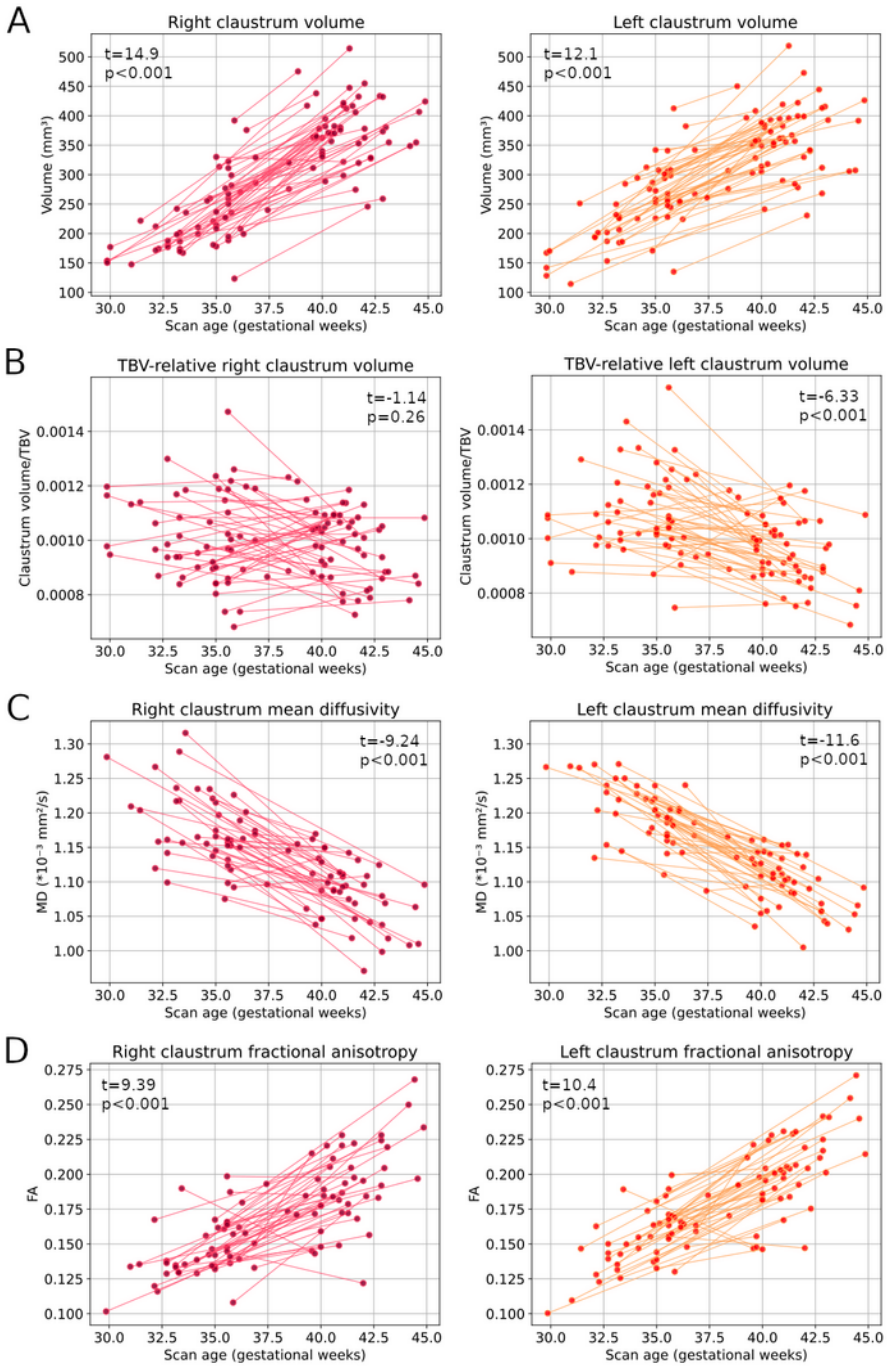


***Figure 24: Right and left claustrum structure in longitudinally scanned preterm-born neonates.***

*Macrostructure: (A) The absolute claustrum volume was rising, (B) the total brain volume (TBV-) relative claustrum volume was decreasing from the first to the second scan of 53 preterm-born neonates with increasing scan age. Microstructure: (C) The claustrum mean diffusivity (MD) was decreasing, while (D) the claustrum fractional anisotropy (FA) was increasing from the first to the second scan of 45 preterm-born neonates with increasing scan age. T-statistics and p-values were calculated with paired t-tests of the first and second scan of a subject building a pair, respectively. Figure adapted from the Online Supplement of Neubauer et al. (2023), used under CC By.*

### 5.2.2 Impact of prematurity on the claustrum structure

As the main analysis, we examined the impact of preterm birth on the claustrum macro- and microstructure. Furthermore, the effect of prematurity on correlation ratios between right and left claustrum and spread cortical and subcortical gray and white matter regions was evaluated. In a first approach, the term-born and preterm-born subjects were selected in a balanced manner: All preterm-born subjects (PT) scanned in the scan age range of the term-born subjects (GA 37.4 to 44.9 weeks) were chosen and paired with term-born correlates (full term, FT) with a minimal scan age gap (Table 10D). This results in age-equivalent conditions to reduce the impact of ongoing brain and claustrum development as shown in the background analysis above. Term-born controls selected for the comparison study were almost similar to the other term-born subjects not selected regarding birth age and birth weight (Table 13). In a second approach, the same preterm-born neonates were compared with all available term-born subjects under the control of scan age within the statistical model.

***Table 13: Demographics of term-born neonates who were selected or not selected for the scan age-matched comparison study with preterm-born subjects.***

| Term-born neonates | Subjects (Male) | Singles / Multiples | Birth age in gestational weeks (Mean (± SD)) | Birth weight in kg (Mean (± SD)) |
|---|---|---|---|---|
| T2-weighted scans: Neonates included in the analysis pre-vs.-term | 83 (48) | 81 / 2 | 39.9 (±1.2) | 3.34 (±0.56) |
| T2-weighted scans: Neonates who were **not** included | 295 (157) | 280 / 15 | 40.0 (±1.2) | 3.38 (±0.51) |
| Diffusion-weighted scans: Neonates included in the analysis pre-vs.-term | 72 (41) | 70 / 2 | 39.8 (±1.2) | 3.31 (±0.57) |
| Diffusion-weighted scans: Neonates who were **not** included | 255 (134) | 240 / 15 | 39.9 (±1.2) | 3.35 (±0.52) |

*Table adapted from the Online Supplement of Neubauer et al. (2023), used under CC By. SD = standard deviation.*

#### 5.2.2.1 Effect on the claustrum macrostructure

To assess the claustrum macrostructure, we used the metrics absolute and TBV-relative claustrum volume. 83 preterm- (PT) and 83 term-born (full term; FT) neonates, with a scan age between GA 37.4 and 44.9 weeks, were included. The plots of both measures along scan age are shown in Figure 25A and B. To see if there is an absolute volume difference between groups, namely preterm- and term-born neonates, we applied a GLM approach. The mean

volume of the right and left claustrum was the dependent variable and preterm birth was a categorical independent variable. We corrected for scan age and sex. The claustrum volume of preterm-born subjects was significantly larger than in term-born correlates (PT: 360 ± 55 $mm^3$, FT: 332 ± 51 $mm^3$, $p < 0.001$, partial $\eta^2 = 0.07$). This result is also valid for the right and left claustrum separately ($p_{right} = 0.008$, $p_{left} < 0.001$) (Figure 26A and Table 14). Interestingly, the right claustrum is larger than the left claustrum in preterm- and term-born subjects, respectively (Table 14). To exclude a selection bias of the term-born controls, the 83 preterm-born subjects were also compared to all available 377 term-born scans in a GLM approach correcting for scan age and sex. Again, the absolute claustrum volume was significantly increased after preterm birth ($p < 0.001$) (Table 15). This indicates a faster claustrum volume increase in preterm-born neonates than in term-born subjects at least till term-equivalent age.

To exclude a general effect of prematurity on all volumes, we controlled for the total brain volume. Thus, the same GLM approach was performed but this time with TBV-relative claustrum volume, i.e., the volume of the right and left claustrum divided by TBV, as the dependent variable. The TBV-relative claustrum volume was significantly increased after preterm birth (PT: 0.00195 ± 0.00025, FT: 0.00187 ± 0.00026, $p = 0.029$, partial $\eta^2 = 0.03$). However, this result was only significant for the left TBV-relative claustrum volume, i.e., left claustrum volume/TBV, ($p_{left} = 0.006$) and there was no significant difference for the right side ($p_{right} = 0.183$) (Figure 26 and Table 14). Including all available 377 term-born neonates as controls as described above, there was a significantly larger TBV-relative claustrum volume after preterm birth ($p < 0.001$) (Table 15). The results suggest a relatively larger claustrum, with emphasis on the left claustrum, after preterm birth at term-equivalent age independent of the TBV.

To further examine the specificity of the enlarged claustrum, the analysis with age-matched groups of 83 preterm- and 83 term-born neonates was repeated for two other subcortical regions, namely the thalamus and caudate nucleus. In detail, we performed the GLM approach with TBV-relative thalamus volume and TBV-relative caudate nucleus volume as dependent variables, respectively, correcting for scan age and sex. Both, the relative thalamus volume ($p = 0.001$, partial $\eta^2 = 0.07$) and the relative volume of the caudate nucleus ($p = 0.016$, partial $\eta^2 = 0.04$) were significantly smaller in preterm-born neonates in comparison with term-

equivalent term-born subjects. These findings suggest that the larger claustrum volume after preterm birth is specific to the claustrum.

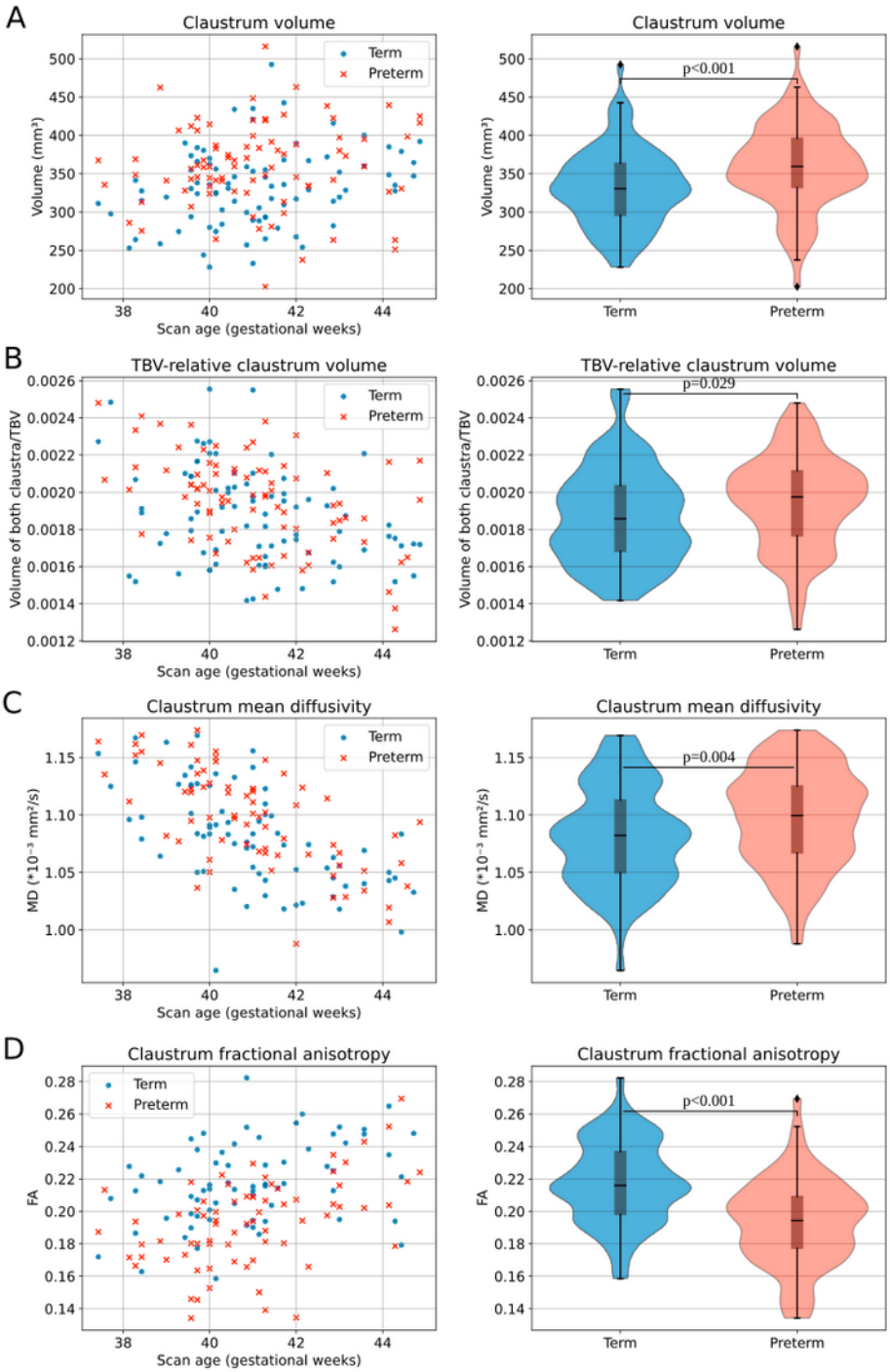


***Figure 25: Comparison of the claustrum structure in scan age equivalent preterm- and term-born neonates.***

*(A) The absolute claustrum volume (B) and the total brain volume (TBV-) relative claustrum volume was increased after preterm birth opposing 83 preterm- and 83 term-born subjects. (C) While the claustrum mean diffusivity (MD) was increased in preterm-born neonates, (D) the claustrum fractional anisotropy (FA) was decreased in the same cohort of 72 preterm- and term-born neonates, respectively. Groups were compared with general linear models correcting for scan age and sex. Figure adapted from Neubauer et al. (2023), used under CC By.*

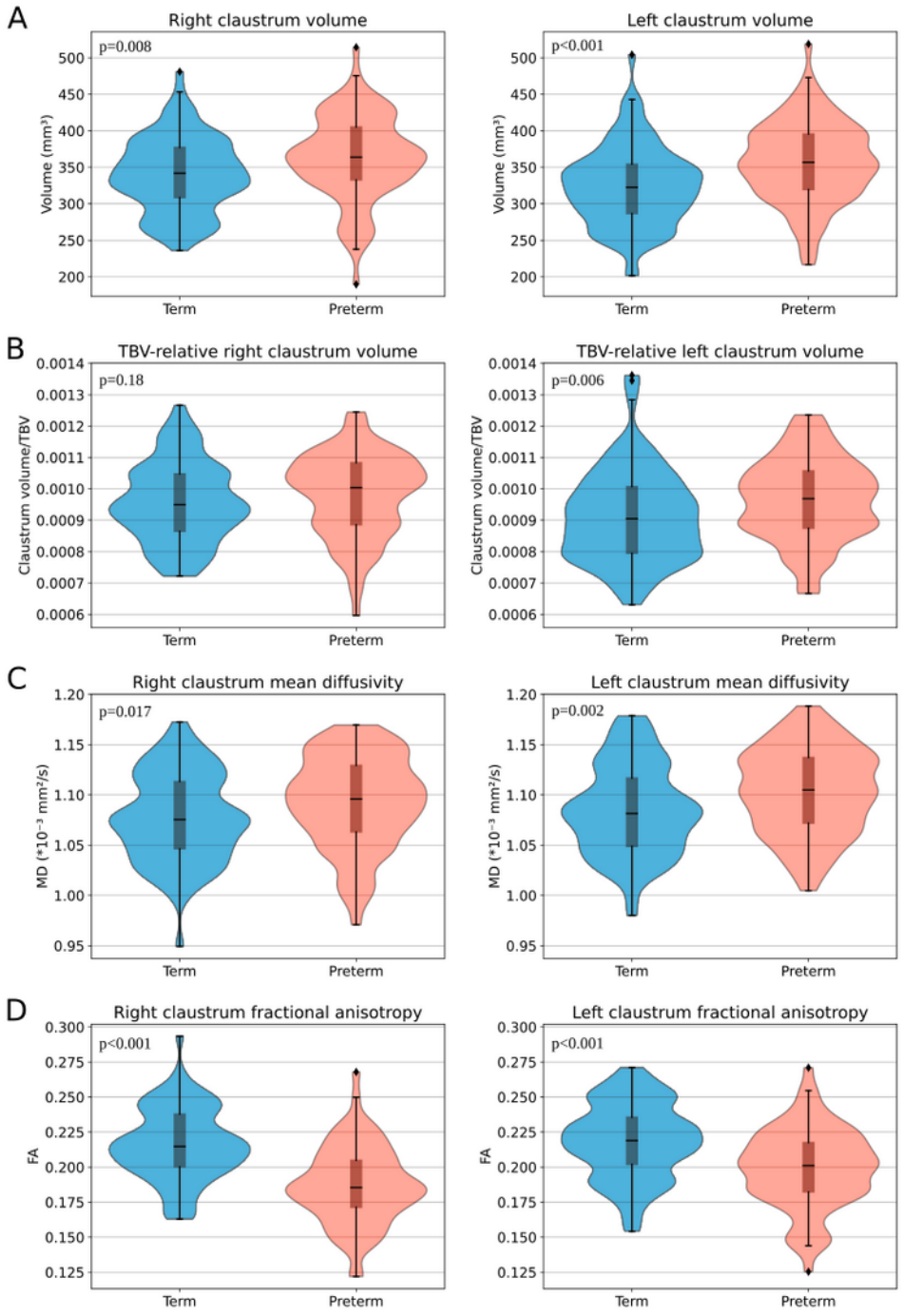


***Figure 26: Comparison of the right and left claustrum structure, separately, in scan age equivalent preterm- and term-born neonates.***

*(A) The absolute claustrum volume (B) and the total brain volume (TBV-) relative claustrum volume was increased after preterm birth opposing 83 preterm- and 83 term-born subjects for the right and left side. However, there was no significant increase in the TBV-relative right claustrum volume. (C) While the claustrum mean diffusivity (MD) was increased in preterm-born neonates, (D) the claustrum fractional anisotropy (FA) was decreased in the same cohort of 72 preterm- and term-born neonates, respectively, for right and left claustrum. Groups were compared with general linear models correcting for scan age and sex. Figure adapted from the Online Supplement of Neubauer et al. (2023), used under CC By.*

***Table 14: Impact of preterm birth on the right and left claustrum, separately.***

| Metric | Term (Mean (± SD)) | Preterm (Mean (± SD)) | p-value | partial $\eta^2$ |
|---|---|---|---|---|
| Right claustrum volume ($mm^3$) | 341 (±51) | 363 (±58) | **0.008** | 0.04 |
| Left claustrum volume ($mm^3$) | 325 (±55) | 357 (±56) | **<0.001** | 0.08 |
| TBV-relative right claustrum volume | 0.00096 (±0.00013) | 0.00098 (±0.00013) | 0.183 | 0.01 |
| TBV-relative left claustrum volume | 0.00091 (±0.00015) | 0.00097 (±0.00013) | **0.006** | 0.05 |
| Right claustrum MD ($10^{-3}$ $mm^2/s$) | 1.08 (±0.04) | 1.09 (±0.05) | **0.017** | 0.04 |
| Left claustrum MD ($10^{-3}$ $mm^2/s$) | 1.09 (±0.05) | 1.10 (±0.04) | **0.002** | 0.07 |
| Right claustrum FA | 0.216 (±0.026) | 0.187 (±0.028) | **<0.001** | 0.26 |
| Left claustrum FA | 0.219 (±0.027) | 0.199 (±0.029) | **<0.001** | 0.13 |

*For absolute and total brain volume (TBV-) relative claustrum volume 83 preterm-born subjects were matched with 83 term-born neonates to reach scan age equivalence. The groups were compared with general linear models additionally correcting for scan age and sex. For claustrum mean diffusivity (MD) and fractional anisotropy (FA), 72 preterm- and term-born neonates, respectively, were analyzed. Significant p-values are written in bold letters. Table reproduced with little formatting from Neubauer et al. (2023), used under CC By. SD = standard deviation.*

***Table 15: Impact of preterm birth on the mean claustrum structure.***

| Metric | Term (Mean (± SD)) | Preterm (Mean (± SD)) | p-value | partial $\eta^2$ |
|---|---|---|---|---|
| Mean claustrum volume ($mm^3$) | 330 (±50) | 360 (±55) | **<0.001** | 0.05 |
| Mean TBV-relative claustrum volume | 0.00184 (±0.00023) | 0.00195 (±0.00025) | **<0.001** | 0.04 |
| Mean claustrum MD ($10^{-3}$ $mm^2/s$) | 1.08 (±0.04) | 1.10 (±0.04) | **<0.001** | 0.04 |
| Mean claustrum FA | 0.216 (±0.027) | 0.193 (±0.027) | **<0.001** | 0.13 |

*For mean absolute and total brain volume (TBV-) relative claustrum volume, 377 term-born subjects were compared to 83 preterm-born neonates in general linear models correcting for scan age and sex. For mean claustrum mean diffusivity (MD) and fractional anisotropy (FA), 326 term-born subjects were compared to 72 preterm-born neonates in general linear models correcting for scan age and sex. Significant p-values are written in bold letters. Table reproduced with little formatting from the Online Supplement of Neubauer et al. (2023), used under CC By. SD = standard deviation.*

#### 5.2.2.2 Effect on the claustrum microstructure

To evaluate the claustrum microstructure, we chose mean diffusivity (MD) and fractional anisotropy (FA) as observable characteristics. The plots of claustrum MD and FA of the selected subjects along scan age are presented in Figure 25C and D. To test if there is an impact of preterm birth on the mean claustrum MD, we conducted a GLM approach, comparing 72 preterm- and 72 scan age-matched term-born neonates scanned in a range of GA 37.4 to 44.9 weeks. While the mean claustrum MD of right and left claustrum was the dependent variable, preterm birth was the independent categorical variable and we corrected for scan age and sex. We found a significantly higher claustrum MD in preterm-born subjects in comparison with term-equivalent term-born neonates (PT: $1.10 \pm 0.04 * 10^{-3} mm^2/s$, FT: $1.08 \pm 0.04 * 10^{-3} mm^2/s$, $p = 0.004$, partial $\eta^2 = 0.06$) with comparable results for right and left claustrum, separately ($p_{right} = 0.017$, $p_{left} = 0.002$) (Figure 26C and Table 14). Opposing the 72 preterm-born neonates to all available 326 term-born neonates, there was a significantly increased mean claustrum MD ($p < 0.001$), reproducing the results (Table 15). These findings indicate that the claustrum microstructure is impaired in preterm-born newborns around term.

To examine whether the claustrum MD change can be explained by general gray matter MD change, we expanded the GLM by GM MD, defined as the mean MD of cortical and subcortical GM, as a further independent variable. After this adjustment, there was no significant claustrum MD difference between preterm- and term-born neonates ($p = 0.255$), suggesting a general effect of preterm birth on GM MD and not a claustrum specific alteration.

As the claustrum is a narrow gray matter structure surrounded by white matter, the assessment in diffusion-weighted scans with a resolution of 1.5 mm is limited. To reduce the partial volume effect in the boundary area of the claustrum in our analyses, the GLM with 72 subjects per group was repeated with the claustrum-controlled segmentation defined as claustrum voxels which are encompassed by a minimum of 90 % other claustrum voxels (Figure 20). There was a significant increase in claustrum-controlled MD after preterm birth (PT: $1.09 \pm 0.04 * 10^{-3} mm^2/s$, FT: $1.06 \pm 0.04 * 10^{-3} mm^2/s$, $p < 0.0001$, partial $\eta^2 = 0.11$) (Figure 27). Controlling this analysis with general GM MD as a further variable of no interest, the claustrum-controlled MD was not significant anymore ($p = 0.102$), supporting the previous finding of aberrant claustrum MD in the frame of general GM MD alteration.

Regarding the second microstructural metric, we repeated the GLM approach with the claustrum FA as the dependent variable. Opposing 72 preterm- and term-born neonates, respectively, the mean claustrum FA was significantly decreased after preterm birth in comparison with term-equivalent term-born subjects (PT: 0.193 ± 0.027, FT: 0.218 ± 0.025, $p < 0.0001$, partial $\eta^2 = 0.21$), with a much stronger effect in the right claustrum ($p_{right} < 0.001$, partial $\eta^2_{right} = 0.26$, $p_{left} < 0.001$, partial $\eta^2_{left} = 0.13$) (Figure 26D and Table 14). Opposing the 72 preterm-born neonates to all available 326 term-born neonates, there was a significantly decreased mean claustrum FA ($p < 0.001$), reproducing the results (Table 15). These findings indicate an impaired claustrum microstructure probably with emphasis on the right claustrum.

To examine the FA change in relation to the whole GM FA after preterm birth, the GLM was expanded by general GM FA as an additional independent variable. The claustrum FA was still significantly decreased in preterm-born neonates in comparison with the age-equivalent, equally sized group of term-born subjects ($p = 0.007$), suggesting a specific shift of claustrum FA.

The claustrum is a relatively small region with a large surface in proportion to the diffusion-weighted image resolution and FA is a common measure for WM (Rose et al., 2008; Thompson et al., 2011; Vangberg et al., 2006). To control for neighboring gray and white matter, further analyses were conducted. In detail, the GLM with mean claustrum FA as the dependent variable, prematurity as an independent variable, and correction for sex and scan age was expanded with one of the following independent variables, respectively: first, mean FA of the insular cortex; second, lentiform nucleus FA as a combination of the putamen and globus pallidus; and third, FA of the WM claustrum frame (Figure 20) which was defined as the intersection of a boundary around the claustrum with a width of two voxels on all sides with the insular white matter. The latter was determined by the Draw-EM atlas. Regarding the first control study with the insular cortex, there remained a significant negative effect of prematurity on claustrum FA ($p < 0.0001$, partial $\eta^2 = 0.31$). The second control analysis with the lentiform nucleus also revealed a significantly lower claustrum FA after preterm birth ($p < 0.0001$, partial $\eta^2 = 0.31$). Concerning the third control assay with WM claustrum frame, there was still a significantly lower claustrum FA in preterm-born neonates ($p < 0.0001$, partial $\eta^2 = 0.21$). The results of all three control analyses indicate that the claustrum FA alteration is unaccountable by surrounding structures. Instead, there might be a specific effect of preterm birth on the claustrum microstructure.

To address the partial volume effect in the boundary area of the claustrum, the GLM approach was repeated with the claustrum-controlled segmentation. In parallel to the MD analysis, 72 preterm-born neonates were compared with an equally sized scan age-equivalent group of term-born subjects. Again, there was a significantly decreased claustrum-controlled FA after preterm birth (PT: 0.203 ± 0.033, FT: 0.230 ± 0.031, $p < 0.0001$, partial $\eta^2 = 0.17$) (Figure 27), indicating altered claustrum microstructure. With general GM FA as an additional variable of no interest, the difference was not significant anymore ($p = 0.069$). The finding suggests an alteration of claustrum microstructure partly related to general GM FA changes.

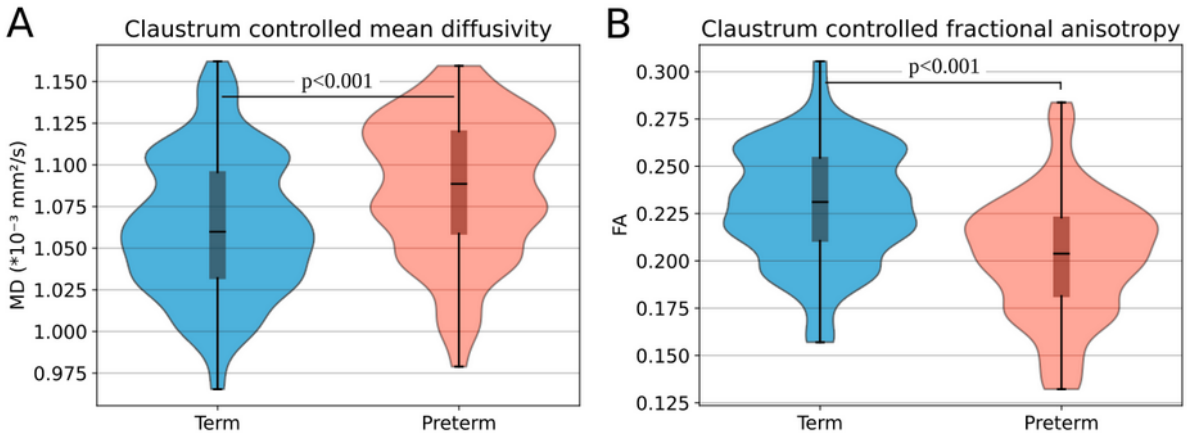


***Figure 27: Comparison of claustrum-controlled microstructure in preterm- and term-born neonates at term-equivalent age.***

*Claustrum-controlled describes claustrum voxels that are encompassed by a minimum of 90 % other claustrum voxels. (A) There was a significant increase in claustrum-controlled mean diffusivity (MD) in preterm-born neonates. (B) There was a significant decrease in claustrum-controlled fractional anisotropy (FA) after preterm birth. The groups of 72 preterm- and 72 term-born neonates were compared with a general linear model approach correcting for sex and scan age. Figure adapted from the Online Supplement of Neubauer et al. (2023), used under CC By.*

### 5.2.2.3 Affected microstructural covariance with the claustrum after preterm birth

To evaluate the impact of preterm birth on the interaction of the claustrum with other brain regions, we correlated the right and left claustrum with cortical and subcortical regions regarding absolute and TBV-relative volume, MD, and FA. The analyses were conducted in scan age-matched groups of 83 preterm- and term-born neonates, respectively, and 72 subjects in each group for MD and FA assessment, respectively (Table 10D). The correlation coefficients r were transformed to z-values by Fisher transformation. The p-values for the

group comparison of preterm- and term-born neonates were corrected for false discovery rate to control for multiple testing. An overview of the claustrum covariance with cortical and subcortical regions is given in Table 16. Detailed z-scores and p-values for all regions and metrics, respectively, are shown in the Supplement (Table B1-4).

***Table 16: Overview of the right claustrum covariance with other brain regions.***

| Group | Metric | Cortical GM | Subcortical GM | White matter |
|---|---|---|---|---|
| Preterm | Volume | 0.44 (±0.10) | 0.57 (±0.18) | 0.49 (±0.14) |
| Term | Volume | 0.43 (±0.10) | 0.59 (±0.09) | 0.43 (±0.16) |
| | Volume: no significant differences | | | |
| Preterm | Relative volume | -0.15 (±0.20) | 0.12 (±0.25) | 0.20 (±0.19) |
| Term | Relative volume | -0.17 (±0.14) | 0.24 (±0.10) | 0.09 (±0.16) |
| | Relative volume: no significant differences | | | |
| Preterm | MD | 0.08 (±0.29) | 0.70 (±0.25) | 0.68 (±0.21) |
| Term | MD | 0.40 (±0.23) | 1.03 (±0.16) | 0.99 (±0.19) |
| | **MD (significant differences)** | **11 out of 34 regions** | **5 out of 12 regions** | **7 out of 33 regions** |
| Preterm | FA | 0.61 (±0.15) | 0.72 (±0.19) | 0.89 (±0.19) |
| Term | FA | 0.17 (±0.14) | 0.44 (±0.23) | 0.74 (±0.16) |
| | **FA (significant differences)** | **25 out of 34 regions** | **4 out of 12 regions** | **3 out of 33 regions** |

*The four claustrum metrics were correlated with the corresponding metrics in cortical and subcortical gray matter (GM), excluding the claustrum itself, as well as in white matter, respectively. For absolute volume and total brain volume-relative volume, the correlation coefficients were calculated in a group of 83 preterm-born and 83 scan age-matched term-born neonates, respectively. For mean diffusivity (MD) and fractional anisotropy (FA), the group size was 72 subjects each. The Pearson's r correlation coefficients were Fisher z-transformed and corrected for false discovery rate because of multiple testing. The presented values equal the mean z-score (± standard deviation) of the tissue regions. The amount of significantly different regions is shown in the third row of each metric, e.g., regarding the MD covariance between right claustrum and cortical GM regions, there was a significant z-score decrease in preterm-born neonates in 11 out of 34 cortical regions, labeled in bold. The regions except the claustrum were defined by the Draw-EM segmentation provided by the developing Human Connectome Project and are listed in the Supplement (Table B1-4). Table adapted from Neubauer et al. (2023), used under CC By.*

There was no significant impact of preterm birth on the covariance of claustrum volume with the absolute volume of other brain regions at term-equivalent age (Figure 28 and Table B1). The volume correlations were exclusively positive. Regarding subcortical GM, preterm-born neonates showed a comparable mean z-score but a larger standard deviation of z-scores (mean z-score for covariance with the right claustrum (±standard deviation): PT: 0.57 (±0.18), FT: 0.59 (±0.09)), suggesting more heterogeneous correlation coefficients in the preterm-born

group. Regarding cortical GM, the correlations were a bit lower and relatively homogeneous for preterm- and term-born subjects (PT: 0.44 (±0.10), FT: 0.43 (±0.10)). The z-scores were comparable with the covariance between claustrum and WM volume. Expectedly, there was a high correlation with the contra-lateral claustrum volume (PT: 1.34, FT: 1.18). The results conform with a general growth trend in the neonatal brain. There is no hint of a significant impact on the claustrum-brain volume interaction after preterm birth.

There was also no significant impact of preterm birth on the covariance of TBV-relative claustrum volume with the TBV-relative volume of other brain regions at term-equivalent age (Figure 29 and Table B2). The correlations were partly negative. Regarding the claustrum covariance with subcortical GM, there was a larger standard deviation for preterm-born subjects (PT: 0.12 (±0.25), FT: 0.24 (±0.10)), suggesting more heterogeneity in subcortical regions after preterm birth. Regarding cortical GM, the mean z-scores were negative, indicating a reverse TBV-relative volume trend in comparison with the claustrum (PT: − 0.15 (±0.20), FT: − 0.17 (±0.14)). Regarding WM covariance, the correlations in preterm-born subjects were higher than in term-born subjects, however not significant (PT: 0.20 (±0.19), FT: 0.09 (±0.16)). The results suggest no or a minor effect of preterm birth on the TBV-relative volume correlations.

Concerning MD covariance, there was a significantly decreased correlation between the claustra and the following cortical and subcortical gray and white matter regions after preterm birth (Figure 30): frontal and parts of the parietal and temporal cortex, cingulate gyrus, amygdala, subthalamic and caudate nucleus and parts of the thalamus. The correlation with the right claustrum showed more significant differences after preterm birth than the left claustrum (23 vs. 11 regions) (Table B3). The MD correlation was mostly positive except for cortical GM in preterm-born neonates. Regarding the subcortical GM covariance, the correlations were high in preterm- and term-born neonates with a higher mean in the term-born group (PT: 0.70 (±0.25), FT: 1.03 (±0.16)). In contrast, the correlation between claustrum MD with MD of cortical GM is much lower and even partly negative in preterm-born neonates (PT: 0.08 (±0.29), FT: 0.40 (±0.23)). Regarding WM covariance, the z-scores were comparable with subcortical GM. There is a high correlation between claustrum and ipsilateral insular WM in preterm and term-born neonates (z-scores between 1.55 and 1.70). All MD findings together suggest an altered microstructural interaction between the claustra and spread cortical GM and some subcortical regions after preterm birth.

Regarding FA covariance, there was a significantly increased correlation between the claustra and the following cortical and subcortical gray and white matter regions after preterm birth (Figure 31): parts of the parietal, temporal, and occipital cortex, insula GM and WM, amygdala, partly subthalamic nucleus and lentiform nucleus, hippocampus, and parahippocampal GM and WM, and brainstem. The correlation with the right claustrum showed more significant differences after preterm birth than the left claustrum (33 vs. 10 regions) (Table B4). Most of the FA correlations were positive. Regarding subcortical GM covariance, the correlations were medium high with higher z-scores in preterm-born subjects (PT: 0.72 (±0.19), FT: 0.44 (±0.23)). However, the correlation with cortical GM is lower, especially in term-born neonates (PT: 0.61 (±0.15), FT: 0.17 (±0.14)). The FA claustrum covariance is the highest in WM in preterm- and term-born neonates. The majority of significant z-score differences after preterm birth belong to cortical GM. The findings suggest an impact of preterm birth on the microstructural claustrum-cortex interaction.

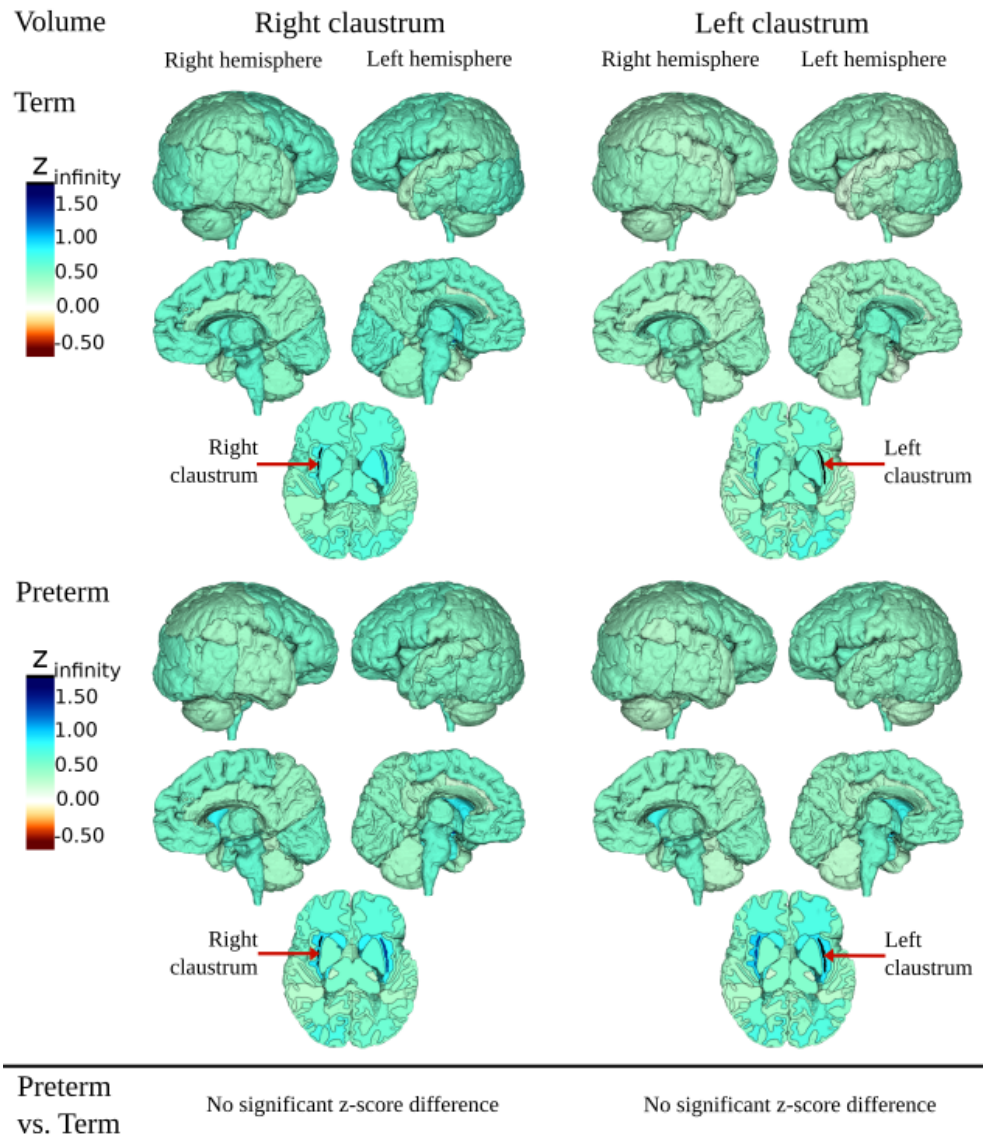


***Figure 28: Volume covariance between the right and left claustrum and other brain regions.***

*The absolute volume was correlated with other volumes in a group of 83 term-born neonates and a scan age-matched group of 83 preterm-born neonates, respectively. Pearson's r correlation coefficients were transformed to z-scores by Fisher transformation. Figure reproduced from the Online Supplement of Neubauer et al. (2023), used under CC By.*

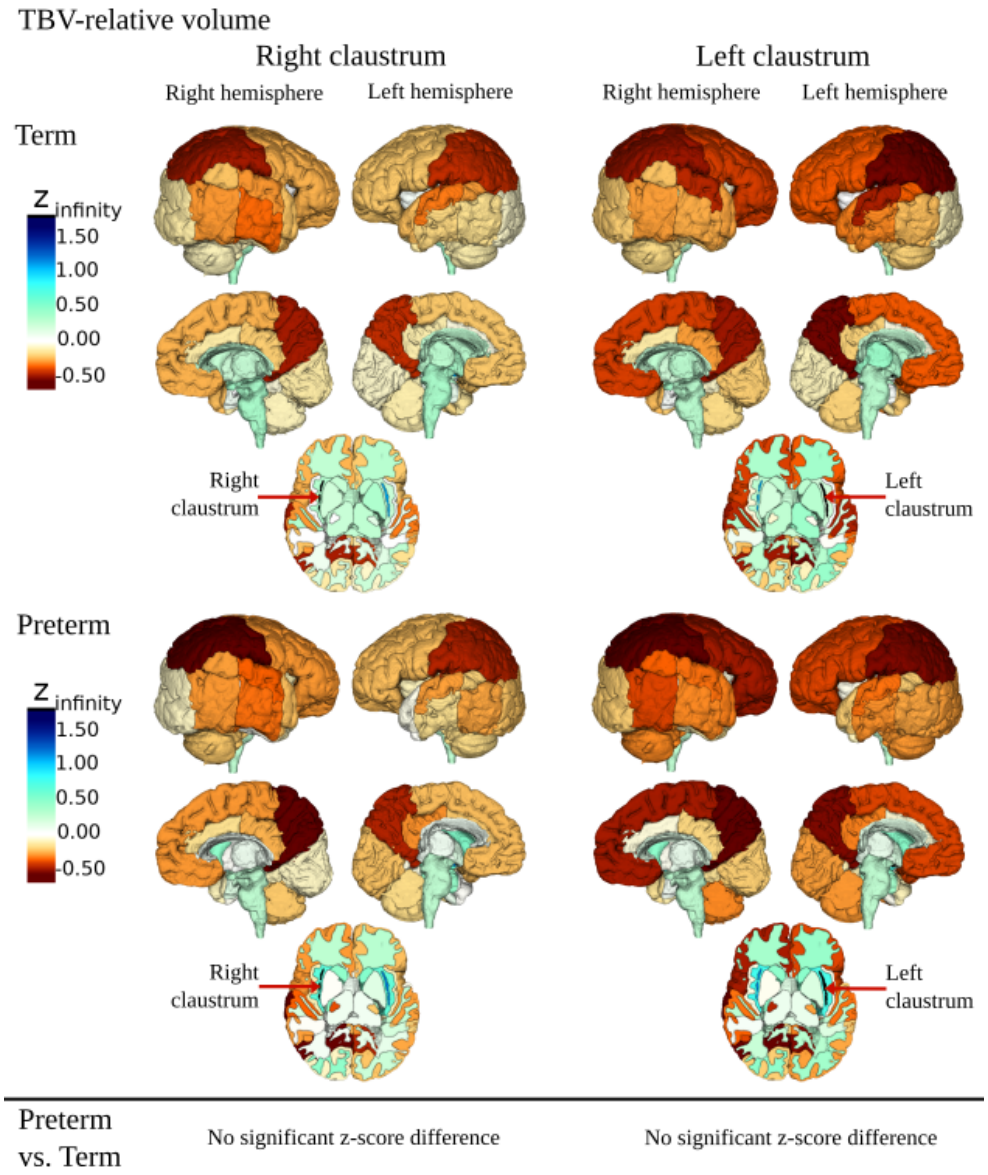


***Figure 29: Total brain volume (TBV-) relative volume covariance between the right and left claustrum and other brain regions.***

*The TBV-relative claustrum volume was correlated with TBV-relative other volumes in a group of 83 term-born neonates and a scan age-matched group of 83 preterm-born neonates, respectively. Pearson's r correlation coefficients were transformed to z-scores by Fisher transformation. Figure reproduced from the Online Supplement of Neubauer et al. (2023), used under CC By.*

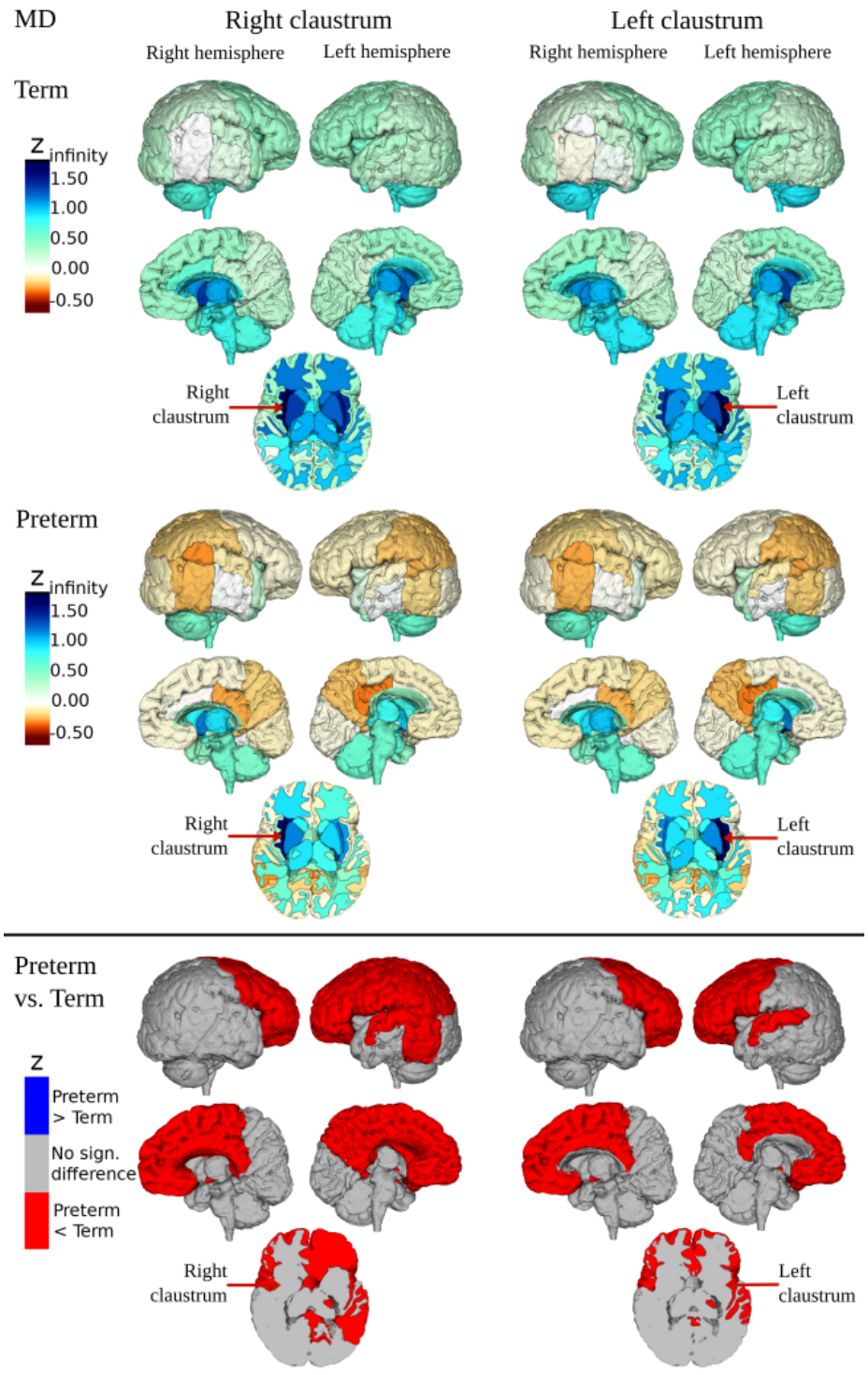


***Figure 30: Mean diffusivity (MD) covariance between the right and left claustrum and other brain regions.***

*The claustrum MD was correlated with other volumes' MD in a group of 72 term-born neonates and a scan age-matched group of 72 preterm-born neonates, respectively. Pearson's r correlation coefficients were transformed to z-scores by Fisher transformation. Regions with significantly different z-scores after preterm birth are labeled in the lower part. Figure reproduced from the Online Supplement of Neubauer et al. (2023), used under CC By.*

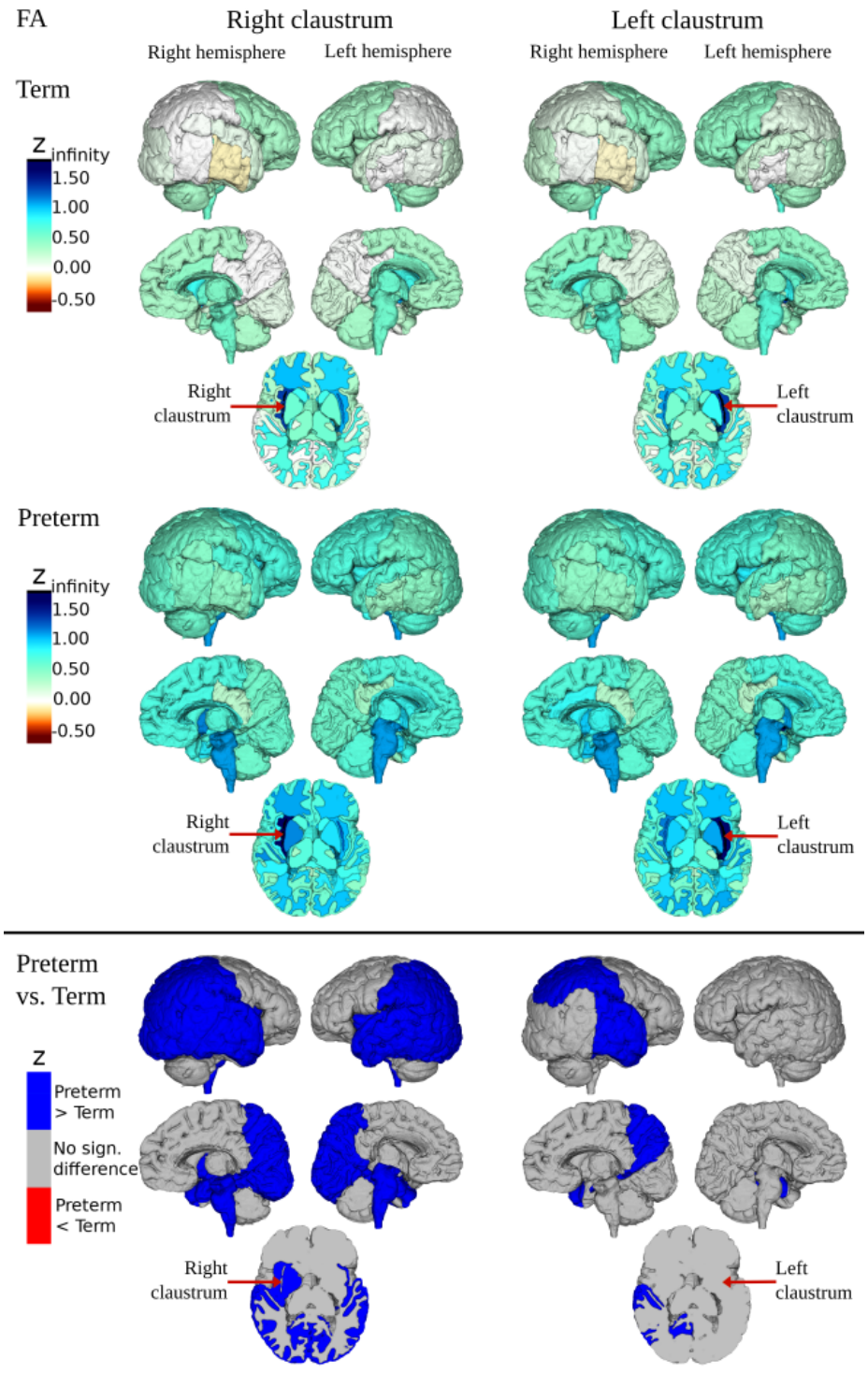


***Figure 31: Fractional anisotropy (FA) covariance between the right and left claustrum and other brain regions.***

*The claustrum FA was correlated with other volumes' FA in a group of 72 term-born neonates and a scan age-matched group of 72 preterm-born neonates, respectively. Pearson's r correlation coefficients were transformed to z-scores by Fisher transformation. Regions with significantly different z-scores after preterm birth are labeled in the lower part. Figure reproduced from the Online Supplement of Neubauer et al. (2023), used under CC By.*

## 5.3 Discussion

Comparing the claustrum in term-equivalent neonatal T2-weighted and diffusion-weighted brain MRI, we found, to the best of our knowledge for the first time, impaired claustrum macro- and microstructure in preterm-born neonates around term. The absolute and total brain volume (TBV-) relative claustrum volumes were increased after preterm birth, pointing to additional cellular or extracellular matrix. The finding is in contrast to decreased volumes of other subcortical structures. Claustrum mean diffusivity (MD) was increased and claustrum fractional anisotropy (FA) was decreased after preterm birth, indicating impaired axonal integrity and probably more extracellular water. The claustrum-related brain development, investigated with a region-based correlation analysis, was affected in several cortical regions and some subcortical areas regarding the metrics MD and FA. Combining the results, the findings suggest an impaired claustrum development in preterm-born neonates with altered coordination of the brain maturation on a cellular level. As a pathophysiological background, the two transient cell populations, subplate neurons and pre-oligodendrocytes, overlap with the claustrum development and might be causally related to the claustrum alteration after preterm birth. Clinically relevant functional deficits in attention modulation and slow-wave sleep are imaginable.

### 5.3.1 Ongoing claustrum development in neonates

Analyzing a spectrum of term-born neonates and longitudinally scanned preterm-born neonates in a range of GA 30 to 45 weeks, there was an ongoing macro- and microstructural development of the claustrum. Regarding the macrostructure, absolute claustrum volume increased around term. Compared to the mean volume of right and left claustrum of term-born adults of around 487 $mm^3$ (Hedderich et al., 2021), the neonatal claustrum is smaller with around 332 $mm^3$, suggesting that the claustrum growth continues after GA of 45 weeks. However, the TBV-relative claustrum volume decreased over time, indicating that other brain structures grow faster in this period than the claustrum. This finding is consistent with other imaging studies (Gilmore et al., 2007; Makropoulos et al., 2016), emphasizing the growth of cortical gray matter in the early postnatal period.

On a microstructural level, the claustrum mean diffusivity (MD) decreased and claustrum fractional anisotropy (FA) increased in the postnatal period in preterm- and term-born newborns. While the adult claustrum MD and FA are $769*10^{-6}$ $mm^2/s$ and 0.403, respectively

(Hedderich et al., 2021), the neonatal claustrum MD and FA were $1080*10^{-6}$mm²/s and 0.218, respectively. Thus, the developmental trend seems to proceed after the GA of 45 weeks. This development is in parallel with generally decreasing mean diffusivity (Hüppi and Dubois, 2006) and increasing FA in basal ganglia (Chau et al., 2013) as well as decreasing MD and increasing FA in the neonatal thalamus (Eaton-Rosen et al., 2015) and the putamen (Dimitrova et al., 2020).

MD decrease is associated with higher cell density, myelination, and lower extracellular water (Dimitrova et al., 2020; Hüppi and Dubois, 2006). Higher FA is related to a higher fiber density and is also influenced by myelination (Beaulieu, 2002; Eaton-Rosen et al., 2015). In sum, the findings suggest a growing amount and increasing integrity of cells and connections with progressing myelination.

### 5.3.2 Impaired claustrum macrostructure after preterm birth

Comparing preterm- and term-born T2-weighted MRI scans with a scan age-matched and sex-controlling approach, the absolute and TBV-relative claustrum volumes were increased after preterm birth. Splitting right and left claustrum, the latter showed a higher volume increase after preterm birth, suggesting an asymmetry. A side difference was also present in term-born neonates with slightly larger right claustrum volumes than left claustrum volumes. This finding is in accordance with studies in adults (Kapakin, 2011; Milardi et al., 2015; Torgerson et al., 2015) although a larger left claustrum was also described elsewhere (Berman et al., 2020). Coming back to the increased claustrum volume after preterm birth, the result is different from other subcortical gray matter structures, namely the thalamus and caudate nucleus, which showed a smaller TBV-relative volume after preterm birth in the same dataset.

In general, the increased claustrum volume is opposed to studies of other subcortical gray matter structures in newborns after preterm birth: there is evidence for smaller thalamus volume (Ball et al., 2012), thalamus and lentiform nucleus volume (Boardman et al., 2006; Srinivasan et al., 2007), and deep gray matter in general (Makropoulos et al., 2016; Padilla et al., 2015). Increased gray matter volume in preterm-born neonates is rarely reported. A larger volume in preterm-born neonates at term was found for the ventricles (Inder et al., 2005; Makropoulos et al., 2016). Also in preterm-born adolescents and adults, the cortical and subcortical gray matter volume is mainly decreased in comparison with term-born controls (Nosarti et al., 2008). However, increased volumes were observed in regions related to visual processes (Padilla et al., 2015) and in frontal, insular, and anterior parietal cortices in neonates

after preterm birth (Dimitrova et al., 2021). Moreover, an increased gray matter was found in frontal and temporal cortices including the parahippocampal and cingulate gyrus in preterm-born adolescents and adults (Meng et al., 2016; Nosarti et al., 2008). In contrast, there is no significant difference between the claustrum volume in preterm- and term-born adults (Hedderich et al., 2021). Thus, the increased claustrum volume after preterm birth might be transient.

The temporary increase of the claustrum could be explained by swollen cells or a higher amount of cell bodies, an accumulation of extracellular matrix, or a combination of both. A volume increase due to extrauterine experiences influencing the claustrum function like attention and slow-wave sleep processes might also affect regional maturation (Padilla et al., 2015). A blurred delimitation between the claustrum and surrounding white matter after preterm birth is also imaginable. A microstructural analysis was appended to approach these explanations.

### 5.3.3 Impaired claustrum microstructure after preterm birth

Comparing preterm- and term-born diffusion-weighted MRI scans with a scan age-matched and sex-controlling approach, the claustrum MD was increased and the claustrum FA was decreased after preterm birth. To address the limitation of a narrow claustrum structure in limited image resolution, the analyses were extensively controlled with surrounding white and gray matter structures and reproduced with the core part of the claustrum segmentation, called claustrum-controlled. Thereby, the signal impact of surrounding areas, e.g., corticostriatal fibers in the external capsule (Kostović et al., 2022; Schmahmann and Pandya, 2006; Vasung et al., 2010) and corticocortical connections like frontotemporal fibers in the extreme capsule (Mars et al., 2016; Mathur, 2014; Petrides and Pandya, 2007) could be reduced. The FA decrease, more prominent on the right side, was more claustrum specific than the MD change which was unspecific after control for cortical and subcortical gray matter regions.

A lower FA in preterm-born neonates in comparison with term-born controls is in line with observations of other subcortical gray matter structures like basal ganglia (Chau et al., 2013) and lentiform nucleus (Lean et al., 2019). It is also observed in WM regions (Chau et al., 2013; de Kieviet et al., 2014; Ment et al., 2009). As there was no claustrum FA difference in preterm- and term-born adults (Hedderich et al., 2021), the FA deviation might be a temporary effect.

An increased MD in gray matter in preterm-born neonates is partly consistent with other studies: While previous investigations described increased thalamus MD (Ball et al., 2012; Rose et al., 2014), Boardman et al. (2006) found comparable diffusivity in the thalamus and lentiform nucleus in neonates at term equivalent age. Another study found decreased MD of basal ganglia and thalamus in the first week after hypoxic-ischemic events (Rutherford et al., 2004). However, there was an increased MD two or three weeks later (Rutherford et al., 2004; Ward et al., 2006) which is in accordance with our observation in scans around term. The claustrum MD in preterm-born adults was also increased in comparison with term-born controls (Hedderich et al., 2021), proposing a long-lasting phenomenon.

Both measures, FA and MD, can be interpreted on a cellular level: Physically, FA represents how directed the water molecules diffuse (Beaulieu, 2002; Hüppi and Dubois, 2006; Le Bihan, 2003). It is a common evaluation metric of white matter fiber integrity as axonal and cell membranes confine the water diffusion (Hüppi and Dubois, 2006; Le Bihan, 2003). Thereby, it reflects axonal composition and myelination (Beaulieu, 2002) and neurite density dispersion and orientation in general (Zhang et al., 2012). By the same mechanism, it can also help to describe gray matter microstructure (Chau et al., 2013; Eaton-Rosen et al., 2015; Lean et al., 2019). A lower FA correlates with a lower fiber density, less organized cell processes, and less myelination (Hüppi and Dubois, 2006). Thereby, the FA measure in GM could also include intraclaustral or pervading axons and dendrites (Eaton-Rosen et al., 2015; Ward et al., 2006; Zhang et al., 2012) which are present in the claustrum (Jackson et al., 2020; Petrides and Pandya, 1988; Schmahmann and Pandya, 2006). Moreover, a metabolic change might explain the metric shift, like FA shifts due to higher iron concentration (Keller et al., 2011; Pfefferbaum et al., 2010). Regarding gray matter FA up to four days after hypoxic-ischemic events in a piglet model, there was a correlation between decreased FA and swollen astrocytes, impaired oligodendrocytes, and altered myelination (Lee et al., 2021).

A higher MD is related to broader tissue water diffusion in a defined time (Le Bihan, 2003). This can be due to fewer membranes because of fewer or smaller cells, lower connectivity, less myelin around axons, and proportionally more tissue water (Dimitrova et al., 2020; Pfefferbaum et al., 2010; Rose et al., 2008). Instead, cytotoxic edema and neuronal degeneration on the day of a hypoxic-ischemic event are related to lower MD in piglets (Lee et al., 2021, 2020). A possible explanation for later increasing diffusivity could be an extracellular edema or cellular atrophy although the brain swelling declines in the first week

after birth (Rutherford et al., 2004, 1996). Accordingly, higher MD is related to lower cellularity (Ball et al., 2012; Batalle et al., 2019; Hedderich et al., 2021).

In summary, the finding of claustrum MD increase and FA decrease in preterm-born neonates could be affected by lower cell density and less axonal integrity and myelination or more extracellular water moving apart the membranes (Hüppi and Dubois, 2006). A developmental delay could explain the microstructural shift (Dimitrova et al., 2020) but is contrary to the macrostructural finding of an increased absolute claustrum volume.

### 5.3.4 Impaired microstructural correlations with the claustrum after preterm birth

Comparing correlations between the claustrum and other brain structures in preterm- and term-born neonates, there was significantly altered microstructural covariance with the claustrum after preterm birth. In detail, the MD covariance with the claustrum was decreased in several cortical and partly subcortical regions. The FA covariance with the claustrum was increased in many cortical and some subcortical regions. The groups of the term- and preterm-born subjects were matched for scan age to gain term-equivalent conditions. P-values were corrected for false discovery rate because of multiple testing. Altered covariance was previously described for GM volumes in very preterm-born adolescents (Nosarti et al., 2011) and young adults (Scheinost et al., 2017). Possible reasons for our result with altered microstructural covariance but without altered volume covariance could be the age of the subjects or the claustrum as the only seed region. Impaired structural covariance was also shown in other conditions like dementia and schizophrenia (Alexander-Bloch et al., 2013). Our findings partly conform with the claustrum covariance networks in adults, described in Berman et al. (2020): Regarding the volume covariance, we also found a relatively higher correlation with the frontal GM, although the correlation with the temporal cortex was unsuspicious; concerning the MD covariance, we found a more symmetric correlation for right and left claustrum than described in adults. Due to slightly different methodological approaches with other parcellations, correlation coefficients, and fewer structural changes in the scan age range of young adults, the direct comparison of the results is limited. A potential impact of the scan age range in the neonatal cohort is discussed below.

There are different possible explanations of structural covariance: The related regions could be directly connected, functionally connected, accord in their genetic regulation, or overlap in their development (Alexander-Bloch et al., 2013; Berman et al., 2020). Thus, the altered

claustrum microstructural covariance in preterm-born neonates can be interpreted in different ways. The theory of developmental similarities is particularly relevant as the neonates show ongoing brain development and claustrum maturation in the observational scan age range. An altered covariance could correspond to a confounded development (Alexander-Bloch et al., 2013; Nosarti et al., 2011). How vulnerable a region reacts to adverse events like hypoxia-ischemia around preterm birth depends on the tissue properties at that time, e.g., on the genetically influenced expression of glutamate receptors (Millar et al., 2017). The impaired microstructural correlation between claustra and cortical and subcortical regions after preterm birth suggests a specific alteration of the claustrum development in interaction with other regions.

Another interpretation could be the indirect damage of the claustrum structure by aberrant connectivity (Alexander-Bloch et al., 2013). Subplate neurons influence the thalamo-cortical and cortico-cortical connectivity and are also related to claustrum development (Bruguier et al., 2020; Hoerder-Suabedissen and Molnár, 2015; Molnár et al., 2020). Pre-oligodendrocytes (pre-OLs) are essential for the physiological development of the myelinated connectome and damage also affects the connected GM regions (Back and Volpe, 2018; Kinney and Volpe, 2018; Volpe, 2019). As the claustrum is widely connected to cortical and partly subcortical regions (Milardi et al., 2015; Torgerson et al., 2015), it is putatively vulnerable to these effects and the altered covariance could indicate impaired connectivity.

It seems that the altered MD correlations always decreased and the FA correlations increased after preterm birth. We found that claustrum MD was decreasing around term. As cortical MD is also decreasing in neonates (Ball et al., 2013), an alteration of the system affects the correlation. The claustrum FA was increasing around term. The cortical FA decreases till GA 38 and remains static in large parts in the following weeks (Ball et al., 2013). When the claustrum FA increases more slowly after preterm birth, the claustrum and cortical trajectories align with each other resulting in a higher correlation.

While the affected regions of MD covariance cover the frontal cortex, the impacted regions of FA covariance concentrate on the parietal and temporal lobes. Previous studies found heterogeneity in the cortex regarding microstructural development (Dimitrova et al., 2021, 2020) and the impact of preterm birth (Bouyssi-Kobar et al., 2018; Dimitrova et al., 2020). Consistent with our variation in frontal and more occipital regions, there was a specific FA decrease in parietal and temporal cortices and an MD decrease in frontal regions in neonates

around term (Dimitrova et al., 2021). The impact of preterm birth is partly varying in different studies: An increased MD in parietal, temporal, and occipital regions, and increased FA in the insula (Dimitrova et al., 2021), or widespread increased MD and increased FA in the primary motor cortex (Bouyssi-Kobar et al., 2018). Reasons for the region-specific effect of preterm birth on the cortical microstructure could be the variety in development and function (Dimitrova et al., 2021), e.g., the synaptogenesis is more pronounced in sensory areas with stimulation by extrauterine influences (Huttenlocher and Dabholkar, 1997).

Comparing the right and left claustrum covariance analysis, there were more significant differences for the right claustrum microstructure. The finding is in accordance with a higher effect size of preterm birth on the right claustrum FA. However, the impact of preterm birth on claustrum MD is not focused on the right side. The side difference may be explained by uneven genetic factors in the brain (Sun et al., 2005). To conclude, the changed microstructural claustrum covariance suggests an altered maturation possibly affecting the claustrum connectivity. Further work is required to clarify the pathophysiological causes and consequences for side- and region-specific effects and the meaning on a network and a functional level.

### 5.3.5 Coherence of macro- and microstructural claustrum impairment

For a more detailed interpretation, we bring together the individual analyses: first, the increased claustrum volume; second, the altered claustrum microstructure; and third, the aberrant microstructural covariance with the claustrum in preterm-born neonates in comparison with scan age-equivalent term-born subjects. A couple of non-exclusive mechanisms are conceivable to unite macro- and microstructural findings. Point by point, we found an absolute claustrum volume increase. The volume extension could be explained by a higher amount of cellular or extracellular components. This tissue composition was investigated by the metrics MD and FA. A higher MD, which was observed in the claustrum, is correlated with lower cellularity (Ball et al., 2012; Batalle et al., 2019; Dimitrova et al., 2020). Thus, the volume increase might be due to an increased extracellular matrix instead of cell somata and fiber tracts. This theory is in line with the decreased claustrum FA as the additional matrix might pull the existing fiber tracts apart. When the water molecules diffuse less directed, the FA decreases (Beaulieu, 2002; Le Bihan, 2003).

The increased extracellular matrix might be due to an inflammatory reaction. An inflammatory reaction might occur in the context of neuroinflammation after preterm birth often accompanied by hypoxic-ischemic events (McClendon et al., 2017; Rose et al., 2014; Volpe, 2019). Such an inflammatory reaction in the developing brain is mediated by certain phenotypes of microglia (Reemst et al., 2016; Volpe, 2019). For instance, glial cell reaction alters the maturation of pre-oligodendrocytes (Back, 2017; Back and Volpe, 2018; Volpe, 2019). Thus, immature myelination is reduced in accordance with increased MD and decreased FA (Beaulieu, 2002; Dimitrova et al., 2020; Volpe, 2019). Furthermore, hypoxic-ischemic incidents affect subplate neurons (Kinney et al., 2012; McClendon et al., 2017; McQuillen and Ferriero, 2005) probably leading to impaired axonal integrity supporting the MD and FA change (Beaulieu, 2002; Ghosh et al., 1990). Moreover, cells in the claustrum could be directly damaged by hypoxic-ischemic events and inflammation, e.g., vulnerable subplate-derived cells (Bruguier et al., 2020; Kinney et al., 2012; McClendon et al., 2017; McQuillen and Ferriero, 2005; Volpe, 2019). Overall, it should be noted that brain damage is dynamic, particularly in the first weeks after birth (McKinstry et al., 2002; Rutherford et al., 2004). This study primarily examines the claustrum structure in the range of weeks post-delivery after the acute phase with cell edema in the first week after injury (Rutherford et al., 2004).

Though, the TBV-relative volumes of other subcortical gray matter structures like the thalamus were reduced after preterm birth. Both structures, the thalamus and claustrum, are highly connected. A crucial difference could be the close connection between the claustrum and subplate (Bruguier et al., 2020; Puelles, 2014). Additionally, the early formation of the claustrum might play a role (Bruguier et al., 2020; Watson and Puelles, 2017). However, it remains speculation if these aspects influence the vulnerability of the claustrum.

Future studies focusing on the microstructure of the claustrum and connected regions after preterm birth are needed to examine the cellular level and potential metabolic alterations in detail and to confirm or refute the theories. Histological methods and advanced imaging approaches, e.g., neurite orientation dispersion and density imaging and constrained spherical deconvolution, are conceivable to clarify further details of the physiologic and impaired claustrum microstructure (Eaton-Rosen et al., 2015; Kelly et al., 2022; Kline et al., 2022; Pecheva et al., 2018; Wang et al., 2022; Zhang et al., 2012).

### 5.3.6 Speculation about clinical effects of impaired claustrum structure in neonates

The claustrum function has not been fully clarified so far (Smith et al., 2020). Inspired by the high connectivity of this region, the claustrum is discussed to be important for attention modulation and slow-wave sleep coordination (Benarroch, 2021; Liu et al., 2019; Narikiyo et al., 2020; Smith et al., 2020). Both features are essential for mental development and performance (Ginnell et al., 2021; Perkinson-Gloor et al., 2015). However, preterm birth and correlated risk factors like bronchopulmonary dysplasia endanger normal brain development and putatively reduce the mean long-term cognitive performance of preterm-born subjects (Jaekel et al., 2019; Twilhaar et al., 2018a, 2018b; Wolke et al., 2019). Beyond that, the claustrum microstructure impairment is related to the intelligence quotient drop in very preterm-born adults (Hedderich et al., 2021). We found that altered claustrum microstructure is already apparent in preterm-born neonates and, additionally, there was an increased claustrum volume after preterm birth. This observation may support the hypothesis that early claustrum alteration forecasts the cognitive outcome. This question could be answered in the future with the cognitive data of the developing Human Connectome Project collected at 1.5 years after birth.

Concerning the assumed claustrum function in the sleeping phase (Narikiyo et al., 2020), we expect an altered slow-wave sleep after preterm birth due to altered claustrum structure. Consistent with our estimation, a previous study reported that affected neonates show delayed development of slow-wave sleep (Watanabe et al., 1974). On the other hand, the results for preterm-born children and adolescents are inconsistent as they showed prolonged slow-wave sleep (Chan et al., 2020; Wehrle et al., 2017) or reduced slow-wave sleep (Perkinson-Gloor et al., 2015) depending on the study. Other data about slow-wave sleep in preterm-born humans are scarce. Additional studies on this topic will be needed to verify the role of the claustrum in sleep alteration after preterm birth.

The reliability of claustrum macro- and microstructure as prognostic factors needs evaluation. The specificity of results and the importance of the attributed functions provide sustaining conditions.

### 5.3.7 Strengths and limitations

The neonatal claustrum was analyzed in a current, large-scale, public dataset of preterm- and term-born neonates. High-resolution scans underwent expert quality control and all claustrum

segmentations were visually checked. The comparison of preterm- and term-born neonates was studiously controlled for age equivalence and the analyses were corrected for sex and total brain volume. Background examinations of the claustrum development, covariance analyses with other brain regions, and extensive control studies were provided.

Despite the current dataset and careful evaluation, the study is limited by the following aspects: 1) The claustrum is a narrow structure with a partly blurred boundary in the MRI. Thus, the claustrum segmentation is demanding and partly subjective in the edge areas. We tried to standardize the segmentation process with automatization, which is discussed in section 4.3. 2) The limited image resolution, particularly in diffusion-weighted scans, might lead to partial volume effects confounding gray and white matter (Arrigo et al., 2017; Hedderich et al., 2021; Makropoulos et al., 2018b). For this reason, the analyses were corrected for the surrounding structures. Furthermore, a claustrum-controlled segmentation excluded the boundary region in the microstructural examination. 3) The metrics applied in this study are limited in their interpretation of the claustrum microstructure. Mean diffusivity (MD) and fractional anisotropy (FA) are physical dimensions describing water diffusion. The cellular components can only be inferred indirectly (Le Bihan, 2003). Additionally, the interpretation of FA must be viewed critically as FA in gray matter shows a higher variability when being reproduced (Vollmar et al., 2010) and the absolute values were rather low (0.10-0.28). In white matter, values < 0.2 are hardly usable (Smith et al., 2006). Advanced diffusion MRI approaches like neurite orientation dispersion and density imaging and constrained spherical deconvolution could supply further information about volume fractions and fiber orientation distributions (De Luca et al., 2020; Zhang et al., 2012). Histological studies are welcome to investigate the impact of preterm birth on cellular components. 4) We mainly applied general linear models which are unable to depict non-linear relationships. As a result, complex relationships can be overlooked. For instance, the statistical models cannot distinguish whether the gap between preterm and term-born neonates changes over the observational period. However, the simplistic linear approach avoids the overfitting of the dataset. Scatter plots give an additional visual overview of the data. 5) Previous studies showed that preterm-born neonates are a heterogeneous group with a wide outcome range (Dimitrova et al., 2020; F. Kaul et al., 2021). Thus, comparing the group means might not satisfy the complexity of brain alterations after preterm birth. In future investigations,

normative modeling can address this issue by comparing preterm-born individuals to a normative range (Marquand et al., 2019, 2016).

To conclude, comparing preterm- and term-born neonates at term-equivalent age, we found altered claustrum macro- and microstructure, and impaired microstructural covariance with the claustrum after preterm birth. The results suggest specific claustrum development alteration possibly due to the link to hypoxia-ischemia sensible subplate neurons and pre-oligodendrocytes around preterm birth.

# 6 General discussion: Claustrum structure analysis in neonatal brain MRI

Based on a large public dataset, we established automated claustrum segmentation in neonatal brain MRI by deep learning with transfer learning from adult scans (Li et al., 2021; Neubauer et al., 2022). Subsequently, these segmentations were applied to extract claustrum macro- and microstructural measures in a contemporary cohort of preterm- and term-born neonates. Claustrum macro- and microstructure were altered in preterm-born neonates compared with age-equivalent term-born subjects, suggesting an impaired claustrum development after preterm birth (Neubauer et al., 2023). There are indications that the claustrum microstructure remains impaired further into adulthood (Hedderich et al., 2021). In the following, the claustrum segmentation and analyses are discussed together. Detailed discussions of each topic separately are presented in 4.3 for claustrum segmentation and in 5.3 for claustrum structure analysis.

The optimized multi-view deep learning model achieved high accuracy in claustrum segmentation in >97 % of the subjects after transfer learning from adult scans. The performance was extensively evaluated with three scores and showed slightly inferior results than intra-rater reliability but outperformed inter-rater reliability. To ascertain a high quality in all scans, the automated segmentations were visually controlled and corrected where necessary. The model constraints in the youngest subjects were examined and led to improved age-stratified training. The model accuracy is comparable to current studies in other small regions (Billot et al., 2020; Wisse et al., 2016) and was able to exceed the adult claustrum segmentation algorithm (Li et al., 2021). The results indicate an effective and precise method for automated claustrum segmentation in neonatal MRI. The transfer learning approach can also serve as a model for similar studies in neonates as many new applications are adapted for adults first. We recommend an age-stratification of the training set in further AI application in neonatal cohorts.

Comparing the claustrum structure of preterm- and term-born neonates by applying the segmentations described above, we found altered claustrum macro- and microstructure after preterm birth. The absolute and total brain volume-relative claustrum volume were increased after preterm birth. The claustrum microstructure was altered in terms of increased mean diffusivity (MD) and decreased fractional anisotropy (FA). Additionally, the claustrum microstructural relative brain development was altered in preterm-born subjects. The

statistical models were controlled for scan age and sex. Structural and diffusion-weighted scans were further controlled for surrounding gray and white matter structures to test for specificity of the finding showing specific claustrum volume increase and FA shift. While the MD change was in line with the findings in the adult claustrum, there was no FA or volume shift in older subjects (Hedderich et al., 2021), suggesting a partly temporary impact of preterm birth on the neonatal claustrum. The claustrum volume increase after preterm birth is atypical in comparison with many other brain regions with decreased volumes (Ball et al., 2012; Makropoulos et al., 2016) but not incredible (Dimitrova et al., 2021; Padilla et al., 2015). Besides, the microstructural changes accord with earlier observations in other brain regions (Ball et al., 2012; Chau et al., 2013). To conclude, preterm birth alters the mean claustrum structure in neonates with some lasting effects into adulthood (Hedderich et al., 2021; Neubauer et al., 2023). An association with cognitive performance is suggested (Hedderich et al., 2021). The detailed clinical or functional relevance has to be elucidated in further studies.

Methodologically, this study is in parallel with the claustrum examination in very preterm-born and very-low-birth-weight adults (Hedderich et al., 2021; Li et al., 2021). The approach of automated claustrum segmentation and the observable metrics, namely absolute and relative claustrum volume, MD, and FA, are similar. However, the neonatal study dealt with a developing cohort coming along with new challenges for the deep learning algorithm (Neubauer et al., 2022). While the increased claustrum MD is consistent in preterm-born neonates and adults (Hedderich et al., 2021), the increased volume and decreased FA of the claustrum in neonates were, to the best of our knowledge, not reported before. This finding suggests both, a temporary effect and a lasting impairment of the claustrum structure after preterm birth.

Despite careful data processing and elaborate evaluation with control analyses, this study has some limitations: 1) the image resolution of structural and diffusion MRI conforms to the current technical standard (Hughes et al., 2017). However, the claustrum is a delicate structure and difficult to delimitate for humans and machines in the scans. In spite of a segmentation protocol, the manual annotation and the models trained with these templates remain subjective to some degree. Especially, diffusion metrics may be mingled with surrounding tissue due to partial volume effects. Several control analyses address this issue; 2) the interpretation of the determined metrics, claustrum volume, MD, and FA, is ambiguous. Histological examination

or advanced imaging methods are needed for clarification on a cellular level; 3) cognitive data could considerably broaden the impact of this study by combining structural and functional components. A correlation between claustrum impairment in neonates and mental performance is pending. The publication of clinical and performance data by the developing Human Connectome Project will make this possible.

# 7 Conclusion

In conclusion, the claustrum structure was analyzed in a large and current neonatal cohort.

First, automated claustrum segmentation was established in neonatal brain MRI by deep learning with transfer learning from adult scans. The algorithm was optimized for the developing subjects and achieved reliable results for the most part in the large dataset, outperforming inter-rater reliability.

Second, analyzing the claustrum structure, the claustrum volume was increased in preterm-born neonates in comparison with age-equivalent term-born neonates. The claustrum microstructure was altered in terms of higher mean diffusivity and lower fractional anisotropy after preterm birth, suggesting increased extracellular matrix or lower cellularity and cell integrity after hypoxic-ischemic events. An overlap of susceptible subplate neurons and pre-oligodendrocytes in the developing claustrum could explain specific vulnerability.

# 8 References


Aanes, S., Bjuland, K.J., Sripada, K., Sølsnes, A.E., Grunewaldt, K.H., Håberg, A., Løhaugen, G.C., Skranes, J., 2019. Reduced hippocampal subfield volumes and memory function in school-aged children born preterm with very low birthweight (VLBW). NeuroImage Clin. 23, 101857. https://doi.org/10.1016/j.nicl.2019.101857

Albishri, A.A., Shah, S.J.H., Schmiedler, A., Kang, S.S., Lee, Y., 2019. Automated Human Claustrum Segmentation using Deep Learning Technologies. ArXiv191107515 Cs Eess.

Alexander, B., Loh, W.Y., Matthews, L.G., Murray, A.L., Adamson, C., Beare, R., Chen, J., Kelly, C.E., Anderson, P.J., Doyle, L.W., Spittle, A.J., Cheong, J.L.Y., Seal, M.L., Thompson, D.K., 2019. Desikan-Killiany-Tourville Atlas Compatible Version of M-CRIB Neonatal Parcellated Whole Brain Atlas: The M-CRIB 2.0. Front. Neurosci. 13.

Alexander, B., Murray, A.L., Loh, W.Y., Matthews, L.G., Adamson, C., Beare, R., Chen, J., Kelly, C.E., Rees, S., Warfield, S.K., Anderson, P.J., Doyle, L.W., Spittle, A.J., Cheong, J.L.Y., Seal, M.L., Thompson, D.K., 2017. A new neonatal cortical and subcortical brain atlas: the Melbourne Children's Regional Infant Brain (M-CRIB) atlas. NeuroImage 147, 841–851. https://doi.org/10.1016/j.neuroimage.2016.09.068

Alexander-Bloch, A., Giedd, J.N., Bullmore, E., 2013. Imaging structural co-variance between human brain regions. Nat. Rev. Neurosci. 14, 322–336. https://doi.org/10.1038/nrn3465

Andersson, J.L., Jenkinson, M., Smith, S., 2007. Non-linear registration, aka Spatial normalisation FMRIB technical report TR07JA2. FMRIB Anal. Group Univ. Oxf. 2, e21.

Arimatsu, Y., Ishida, M., Kaneko, T., Ichinose, S., Omori, A., 2003. Organization and development of corticocortical associative neurons expressing the orphan nuclear receptor Nurr1. J. Comp. Neurol. 466, 180–196. https://doi.org/10.1002/cne.10875

Arrigo, A., Mormina, E., Calamuneri, A., Gaeta, M., Granata, F., Marino, S., Anastasi, G.P., Milardi, D., Quartarone, A., 2017. Inter-hemispheric Claustral Connections in Human Brain: A Constrained Spherical Deconvolution-Based Study. Clin. Neuroradiol. 27, 275–281. https://doi.org/10.1007/s00062-015-0492-x

Back, S.A., 2017. White matter injury in the preterm infant: pathology and mechanisms. Acta Neuropathol. (Berl.) 134, 331–349.

Back, S.A., Luo, N.L., Borenstein, N.S., Levine, J.M., Volpe, J.J., Kinney, H.C., 2001. Late Oligodendrocyte Progenitors Coincide with the Developmental Window of Vulnerability for Human Perinatal White Matter Injury. J. Neurosci. 21, 1302–1312. https://doi.org/10.1523/JNEUROSCI.21-04-01302.2001

Back, S.A., Luo, N.L., Mallinson, R.A., O'Malley, J.P., Wallen, L.D., Frei, B., Morrow, J.D., Petito, C.K., Roberts Jr., C.T., Murdoch, G.H., Montine, T.J., 2005. Selective vulnerability of preterm white matter to oxidative damage defined by F2-isoprostanes. Ann. Neurol. 58, 108–120. https://doi.org/10.1002/ana.20530

Back, S.A., Volpe, J.J., 2018. Chapter 15 - Encephalopathy of Prematurity: Pathophysiology, in: Volpe, J.J., Inder, T.E., Darras, B.T., de Vries, L.S., du Plessis, A.J., Neil, J.J., Perlman, J.M. (Eds.), Volpe's Neurology of the Newborn (Sixth Edition). Elsevier, pp. 405-424.e8. https://doi.org/10.1016/B978-0-323-42876-7.00015-6

Backhausen, L.L., Herting, M.M., Tamnes, C.K., Vetter, N.C., 2021. Best Practices in Structural Neuroimaging of Neurodevelopmental Disorders. Neuropsychol. Rev. https://doi.org/10.1007/s11065-021-09496-2

Baizer, J.S., 2001. Serotonergic innervation of the primate claustrum. Brain Res. Bull. 55, 431–434. https://doi.org/10.1016/S0361-9230(01)00535-4

Ball, G., Boardman, J.P., Rueckert, D., Aljabar, P., Arichi, T., Merchant, N., Gousias, I.S., Edwards, A.D., Counsell, S.J., 2012. The effect of preterm birth on thalamic and cortical development. Cereb. Cortex N. Y. N 1991 22, 1016–1024. https://doi.org/10.1093/cercor/bhr176

Ball, G., Srinivasan, L., Aljabar, P., Counsell, S.J., Durighel, G., Hajnal, J.V., Rutherford, M.A., Edwards, A.D., 2013. Development of cortical microstructure in the preterm human brain. Proc. Natl. Acad. Sci. 110, 9541–9546. https://doi.org/10.1073/pnas.1301652110

Barrett, F.S., Krimmel, S.R., Griffiths, R.R., Seminowicz, D.A., Mathur, B.N., 2020. Psilocybin acutely alters the functional connectivity of the claustrum with brain networks that support perception, memory, and attention. NeuroImage 218, 116980. https://doi.org/10.1016/j.neuroimage.2020.116980

Basser, P.J., Mattiello, J., LeBihan, D., 1994. MR diffusion tensor spectroscopy and imaging. Biophys. J. 66, 259–267. https://doi.org/10.1016/S0006-3495(94)80775-1

Basser, P.J., Pierpaoli, C., 1996. Microstructural and Physiological Features of Tissues Elucidated by Quantitative-Diffusion-Tensor MRI. J. Magn. Reson. B 111, 209–219. https://doi.org/10.1006/jmrb.1996.0086

Bastiani, M., Andersson, J.L.R., Cordero-Grande, L., Murgasova, M., Hutter, J., Price, A.N., Makropoulos, A., Fitzgibbon, S.P., Hughes, E., Rueckert, D., Victor, S., Rutherford, M., Edwards, A.D., Smith, S.M., Tournier, J.-D., Hajnal, J.V., Jbabdi, S., Sotiropoulos, S.N., 2019a. Automated processing pipeline for neonatal diffusion MRI in the developing Human Connectome Project. NeuroImage 185, 750–763. https://doi.org/10.1016/j.neuroimage.2018.05.064

Bastiani, M., Cottaar, M., Fitzgibbon, S.P., Suri, S., Alfaro-Almagro, F., Sotiropoulos, S.N., Jbabdi, S., Andersson, J.L.R., 2019b. Automated quality control for within and between studies diffusion MRI data using a non-parametric framework for movement and distortion correction. NeuroImage 184, 801–812. https://doi.org/10.1016/j.neuroimage.2018.09.073

Batalle, D., O'Muircheartaigh, J., Makropoulos, A., Kelly, C.J., Dimitrova, R., Hughes, E.J., Hajnal, J.V., Zhang, H., Alexander, D.C., Edwards, A.D., Counsell, S.J., 2019. Different patterns of cortical maturation before and after 38 weeks gestational age demonstrated by diffusion MRI in vivo. NeuroImage 185, 764–775. https://doi.org/10.1016/j.neuroimage.2018.05.046

Bäuml, J.G., Daamen, M., Meng, C., Neitzel, J., Scheef, L., Jaekel, J., Busch, B., Baumann, N., Bartmann, P., Wolke, D., Boecker, H., Wohlschläger, A.M., Sorg, C., 2015. Correspondence Between Aberrant Intrinsic Network Connectivity and Gray-Matter Volume in the Ventral Brain of Preterm Born Adults. Cereb. Cortex 25, 4135–4145. https://doi.org/10.1093/cercor/bhu133

Beaulieu, C., 2002. The basis of anisotropic water diffusion in the nervous system – a technical review. NMR Biomed. 15, 435–455. https://doi.org/10.1002/nbm.782

Benarroch, E.E., 2021. What is the Role of the Claustrum in Cortical Function and Neurologic Disease? Neurology 96, 110–113. https://doi.org/10.1212/WNL.0000000000011280

Berman, S., Schurr, R., Atlan, G., Citri, A., Mezer, A.A., 2020. Automatic Segmentation of the Dorsal Claustrum in Humans Using in vivo High-Resolution MRI. Cereb. Cortex Commun. 1. https://doi.org/10.1093/texcom/tgaa062

Bernstein, H.-G., Ortmann, A., Dobrowolny, H., Steiner, J., Brisch, R., Gos, T., Bogerts, B., 2016. Bilaterally reduced claustral volumes in schizophrenia and major depressive disorder: a morphometric postmortem study. Eur. Arch. Psychiatry Clin. Neurosci. 266, 25–33. https://doi.org/10.1007/s00406-015-0597-x

Bethlehem, R. a. I., Seidlitz, J., White, S.R., Vogel, J.W., Anderson, K.M., Adamson, C., Adler, S., Alexopoulos, G.S., Anagnostou, E., Areces-Gonzalez, A., Astle, D.E., Auyeung, B., Ayub, M., Bae, J., Ball, G., Baron-Cohen, S., Beare, R., Bedford, S.A., Benegal, V., Beyer, F., Blangero, J., Blesa Cábez, M., Boardman, J.P., Borzage, M., Bosch-Bayard, J.F., Bourke, N., Calhoun, V.D., Chakravarty, M.M., Chen, C., Chertavian, C., Chetelat, G., Chong, Y.S., Cole, J.H., Corvin, A., Costantino, M., Courchesne, E., Crivello, F., Cropley, V.L., Crosbie, J., Crossley, N., Delarue, M., Delorme, R., Desrivieres, S., Devenyi, G.A., Di Biase, M.A., Dolan, R., Donald, K.A., Donohoe, G., Dunlop, K., Edwards, A.D., Elison, J.T., Ellis, C.T., Elman, J.A., Eyler, L., Fair, D.A., Feczko, E., Fletcher, P.C., Fonagy, P., Franz, C.E., Galan-Garcia, L., Gholipour, A., Giedd, J., Gilmore, J.H., Glahn, D.C., Goodyer, I.M., Grant, P.E., Groenewold, N.A., Gunning, F.M., Gur, R.E., Gur, R.C., Hammill, C.F., Hansson, O., Hedden, T., Heinz, A., Henson, R.N., Heuer, K., Hoare, J., Holla, B., Holmes, A.J., Holt, R., Huang, H., Im, K., Ipser, J., Jack, C.R., Jackowski, A.P., Jia, T., Johnson, K.A., Jones, P.B., Jones, D.T., Kahn, R.S., Karlsson, H., Karlsson, L., Kawashima, R., Kelley, E.A., Kern, S., Kim, K.W., Kitzbichler, M.G., Kremen, W.S., Lalonde, F., Landeau, B., Lee, S., Lerch, J., Lewis, J.D., Li, J., Liao, W., Liston, C., Lombardo, M.V., Lv, J., Lynch, C., Mallard, T.T., Marcelis, M., Markello, R.D., Mathias, S.R., Mazoyer, B., McGuire, P., Meaney, M.J., Mechelli, A., Medic, N., Misic, B., Morgan, S.E., Mothersill, D., Nigg, J., Ong, M.Q.W., Ortinau, C., Ossenkoppele, R., Ouyang, M., Palaniyappan, L., Paly, L., Pan, P.M., Pantelis, C., Park, M.M., Paus, T., Pausova, Z., Paz-Linares, D., Pichet Binette, A., Pierce, K., Qian, X., Qiu, J., Qiu, A., Raznahan, A., Rittman, T., Rodrigue, A., Rollins, C.K., Romero-Garcia, R., Ronan, L., Rosenberg, M.D., Rowitch, D.H., Salum, G.A., Satterthwaite, T.D., Schaare, H.L., Schachar, R.J., Schultz, A.P., Schumann, G., Schöll, M., Sharp, D., Shinohara, R.T., Skoog, I., Smyser, C.D., Sperling, R.A., Stein, D.J., Stolicyn, A., Suckling, J., Sullivan, G., Taki, Y., Thyreau, B., Toro, R., Traut, N., Tsvetanov, K.A., Turk-Browne, N.B., Tuulari, J.J., Tzourio, C., Vachon-Presseau, É., Valdes-Sosa, M.J., Valdes-Sosa, P.A., Valk, S.L., van Amelsvoort, T., Vandekar, S.N., Vasung, L., Victoria, L.W., Villeneuve, S., Villringer, A., Vértes, P.E., Wagstyl, K., Wang, Y.S., Warfield, S.K., Warrier, V., Westman, E., Westwater, M.L., Whalley, H.C., Witte, A.V., Yang, N., Yeo, B., Yun, H., Zalesky, A., Zar,

H.J., Zettergren, A., Zhou, J.H., Ziauddeen, H., Zugman, A., Zuo, X.N., Bullmore, E.T., Alexander-Bloch, A.F., 2022. Brain charts for the human lifespan. Nature 604, 525–533. https://doi.org/10.1038/s41586-022-04554-y

Billot, B., Bocchetta, M., Todd, E., Dalca, A.V., Rohrer, J.D., Iglesias, J.E., 2020. Automated segmentation of the hypothalamus and associated subunits in brain MRI. NeuroImage 223, 117287. https://doi.org/10.1016/j.neuroimage.2020.117287

Binks, D., Watson, C., Puelles, L., 2019. A Re-evaluation of the Anatomy of the Claustrum in Rodents and Primates—Analyzing the Effect of Pallial Expansion. Front. Neuroanat. 13. https://doi.org/10.3389/fnana.2019.00034

Blencowe, H., Cousens, S., Chou, D., Oestergaard, M., Say, L., Moller, A.-B., Kinney, M., Lawn, J., Born Too Soon Preterm Birth Action Group, 2013. Born too soon: the global epidemiology of 15 million preterm births. Reprod. Health 10 Suppl 1, S2. https://doi.org/10.1186/1742-4755-10-S1-S2

Blencowe, H., Cousens, S., Oestergaard, M.Z., Chou, D., Moller, A.-B., Narwal, R., Adler, A., Vera Garcia, C., Rohde, S., Say, L., Lawn, J.E., 2012. National, regional, and worldwide estimates of preterm birth rates in the year 2010 with time trends since 1990 for selected countries: a systematic analysis and implications. Lancet Lond. Engl. 379, 2162–2172. https://doi.org/10.1016/S0140-6736(12)60820-4

Bluemke, D.A., Moy, L., Bredella, M.A., Ertl-Wagner, B.B., Fowler, K.J., Goh, V.J., Halpern, E.F., Hess, C.P., Schiebler, M.L., Weiss, C.R., 2020. Assessing Radiology Research on Artificial Intelligence: A Brief Guide for Authors, Reviewers, and Readers—From the Radiology Editorial Board. Radiology 294, 487–489. https://doi.org/10.1148/radiol.2019192515

Boardman, J.P., Counsell, S.J., Rueckert, D., Kapellou, O., Bhatia, K.K., Aljabar, P., Hajnal, J., Allsop, J.M., Rutherford, M.A., Edwards, A.D., 2006. Abnormal deep grey matter development following preterm birth detected using deformation-based morphometry. NeuroImage 32, 70–78. https://doi.org/10.1016/j.neuroimage.2006.03.029

Bouyssi-Kobar, M., Brossard-Racine, M., Jacobs, M., Murnick, J., Chang, T., Limperopoulos, C., 2018. Regional microstructural organization of the cerebral cortex is affected by preterm birth. NeuroImage Clin. 18, 871–880. https://doi.org/10.1016/j.nicl.2018.03.020

Bruguier, H., Suarez, R., Manger, P., Hoerder-Suabedissen, A., Shelton, A.M., Oliver, D.K., Packer, A.M., Ferran, J.L., García-Moreno, F., Puelles, L., others, 2020. In search of common developmental and evolutionary origin of the claustrum and subplate. J. Comp. Neurol.

Buser, J.R., Maire, J., Riddle, A., Gong, X., Nguyen, T., Nelson, K., Luo, N.L., Ren, J., Struve, J., Sherman, L.S., Miller, S.P., Chau, V., Hendson, G., Ballabh, P., Grafe, M.R., Back, S.A., 2012. Arrested preoligodendrocyte maturation contributes to myelination failure in premature infants. Ann. Neurol. 71, 93–109. https://doi.org/10.1002/ana.22627

Campanella, G., Hanna, M.G., Geneslaw, L., Miraflor, A., Werneck Krauss Silva, V., Busam, K.J., Brogi, E., Reuter, V.E., Klimstra, D.S., Fuchs, T.J., 2019. Clinical-grade computational pathology using weakly supervised deep learning on whole slide images. Nat. Med. 25, 1301–1309. https://doi.org/10.1038/s41591-019-0508-1

Chan, M., Wong, T.C.H., Weichard, A., Nixon, G.M., Walter, L.M., Horne, R.S.C., 2020. Sleep macro-architecture and micro-architecture in children born preterm with sleep disordered breathing. Pediatr. Res. 87, 703–710. https://doi.org/10.1038/s41390-019-0453-1

Chau, V., Synnes, A., Grunau, R.E., Poskitt, K.J., Brant, R., Miller, S.P., 2013. Abnormal brain maturation in preterm neonates associated with adverse developmental outcomes. Neurology 81, 2082–2089. https://doi.org/10.1212/01.wnl.0000437298.43688.b9

Chawanpaiboon, S., Vogel, J.P., Moller, A.-B., Lumbiganon, P., Petzold, M., Hogan, D., Landoulsi, S., Jampathong, N., Kongwattanakul, K., Laopaiboon, M., Lewis, C., Rattanakanokchai, S., Teng, D.N., Thinkhamrop, J., Watananirun, K., Zhang, J., Zhou, W., Gülmezoglu, A.M., 2019. Global, regional, and national estimates of levels of preterm birth in 2014: a systematic review and modelling analysis. Lancet Glob. Health 7, e37–e46. https://doi.org/10.1016/S2214-109X(18)30451-0

Chlap, P., Min, H., Vandenberg, N., Dowling, J., Holloway, L., Haworth, A., 2021. A review of medical image data augmentation techniques for deep learning applications. J. Med. Imaging Radiat. Oncol. 65, 545–563. https://doi.org/10.1111/1754-9485.13261

Choi, H.A., Badjatia, N., Mayer, S.A., 2012. Hypothermia for acute brain injury—mechanisms and practical aspects. Nat. Rev. Neurol. 8, 214–222. https://doi.org/10.1038/nrneurol.2012.21

Cordero-Grande, L., Hughes, E.J., Hutter, J., Price, A.N., Hajnal, J.V., 2018. Three-dimensional motion corrected sensitivity encoding reconstruction for multi-shot multi-slice MRI: Application to neonatal brain

imaging. Magn. Reson. Med. 79, 1365–1376. https://doi.org/10.1002/mrm.26796
Courchesne, E., Chisum, H.J., Townsend, J., Cowles, A., Covington, J., Egaas, B., Harwood, M., Hinds, S., Press, G.A., 2000. Normal Brain Development and Aging: Quantitative Analysis at in Vivo MR Imaging in Healthy Volunteers. Radiology 216, 672–682. https://doi.org/10.1148/radiology.216.3.r00au37672
Crick, F.C., Koch, C., 2005. What is the function of the claustrum? Philos. Trans. R. Soc. B Biol. Sci. 360, 1271–1279.
Davis, W.B., 2008. The claustrum in autism and typically developing male children: a quantitative MRI study (PhD Thesis). Brigham Young University.
de Kieviet, J.F., Pouwels, P.J.W., Lafeber, H.N., Vermeulen, R.J., van Elburg, R.M., Oosterlaan, J., 2014. A crucial role of altered fractional anisotropy in motor problems of very preterm children. Eur. J. Paediatr. Neurol. 18, 126–133. https://doi.org/10.1016/j.ejpn.2013.09.004
de Kieviet, J.F., Zoetebier, L., Elburg, R.M. van, Vermeulen, R.J., Oosterlaan, J., 2012. Brain development of very preterm and very low-birthweight children in childhood and adolescence: a meta-analysis. Dev. Med. Child Neurol. 54, 313–323. https://doi.org/10.1111/j.1469-8749.2011.04216.x
De Luca, A., Guo, F., Froeling, M., Leemans, A., 2020. Spherical deconvolution with tissue-specific response functions and multi-shell diffusion MRI to estimate multiple fiber orientation distributions (mFODs). NeuroImage 222, 117206. https://doi.org/10.1016/j.neuroimage.2020.117206
Dice, L.R., 1945. Measures of the Amount of Ecologic Association Between Species. Ecology 26, 297–302. https://doi.org/10.2307/1932409
Dimitrova, R., Pietsch, M., Christiaens, D., Ciarrusta, J., Wolfers, T., Batalle, D., Hughes, E., Hutter, J., Cordero-Grande, L., Price, A.N., Chew, A., Falconer, S., Vecchiato, K., Steinweg, J.K., Carney, O., Rutherford, M.A., Tournier, J.-D., Counsell, S.J., Marquand, A.F., Rueckert, D., Hajnal, J.V., McAlonan, G., Edwards, A.D., O'Muircheartaigh, J., 2020. Heterogeneity in Brain Microstructural Development Following Preterm Birth. Cereb. Cortex 30, 4800–4810. https://doi.org/10.1093/cercor/bhaa069
Dimitrova, R., Pietsch, M., Ciarrusta, J., Fitzgibbon, S.P., Williams, L.Z.J., Christiaens, D., Cordero-Grande, L., Batalle, D., Makropoulos, A., Schuh, A., Price, A.N., Hutter, J., Teixeira, R.P., Hughes, E., Chew, A., Falconer, S., Carney, O., Egloff, A., Tournier, J.-D., McAlonan, G., Rutherford, M.A., Counsell, S.J., Robinson, E.C., Hajnal, J.V., Rueckert, D., Edwards, A.D., O'Muircheartaigh, J., 2021. Preterm birth alters the development of cortical microstructure and morphology at term-equivalent age. NeuroImage 243, 118488. https://doi.org/10.1016/j.neuroimage.2021.118488
Doria, V., Beckmann, C.F., Arichi, T., Merchant, N., Groppo, M., Turkheimer, F.E., Counsell, S.J., Murgasova, M., Aljabar, P., Nunes, R.G., Larkman, D.J., Rees, G., Edwards, A.D., 2010. Emergence of resting state networks in the preterm human brain. Proc. Natl. Acad. Sci. 107, 20015–20020. https://doi.org/10.1073/pnas.1007921107
Drozdzal, M., Vorontsov, E., Chartrand, G., Kadoury, S., Pal, C., 2016. The Importance of Skip Connections in Biomedical Image Segmentation, in: Carneiro, G., Mateus, D., Peter, L., Bradley, A., Tavares, J.M.R.S., Belagiannis, V., Papa, J.P., Nascimento, J.C., Loog, M., Lu, Z., Cardoso, J.S., Cornebise, J. (Eds.), Deep Learning and Data Labeling for Medical Applications, Lecture Notes in Computer Science. Springer International Publishing, Cham, pp. 179–187. https://doi.org/10.1007/978-3-319-46976-8_19
Eaton-Rosen, Z., Melbourne, A., Orasanu, E., Cardoso, M.J., Modat, M., Bainbridge, A., Kendall, G.S., Robertson, N.J., Marlow, N., Ourselin, S., 2015. Longitudinal measurement of the developing grey matter in preterm subjects using multi-modal MRI. NeuroImage 111, 580–589. https://doi.org/10.1016/j.neuroimage.2015.02.010
England, J.R., Cheng, P.M., 2019. Artificial Intelligence for Medical Image Analysis: A Guide for Authors and Reviewers. Am. J. Roentgenol. 212, 513–519. https://doi.org/10.2214/AJR.18.20490
Euser, A.M., Wit, C.C. de, Finken, M.J.J., Rijken, M., Wit, J.M., 2008. Growth of Preterm Born Children. Horm. Res. Paediatr. 70, 319–328. https://doi.org/10.1159/000161862
F. Kaul, Y., Johansson, M., Månsson, J., Stjernqvist, K., Farooqi, A., Serenius, F., B. Thorell, L., 2021. Cognitive profiles of extremely preterm children: Full-Scale IQ hides strengths and weaknesses. Acta Paediatr. 110, 1817–1826. https://doi.org/10.1111/apa.15776
Gabr, R.E., Coronado, I., Robinson, M., Sujit, S.J., Datta, S., Sun, X., Allen, W.J., Lublin, F.D., Wolinsky, J.S., Narayana, P.A., 2020. Brain and lesion segmentation in multiple sclerosis using fully convolutional neural networks: A large-scale study. Mult. Scler. Houndmills Basingstoke Engl. 26, 1217–1226. https://doi.org/10.1177/1352458519856843

Ghafoorian, M., Mehrtash, A., Kapur, T., Karssemeijer, N., Marchiori, E., Pesteie, M., Guttmann, C.R.G., de Leeuw, F.-E., Tempany, C.M., van Ginneken, B., Fedorov, A., Abolmaesumi, P., Platel, B., Wells, W.M., 2017. Transfer Learning for Domain Adaptation in MRI: Application in Brain Lesion Segmentation, in: Descoteaux, M., Maier-Hein, L., Franz, A., Jannin, P., Collins, D.L., Duchesne, S. (Eds.), Medical Image Computing and Computer Assisted Intervention − MICCAI 2017, Lecture Notes in Computer Science. Springer International Publishing, Cham, pp. 516–524. https://doi.org/10.1007/978-3-319-66179-7_59

Ghosh, A., Antonini, A., McConnell, S.K., Shatz, C.J., 1990. Requirement for subplate neurons in the formation of thalamocortical connections. Nature 347, 179–181. https://doi.org/10.1038/347179a0

Gilmore, J.H., Lin, W., Prastawa, M.W., Looney, C.B., Vetsa, Y.S.K., Knickmeyer, R.C., Evans, D.D., Smith, J.K., Hamer, R.M., Lieberman, J.A., Gerig, G., 2007. Regional Gray Matter Growth, Sexual Dimorphism, and Cerebral Asymmetry in the Neonatal Brain. J. Neurosci. 27, 1255–1260. https://doi.org/10.1523/JNEUROSCI.3339-06.2007

Ginnell, L., Boardman, J.P., Reynolds, R.M., Fletcher-Watson, S., 2021. Attention profiles following preterm birth: A review of methods and findings from infancy to adulthood. Infant Child Dev. 30, e2255. https://doi.org/10.1002/icd.2255

Glass, H.C., Costarino, A.T., Stayer, S.A., Brett, C.M., Cladis, F., Davis, P.J., 2015. Outcomes for extremely premature infants. Anesth. Analg. 120, 1337–1351. https://doi.org/10.1213/ANE.0000000000000705

Goldenberg, R.L., Culhane, J.F., Iams, J.D., Romero, R., 2008. Epidemiology and causes of preterm birth. The Lancet 371, 75–84. https://doi.org/10.1016/S0140-6736(08)60074-4

Goll, Y., Atlan, G., Citri, A., 2015. Attention: the claustrum. Trends Neurosci. 38, 486–495.

Gousias, I.S., Edwards, A.D., Rutherford, M.A., Counsell, S.J., Hajnal, J.V., Rueckert, D., Hammers, A., 2012. Magnetic resonance imaging of the newborn brain: manual segmentation of labelled atlases in term-born and preterm infants. NeuroImage 62, 1499–1509. https://doi.org/10.1016/j.neuroimage.2012.05.083

Greve, D.N., Fischl, B., 2009. Accurate and robust brain image alignment using boundary-based registration. NeuroImage 48, 63–72. https://doi.org/10.1016/j.neuroimage.2009.06.060

Grothe, M.J., Scheef, L., Bäuml, J., Meng, C., Daamen, M., Baumann, N., Zimmer, C., Teipel, S., Bartmann, P., Boecker, H., Wolke, D., Wohlschläger, A., Sorg, C., 2017. Reduced Cholinergic Basal Forebrain Integrity Links Neonatal Complications and Adult Cognitive Deficits After Premature Birth. Biol. Psychiatry, Neurodevelopmental Alterations: Mechanisms and Consequences 82, 119–126. https://doi.org/10.1016/j.biopsych.2016.12.008

Hastie, T., Tibshirani, R., Friedman, J., 2009. The Elements of Statistical Learning: Data Mining, Inference, and Prediction, Second Edition. Springer Science & Business Media.

Hedderich, D.M., Bäuml, J.G., Berndt, M.T., Menegaux, A., Scheef, L., Daamen, M., Zimmer, C., Bartmann, P., Boecker, H., Wolke, D., Gaser, C., Sorg, C., 2019. Aberrant gyrification contributes to the link between gestational age and adult IQ after premature birth. Brain 142, 1255–1269. https://doi.org/10.1093/brain/awz071

Hedderich, D.M., Bäuml, J.G., Menegaux, A., Avram, M., Daamen, M., Zimmer, C., Bartmann, P., Scheef, L., Boecker, H., Wolke, D., Gaser, C., Sorg, C., 2020. An analysis of MRI derived cortical complexity in premature-born adults: Regional patterns, risk factors, and potential significance. NeuroImage 208, 116438. https://doi.org/10.1016/j.neuroimage.2019.116438

Hedderich, D.M., Menegaux, A., Li, H., Schmitz-Koep, B., Stämpfli, P., Bäuml, J.G., Berndt, M.T., Bäuerlein, F.J.B., Grothe, M.J., Dyrba, M., Avram, M., Boecker, H., Daamen, M., Zimmer, C., Bartmann, P., Wolke, D., Sorg, C., 2021. Aberrant Claustrum Microstructure in Humans after Premature Birth. Cereb. Cortex. https://doi.org/10.1093/cercor/bhab178

Hoerder-Suabedissen, A., Molnár, Z., 2015. Development, evolution and pathology of neocortical subplate neurons. Nat. Rev. Neurosci. 16, 133–146.

Hughes, E.J., Winchman, T., Padormo, F., Teixeira, R., Wurie, J., Sharma, M., Fox, M., Hutter, J., Cordero-Grande, L., Price, A.N., Allsop, J., Bueno-Conde, J., Tusor, N., Arichi, T., Edwards, A.D., Rutherford, M.A., Counsell, S.J., Hajnal, J.V., 2017. A dedicated neonatal brain imaging system. Magn. Reson. Med. 78, 794–804. https://doi.org/10.1002/mrm.26462

Hüppi, P.S., Dubois, J., 2006. Diffusion tensor imaging of brain development. Semin. Fetal. Neonatal Med., Assessing Brain Function in the Perinatal Period 11, 489–497. https://doi.org/10.1016/j.siny.2006.07.006

Huttenlocher, P.R., Dabholkar, A.S., 1997. Regional differences in synaptogenesis in human cerebral cortex. J. Comp. Neurol. 387, 167–178. https://doi.org/10.1002/(SICI)1096-9861(19971020)387:2<167::AID-CNE1>3.0.CO;2-Z

Hutter, J., Tournier, J.D., Price, A.N., Cordero-Grande, L., Hughes, E.J., Malik, S., Steinweg, J., Bastiani, M., Sotiropoulos, S.N., Jbabdi, S., Andersson, J., Edwards, A.D., Hajnal, J.V., 2018. Time-efficient and flexible design of optimized multishell HARDI diffusion. Magn. Reson. Med. 79, 1276–1292. https://doi.org/10.1002/mrm.26765

Iglovikov, V.I., Rakhlin, A., Kalinin, A.A., Shvets, A.A., 2018. Paediatric Bone Age Assessment Using Deep Convolutional Neural Networks, in: Stoyanov, D., Taylor, Z., Carneiro, G., Syeda-Mahmood, T., Martel, A., Maier-Hein, L., Tavares, J.M.R.S., Bradley, A., Papa, J.P., Belagiannis, V., Nascimento, J.C., Lu, Z., Conjeti, S., Moradi, M., Greenspan, H., Madabhushi, A. (Eds.), Deep Learning in Medical Image Analysis and Multimodal Learning for Clinical Decision Support, Lecture Notes in Computer Science. Springer International Publishing, Cham, pp. 300–308. https://doi.org/10.1007/978-3-030-00889-5_34

Inder, T.E., Huppi, P.S., Warfield, S., Kikinis, R., Zientara, G.P., Barnes, P.D., Jolesz, F., Volpe, J.J., 1999. Periventricular white matter injury in the premature infant is followed by reduced cerebral cortical gray matter volume at term. Ann. Neurol. 46, 755–760. https://doi.org/10.1002/1531-8249(199911)46:5<755::aid-ana11>3.0.co;2-0

Inder, T.E., Warfield, S.K., Wang, H., Hüppi, P.S., Volpe, J.J., 2005. Abnormal cerebral structure is present at term in premature infants. Pediatrics 115, 286–294. https://doi.org/10.1542/peds.2004-0326

Jackson, J., Smith, J.B., Lee, A.K., 2020. The Anatomy and Physiology of Claustrum-Cortex Interactions. Annu. Rev. Neurosci. 43, 231–247. https://doi.org/10.1146/annurev-neuro-092519-101637

Jaekel, J., Sorg, C., Baeuml, J., Bartmann, P., Wolke, D., 2019. Head Growth and Intelligence from Birth to Adulthood in Very Preterm and Term Born Individuals. J. Int. Neuropsychol. Soc. 25, 48–56. https://doi.org/10.1017/S135561771800084X

Jenkinson, M., Bannister, P., Brady, M., Smith, S., 2002. Improved Optimization for the Robust and Accurate Linear Registration and Motion Correction of Brain Images. NeuroImage 17, 825–841. https://doi.org/10.1006/nimg.2002.1132

Johnson, J.I., Fenske, B.A., 2014. Chapter 1 - History of the Study and Nomenclature of the Claustrum, in: Smythies, J.R., Edelstein, L.R., Ramachandran, V.S. (Eds.), The Claustrum. Academic Press, San Diego, pp. 1–27. https://doi.org/10.1016/B978-0-12-404566-8.00001-5

Johnson, S., Hollis, C., Kochhar, P., Hennessy, E., Wolke, D., Marlow, N., 2010. Psychiatric Disorders in Extremely Preterm Children: Longitudinal Finding at Age 11 Years in the EPICure Study. J. Am. Acad. Child Adolesc. Psychiatry 49, 453-463.e1. https://doi.org/10.1016/j.jaac.2010.02.002

Jones, P.B., Rantakallio, P., Hartikainen, A.-L., Isohanni, M., Sipila, P., 1998. Schizophrenia as a Long-Term Outcome of Pregnancy, Delivery, and Perinatal Complications: A 28-Year Follow-Up of the 1966 North Finland General Population Birth Cohort. Am. J. Psychiatry 155, 355–364. https://doi.org/10.1176/ajp.155.3.355

Jordan, M.I., Mitchell, T.M., 2015. Machine learning: Trends, perspectives, and prospects. Science 349, 255–260. https://doi.org/10.1126/science.aaa8415

Kanold, P.O., Luhmann, H.J., 2010. The Subplate and Early Cortical Circuits. Annu. Rev. Neurosci. 33, 23–48. https://doi.org/10.1146/annurev-neuro-060909-153244

Kanold, P.O., Shatz, C.J., 2006. Subplate Neurons Regulate Maturation of Cortical Inhibition and Outcome of Ocular Dominance Plasticity. Neuron 51, 627–638. https://doi.org/10.1016/j.neuron.2006.07.008

Kapakin, S., 2011. The claustrum: three-dimensional reconstruction, photorealistic imaging, and stereotactic approach. Folia Morphol. 70, 228–234.

Karimi, D., Salcudean, S.E., 2020. Reducing the Hausdorff Distance in Medical Image Segmentation With Convolutional Neural Networks. IEEE Trans. Med. Imaging 39, 499–513. https://doi.org/10.1109/TMI.2019.2930068

Karimi, D., Warfield, S.K., Gholipour, A., 2020. Critical Assessment of Transfer Learning for Medical Image Segmentation with Fully Convolutional Neural Networks. ArXiv200600356 Cs Eess.

Keller, S.S., Ahrens, T., Mohammadi, S., Möddel, G., Kugel, H., Bernd Ringelstein, E., Deppe, M., 2011. Microstructural and volumetric abnormalities of the putamen in juvenile myoclonic epilepsy. Epilepsia 52, 1715–1724. https://doi.org/10.1111/j.1528-1167.2011.03117.x

Kelly, C., Dhollander, T., Harding, I.H., Khan, W., Beare, R., Cheong, J.L., Doyle, L.W., Seal, M., Thompson, D.K., Inder, T.E., Anderson, P.J., 2022. Brain tissue microstructural and free-water composition 13

years after very preterm birth. NeuroImage 254, 119168. https://doi.org/10.1016/j.neuroimage.2022.119168
Kelly, C.E., Shaul, M., Thompson, D.K., Mainzer, R.M., Yang, J.Y., Dhollander, T., Cheong, J.L., Inder, T.E., Doyle, L.W., Anderson, P.J., 2023. Long-lasting effects of very preterm birth on brain structure in adulthood: A systematic review and meta-analysis. Neurosci. Biobehav. Rev. 147, 105082. https://doi.org/10.1016/j.neubiorev.2023.105082
Kinney, H.C., Haynes, R.L., Xu, G., Andiman, S.E., Folkerth, R.D., Sleeper, L.A., Volpe, J.J., 2012. Neuron deficit in the white matter and subplate in periventricular leukomalacia. Ann. Neurol. 71, 397–406. https://doi.org/10.1002/ana.22612
Kinney, H.C., Volpe, J.J., 2018. Chapter 14 - Encephalopathy of Prematurity: Neuropathology, in: Volpe, J.J., Inder, T.E., Darras, B.T., de Vries, L.S., du Plessis, A.J., Neil, J.J., Perlman, J.M. (Eds.), Volpe's Neurology of the Newborn (Sixth Edition). Elsevier, pp. 389–404. https://doi.org/10.1016/B978-0-323-42876-7.00014-4
Klein, A., Ghosh, S.S., Avants, B., Yeo, B.T.T., Fischl, B., Ardekani, B., Gee, J.C., Mann, J.J., Parsey, R.V., 2010. Evaluation of volume-based and surface-based brain image registration methods. NeuroImage 51, 214–220. https://doi.org/10.1016/j.neuroimage.2010.01.091
Kline, J.E., Dudley, J., Illapani, V.S.P., Li, H., Kline-Fath, B., Tkach, J., He, L., Yuan, W., Parikh, N.A., 2022. Diffuse excessive high signal intensity in the preterm brain on advanced MRI represents widespread neuropathology. NeuroImage 264, 119727. https://doi.org/10.1016/j.neuroimage.2022.119727
Kostović, I., Džaja, D., Raguž, M., Kopić, J., Blažević, A., Krsnik, Ž., 2022. Transient compartmentalization and accelerated volume growth coincide with the expected development of cortical afferents in the human neostriatum. Cereb. Cortex bhac076. https://doi.org/10.1093/cercor/bhac076
Kostović, I., Judaš, M., 2010. The development of the subplate and thalamocortical connections in the human foetal brain. Acta Paediatr. 99, 1119–1127. https://doi.org/10.1111/j.1651-2227.2010.01811.x
Kostovic, I., Rakic, P., 1990. Developmental history of the transient subplate zone in the visual and somatosensory cortex of the macaque monkey and human brain. J. Comp. Neurol. 297, 441–470. https://doi.org/10.1002/cne.902970309
Krimmel, S.R., White, M.G., Panicker, M.H., Barrett, F.S., Mathur, B.N., Seminowicz, D.A., 2019. Resting state functional connectivity and cognitive task-related activation of the human claustrum. NeuroImage 196, 59–67.
Kuklisova-Murgasova, M., Quaghebeur, G., Rutherford, M.A., Hajnal, J.V., Schnabel, J.A., 2012. Reconstruction of fetal brain MRI with intensity matching and complete outlier removal. Med. Image Anal. 16, 1550–1564. https://doi.org/10.1016/j.media.2012.07.004
Kurada, L., Bayat, A., Joshi, S., Koubeissi, M.Z., 2019. The Claustrum in Relation to Seizures and Electrical Stimulation. Front. Neuroanat. 13, 8. https://doi.org/10.3389/fnana.2019.00008
Le Bihan, D., 2003. Looking into the functional architecture of the brain with diffusion MRI. Nat. Rev. Neurosci. 4, 469–480. https://doi.org/10.1038/nrn1119
Lean, R.E., Han, R.H., Smyser, T.A., Kenley, J.K., Shimony, J.S., Rogers, C.E., Limbrick, D.D., Smyser, C.D., 2019. Altered neonatal white and gray matter microstructure is associated with neurodevelopmental impairments in very preterm infants with high-grade brain injury. Pediatr. Res. 86, 365–374. https://doi.org/10.1038/s41390-019-0461-1
LeCun, Y., Bengio, Y., Hinton, G., 2015. Deep learning. Nature 521, 436–444. https://doi.org/10.1038/nature14539
Lee, J.K., Liu, D., Jiang, D., Kulikowicz, E., Tekes, A., Liu, P., Qin, Q., Koehler, R.C., Aggarwal, M., Zhang, J., Martin, L.J., 2021. Fractional anisotropy from diffusion tensor imaging correlates with acute astrocyte and myelin swelling in neonatal swine models of excitotoxic and hypoxic-ischemic brain injury. J. Comp. Neurol. 529, 2750–2770. https://doi.org/10.1002/cne.25121
Lee, J.K., Liu, D., Raven, E.P., Jiang, D., Liu, P., Qin, Q., Kulikowicz, E., Santos, P.T., Adams, S., Zhang, J., Koehler, R.C., Martin, L.J., Tekes, A., 2020. Mean Diffusivity in Striatum Correlates With Acute Neuronal Death but Not Lesser Neuronal Injury in a Pilot Study of Neonatal Piglets With Encephalopathy. J. Magn. Reson. Imaging 52, 1216–1226. https://doi.org/10.1002/jmri.27181
Li, H., Menegaux, A., Schmitz-Koep, B., Neubauer, A., Bäuerlein, F.J.B., Shit, S., Sorg, C., Menze, B., Hedderich, D., 2021. Automated claustrum segmentation in human brain MRI using deep learning. Hum. Brain Mapp. 42, 5862–5872. https://doi.org/10.1002/hbm.25655
Litjens, G., Kooi, T., Bejnordi, B.E., Setio, A.A.A., Ciompi, F., Ghafoorian, M., van der Laak, J.A.W.M., van Ginneken, B., Sánchez, C.I., 2017. A survey on deep learning in medical image analysis. Med. Image

Anal. 42, 60–88. https://doi.org/10.1016/j.media.2017.07.005
Liu, J., Wu, R., Johnson, B., Vu, J., Bass, C., Li, J.-X., 2019. The Claustrum-Prefrontal Cortex Pathway Regulates Impulsive-Like Behavior. J. Neurosci. 39, 10071–10080. https://doi.org/10.1523/JNEUROSCI.1005-19.2019
Luhmann, H.J., Kilb, W., Hanganu-Opatz, I., 2009. Subplate cells: amplifiers of neuronal activity in the developing cerebral cortex. Front. Neuroanat. 3, 19.
Luhmann, H.J., Kirischuk, S., Kilb, W., 2018. The superior function of the subplate in early neocortical development. Front. Neuroanat. 12, 97.
Makropoulos, A., Aljabar, P., Wright, R., Hüning, B., Merchant, N., Arichi, T., Tusor, N., Hajnal, J.V., Edwards, A.D., Counsell, S.J., Rueckert, D., 2016. Regional growth and atlasing of the developing human brain. NeuroImage 125, 456–478. https://doi.org/10.1016/j.neuroimage.2015.10.047
Makropoulos, A., Counsell, S.J., Rueckert, D., 2018a. A review on automatic fetal and neonatal brain MRI segmentation. NeuroImage, Segmenting the Brain 170, 231–248. https://doi.org/10.1016/j.neuroimage.2017.06.074
Makropoulos, A., Gousias, I.S., Ledig, C., Aljabar, P., Serag, A., Hajnal, J.V., Edwards, A.D., Counsell, S.J., Rueckert, D., 2014. Automatic whole brain MRI segmentation of the developing neonatal brain. IEEE Trans. Med. Imaging 33, 1818–1831. https://doi.org/10.1109/TMI.2014.2322280
Makropoulos, A., Robinson, E.C., Schuh, A., Wright, R., Fitzgibbon, S., Bozek, J., Counsell, S.J., Steinweg, J., Vecchiato, K., Passerat-Palmbach, J., Lenz, G., Mortari, F., Tenev, T., Duff, E.P., Bastiani, M., Cordero-Grande, L., Hughes, E., Tusor, N., Tournier, J.-D., Hutter, J., Price, A.N., Teixeira, R.P.A.G., Murgasova, M., Victor, S., Kelly, C., Rutherford, M.A., Smith, S.M., Edwards, A.D., Hajnal, J.V., Jenkinson, M., Rueckert, D., 2018b. The developing human connectome project: A minimal processing pipeline for neonatal cortical surface reconstruction. NeuroImage 173, 88–112. https://doi.org/10.1016/j.neuroimage.2018.01.054
March of Dimes, PMNCH, Save the children, WHO, 2012. Born Too Soon: The Global action report on preterm Birth. World Health Organization., Geneva.
Marquand, A.F., Kia, S.M., Zabihi, M., Wolfers, T., Buitelaar, J.K., Beckmann, C.F., 2019. Conceptualizing mental disorders as deviations from normative functioning. Mol. Psychiatry 24, 1415–1424. https://doi.org/10.1038/s41380-019-0441-1
Marquand, A.F., Rezek, I., Buitelaar, J., Beckmann, C.F., 2016. Understanding Heterogeneity in Clinical Cohorts Using Normative Models: Beyond Case-Control Studies. Biol. Psychiatry, Obsessive-Compulsive Disorder 80, 552–561. https://doi.org/10.1016/j.biopsych.2015.12.023
Mars, R.B., Foxley, S., Verhagen, L., Jbabdi, S., Sallet, J., Noonan, M.P., Neubert, F.-X., Andersson, J.L., Croxson, P.L., Dunbar, R.I.M., Khrapitchev, A.A., Sibson, N.R., Miller, K.L., Rushworth, M.F.S., 2016. The extreme capsule fiber complex in humans and macaque monkeys: a comparative diffusion MRI tractography study. Brain Struct. Funct. 221, 4059–4071. https://doi.org/10.1007/s00429-015-1146-0
Mathur, B.N., 2014. The claustrum in review. Front. Syst. Neurosci. 8. https://doi.org/10.3389/fnsys.2014.00048
McClendon, E., Shaver, D.C., Degener-O'Brien, K., Gong, X., Nguyen, T., Hoerder-Suabedissen, A., Molnár, Z., Mohr, C., Richardson, B.D., Rossi, D.J., Back, S.A., 2017. Transient Hypoxemia Chronically Disrupts Maturation of Preterm Fetal Ovine Subplate Neuron Arborization and Activity. J. Neurosci. 37, 11912–11929. https://doi.org/10.1523/JNEUROSCI.2396-17.2017
McCulloch, W.S., Pitts, W., 1943. A logical calculus of the ideas immanent in nervous activity. Bull. Math. Biophys. 5, 115–133. https://doi.org/10.1007/BF02478259
McKinstry, R.C., Miller, J.H., Snyder, A.Z., Mathur, A., Schefft, G.L., Almli, C.R., Shimony, J.S., Shiran, S.I., Neil, J.J., 2002. A prospective, longitudinal diffusion tensor imaging study of brain injury in newborns. Neurology 59, 824–833. https://doi.org/10.1212/WNL.59.6.824
McQuillen, P.S., Ferriero, D.M., 2005. Perinatal subplate neuron injury: implications for cortical development and plasticity. Brain Pathol. Zurich Switz. 15, 250–260. https://doi.org/10.1111/j.1750-3639.2005.tb00528.x
Mendrik, A.M., Vincken, K.L., Kuijf, H.J., Breeuwer, M., Bouvy, W.H., De Bresser, J., Alansary, A., De Bruijne, M., Carass, A., El-Baz, A., 2015. MRBrainS challenge: online evaluation framework for brain image segmentation in 3T MRI scans. Comput. Intell. Neurosci. 2015.
Menegaux, A., Hedderich, D.M., Bäuml, J.G., Manoliu, A., Daamen, M., Berg, R.C., Preibisch, C., Zimmer, C., Boecker, H., Bartmann, P., Wolke, D., Sorg, C., Stämpfli, P., 2020. Reduced apparent fiber density in the white matter of premature-born adults. Sci. Rep. 10, 17214. https://doi.org/10.1038/s41598-020-73717-6

Meng, C., Bäuml, J.G., Daamen, M., Jaekel, J., Neitzel, J., Scheef, L., Busch, B., Baumann, N., Boecker, H., Zimmer, C., Bartmann, P., Wolke, D., Wohlschläger, A.M., Sorg, C., 2016. Extensive and interrelated subcortical white and gray matter alterations in preterm-born adults. Brain Struct. Funct. 221, 2109–2121. https://doi.org/10.1007/s00429-015-1032-9

Ment, L.R., Hirtz, D., Hüppi, P.S., 2009. Imaging biomarkers of outcome in the developing preterm brain. Lancet Neurol. 8, 1042–1055. https://doi.org/10.1016/S1474-4422(09)70257-1

Milardi, D., Bramanti, P., Milazzo, C., Finocchio, G., Arrigo, A., Santoro, G., Trimarchi, F., Quartarone, A., Anastasi, G., Gaeta, M., 2015. Cortical and subcortical connections of the human claustrum revealed in vivo by constrained spherical deconvolution tractography. Cereb. Cortex 25, 406–414. https://doi.org/10.1093/cercor/bht231

Millar, L.J., Shi, L., Hoerder-Suabedissen, A., Molnár, Z., 2017. Neonatal Hypoxia Ischaemia: Mechanisms, Models, and Therapeutic Challenges. Front. Cell. Neurosci. 11. https://doi.org/10.3389/fncel.2017.00078

Milletari, F., Navab, N., Ahmadi, S.-A., 2016. V-net: Fully convolutional neural networks for volumetric medical image segmentation, in: 2016 Fourth International Conference on 3D Vision (3DV). IEEE, pp. 565–571.

Molnár, Z., Luhmann, H.J., Kanold, P.O., 2020. Transient cortical circuits match spontaneous and sensory-driven activity during development. Science 370. https://doi.org/10.1126/science.abb2153

Mori, S., Barker, P.B., 1999. Diffusion magnetic resonance imaging: Its principle and applications. Anat. Rec. 257, 102–109. https://doi.org/10.1002/(SICI)1097-0185(19990615)257:3<102::AID-AR7>3.0.CO;2-6

Mori, S., Zhang, J., 2006. Principles of Diffusion Tensor Imaging and Its Applications to Basic Neuroscience Research. Neuron 51, 527–539. https://doi.org/10.1016/j.neuron.2006.08.012

Mukherjee, P., Berman, J.I., Chung, S.W., Hess, C.P., Henry, R.G., 2008. Diffusion Tensor MR Imaging and Fiber Tractography: Theoretic Underpinnings. Am. J. Neuroradiol. 29, 632–641. https://doi.org/10.3174/ajnr.A1051

Narikiyo, K., Mizuguchi, R., Ajima, A., Shiozaki, M., Hamanaka, H., Johansen, J.P., Mori, K., Yoshihara, Y., 2020. The claustrum coordinates cortical slow-wave activity. Nat. Neurosci. 23, 741–753. https://doi.org/10.1038/s41593-020-0625-7

Neubauer, A., Li, H.B., Wendt, J., Schmitz-Koep, B., Menegaux, A., Schinz, D., Menze, B., Zimmer, C., Sorg, C., Hedderich, D.M., 2022. Efficient Claustrum Segmentation in T2-weighted Neonatal Brain MRI Using Transfer Learning from Adult Scans. Clin. Neuroradiol. 32, 665–676. https://doi.org/10.1007/s00062-021-01137-8

Neubauer, A., Menegaux, A., Wendt, J., Li, H.B., Schmitz-Koep, B., Ruzok, T., Thalhammer, M., Schinz, D., Bartmann, P., Wolke, D., Priller, J., Zimmer, C., Rueckert, D., Hedderich, D.M., Sorg, C., 2023. Aberrant claustrum structure in preterm-born neonates: an MRI study. NeuroImage Clin. 37, 103286. https://doi.org/10.1016/j.nicl.2022.103286

Nosarti, C., Giouroukou, E., Healy, E., Rifkin, L., Walshe, M., Reichenberg, A., Chitnis, X., Williams, S.C.R., Murray, R.M., 2008. Grey and white matter distribution in very preterm adolescents mediates neurodevelopmental outcome. Brain 131, 205–217. https://doi.org/10.1093/brain/awm282

Nosarti, C., Mechelli, A., Herrera, A., Walshe, M., Shergill, S.S., Murray, R.M., Rifkin, L., Allin, M.P.G., 2011. Structural covariance in the cortex of very preterm adolescents: A voxel-based morphometry study. Hum. Brain Mapp. 32, 1615–1625. https://doi.org/10.1002/hbm.21133

Nosarti, C., Reichenberg, A., Murray, R.M., Cnattingius, S., Lambe, M.P., Yin, L., MacCabe, J., Rifkin, L., Hultman, C.M., 2012. Preterm Birth and Psychiatric Disorders in Young Adult Life. Arch. Gen. Psychiatry 69, 610–617. https://doi.org/10.1001/archgenpsychiatry.2011.1374

O'Shea, K., Nash, R., 2015. An Introduction to Convolutional Neural Networks. ArXiv151108458 Cs.

Padilla, N., Alexandrou, G., Blennow, M., Lagercrantz, H., Ådén, U., 2015. Brain Growth Gains and Losses in Extremely Preterm Infants at Term. Cereb. Cortex 25, 1897–1905. https://doi.org/10.1093/cercor/bht431

Pan, S.J., Yang, Q., 2010. A Survey on Transfer Learning. IEEE Trans. Knowl. Data Eng. 22, 1345–1359. https://doi.org/10.1109/TKDE.2009.191

Pecheva, D., Kelly, C., Kimpton, J., Bonthrone, A., Batalle, D., Zhang, H., Counsell, S.J., 2018. Recent advances in diffusion neuroimaging: applications in the developing preterm brain. F1000Research 7, F1000 Faculty Rev-1326. https://doi.org/10.12688/f1000research.15073.1

Perkinson-Gloor, N., Hagmann-von Arx, P., Brand, S., Holsboer-Trachsler, E., Grob, A., Weber, P., Lemola, S., 2015. The role of sleep and the hypothalamic-pituitary-adrenal axis for behavioral and emotional

problems in very preterm children during middle childhood. J. Psychiatr. Res. 60, 141–147. https://doi.org/10.1016/j.jpsychires.2014.10.005
Petrides, M., Pandya, D.N., 2007. Efferent Association Pathways from the Rostral Prefrontal Cortex in the Macaque Monkey. J. Neurosci. 27, 11573–11586. https://doi.org/10.1523/JNEUROSCI.2419-07.2007
Petrides, M., Pandya, D.N., 1988. Association fiber pathways to the frontal cortex from the superior temporal region in the rhesus monkey. J. Comp. Neurol. 273, 52–66. https://doi.org/10.1002/cne.902730106
Pfefferbaum, A., Adalsteinsson, E., Rohlfing, T., Sullivan, E.V., 2010. Diffusion tensor imaging of deep gray matter brain structures: Effects of age and iron concentration. Neurobiol. Aging 31, 482–493. https://doi.org/10.1016/j.neurobiolaging.2008.04.013
Pierpaoli, C., Basser, P.J., 1996. Toward a quantitative assessment of diffusion anisotropy. Magn. Reson. Med. 36, 893–906. https://doi.org/10.1002/mrm.1910360612
Puelles, L., 2014. Development and Evolution of the Claustrum, in: Smythies, J.R., Edelstein, L., Ramachandran, V.S. (Eds.), The Claustrum: Structural, Functional, and Clinical Neuroscience. Academic Press, pp. 119–176. https://doi.org/10.1016/B978-0-12-404566-8.00004-0
Purisch, S.E., Gyamfi-Bannerman, C., 2017. Epidemiology of preterm birth. Semin. Perinatol., Current Preterm Birth Prevention Strategies 41, 387–391. https://doi.org/10.1053/j.semperi.2017.07.009
Qadir, H., Krimmel, S.R., Mu, C., Poulopoulos, A., Seminowicz, D.A., Mathur, B.N., 2018. Structural Connectivity of the Anterior Cingulate Cortex, Claustrum, and the Anterior Insula of the Mouse. Front. Neuroanat. 12.
Raybaud, C., Ahmad, T., Rastegar, N., Shroff, M., Al Nassar, M., 2013. The premature brain: developmental and lesional anatomy. Neuroradiology 55, 23–40.
Reemst, K., Noctor, S.C., Lucassen, P.J., Hol, E.M., 2016. The Indispensable Roles of Microglia and Astrocytes during Brain Development. Front. Hum. Neurosci. 10.
Ronneberger, O., Fischer, P., Brox, T., 2015. U-Net: Convolutional Networks for Biomedical Image Segmentation, in: Navab, N., Hornegger, J., Wells, W.M., Frangi, A.F. (Eds.), Medical Image Computing and Computer-Assisted Intervention – MICCAI 2015, Lecture Notes in Computer Science. Springer International Publishing, Cham, pp. 234–241. https://doi.org/10.1007/978-3-319-24574-4_28
Rose, J., Vassar, R., Cahill-Rowley, K., Stecher Guzman, X., Hintz, S.R., Stevenson, D.K., Barnea-Goraly, N., 2014. Neonatal physiological correlates of near-term brain development on MRI and DTI in very-low-birth-weight preterm infants. NeuroImage Clin. 5, 169–177. https://doi.org/10.1016/j.nicl.2014.05.013
Rose, S.E., Janke PhD, A.L., Chalk, J.B., 2008. Gray and white matter changes in Alzheimer's disease: A diffusion tensor imaging study. J. Magn. Reson. Imaging 27, 20–26. https://doi.org/10.1002/jmri.21231
Rosenblatt, F., 1958. The perceptron: A probabilistic model for information storage and organization in the brain. Psychol. Rev. 65, 386–408. https://doi.org/10.1037/h0042519
Russell, S., Norvig, P., 2016. Artificial Intelligence: A Modern Approach. Pearson.
Rutherford, M., Counsell, S., Allsop, J., Boardman, J., Kapellou, O., Larkman, D., Hajnal, J., Edwards, D., Cowan, F., 2004. Diffusion-Weighted Magnetic Resonance Imaging in Term Perinatal Brain Injury: A Comparison With Site of Lesion and Time From Birth. Pediatrics 114, 1004–1014. https://doi.org/10.1542/peds.2004-0222
Rutherford, M., Pennock, J., Schwieso, J., Cowan, F., Dubowitz, L., 1996. Hypoxic-ischaemic encephalopathy: early and late magnetic resonance imaging findings in relation to outcome. Arch. Dis. Child. - Fetal Neonatal Ed. 75, F145–F151. https://doi.org/10.1136/fn.75.3.F145
Saigal, S., Stoskopf, B., Streiner, D., Paneth, N., Pinelli, J., Boyle, M., 2006. Growth Trajectories of Extremely Low Birth Weight Infants From Birth to Young Adulthood: A Longitudinal, Population-Based Study. Pediatr. Res. 60, 751–758. https://doi.org/10.1203/01.pdr.0000246201.93662.8e
Salmaso, N., Jablonska, B., Scafidi, J., Vaccarino, F.M., Gallo, V., 2014. Neurobiology of premature brain injury. Nat. Neurosci. 17, 341–346. https://doi.org/10.1038/nn.3604
Sartorius, G.A., Nieschlag, E., 2010. Paternal age and reproduction. Hum. Reprod. Update 16, 65–79. https://doi.org/10.1093/humupd/dmp027
Scheinost, D., Kwon, S.H., Lacadie, C., Vohr, B.R., Schneider, K.C., Papademetris, X., Constable, R.T., Ment, L.R., 2017. Alterations in Anatomical Covariance in the Prematurely Born. Cereb. Cortex 27, 534–543. https://doi.org/10.1093/cercor/bhv248
Schmahmann, J.D., Pandya, D., 2006. Fiber Pathways of the Brain. Oxford University Press, USA.
Schmidhuber, J., 2015. Deep learning in neural networks: An overview. Neural Netw. 61, 85–117. https://doi.org/10.1016/j.neunet.2014.09.003

Schmitz-Koep, B., Haller, B., Coupé, P., Menegaux, A., Gaser, C., Zimmer, C., Wolke, D., Bartmann, P., Sorg, C., Hedderich, D.M., 2021a. Grey and white matter volume changes after preterm birth: A meta-analytic approach. https://doi.org/10.1101/2021.06.15.21258937

Schmitz-Koep, B., Zimmermann, J., Menegaux, A., Nuttall, R., Bäuml, J.G., Schneider, S.C., Daamen, M., Boecker, H., Zimmer, C., Wolke, D., Bartmann, P., Hedderich, D.M., Sorg, C., 2021b. Decreased amygdala volume in adults after premature birth. Sci. Rep. 11, 5403. https://doi.org/10.1038/s41598-021-84906-2

Shah, P.S., Ohlsson, A., Perlman, M., 2007. Hypothermia to Treat Neonatal Hypoxic Ischemic Encephalopathy: Systematic Review. Arch. Pediatr. Adolesc. Med. 161, 951–958. https://doi.org/10.1001/archpedi.161.10.951

Shin, H.-C., Roth, H.R., Gao, M., Lu, L., Xu, Z., Nogues, I., Yao, J., Mollura, D., Summers, R.M., 2016. Deep Convolutional Neural Networks for Computer-Aided Detection: CNN Architectures, Dataset Characteristics and Transfer Learning. IEEE Trans. Med. Imaging 35, 1285–1298. https://doi.org/10.1109/TMI.2016.2528162

Skiöld, B., Alexandrou, G., Padilla, N., Blennow, M., Vollmer, B., Ådén, U., 2014. Sex Differences in Outcome and Associations with Neonatal Brain Morphology in Extremely Preterm Children. J. Pediatr. 164, 1012–1018. https://doi.org/10.1016/j.jpeds.2013.12.051

Smith, J.B., Alloway, K.D., Hof, P.R., Orman, R., Reser, D.H., Watakabe, A., Watson, G.D.R., 2018. The relationship between the claustrum and endopiriform nucleus: A perspective towards consensus on cross-species homology. J. Comp. Neurol. 527, 476–499. https://doi.org/10.1002/cne.24537

Smith, J.B., Lee, A.K., Jackson, J., 2020. The claustrum. Curr. Biol. 30, R1401–R1406. https://doi.org/10.1016/j.cub.2020.09.069

Smith, J.B., Radhakrishnan, H., Alloway, K.D., 2012. Rat claustrum coordinates but does not integrate somatosensory and motor cortical information. J. Neurosci. 32, 8583–8588.

Smith, S.M., 2004. Overview of fMRI analysis. Br. J. Radiol. 77, S167–S175. https://doi.org/10.1259/bjr/33553595

Smith, S.M., 2002. Fast robust automated brain extraction. Hum. Brain Mapp. 17, 143–155. https://doi.org/10.1002/hbm.10062

Smith, S.M., Jenkinson, M., Johansen-Berg, H., Rueckert, D., Nichols, T.E., Mackay, C.E., Watkins, K.E., Ciccarelli, O., Cader, M.Z., Matthews, P.M., Behrens, T.E.J., 2006. Tract-based spatial statistics: Voxelwise analysis of multi-subject diffusion data. NeuroImage 31, 1487–1505. https://doi.org/10.1016/j.neuroimage.2006.02.024

Srinivasan, L., Dutta, R., Counsell, S.J., Allsop, J.M., Boardman, J.P., Rutherford, M.A., Edwards, A.D., 2007. Quantification of Deep Gray Matter in Preterm Infants at Term-Equivalent Age Using Manual Volumetry of 3-Tesla Magnetic Resonance Images. Pediatrics 119, 759–765. https://doi.org/10.1542/peds.2006-2508

Stiles, J., Jernigan, T.L., 2010. The Basics of Brain Development. Neuropsychol. Rev. 20, 327–348. https://doi.org/10.1007/s11065-010-9148-4

Sun, T., Patoine, C., Abu-Khalil, A., Visvader, J., Sum, E., Cherry, T.J., Orkin, S.H., Geschwind, D.H., Walsh, C.A., 2005. Early Asymmetry of Gene Transcription in Embryonic Human Left and Right Cerebral Cortex. Science 308, 1794–1798. https://doi.org/10.1126/science.1110324

Taha, A.A., Hanbury, A., 2015. Metrics for evaluating 3D medical image segmentation: analysis, selection, and tool. BMC Med. Imaging 15, 29. https://doi.org/10.1186/s12880-015-0068-x

Tauzin, L., 2015. Alterations in viscoelastic properties following premature birth may lead to hypertension and cardiovascular disease development in later life. Acta Paediatr. 104, 19–26. https://doi.org/10.1111/apa.12815

Thompson, D.K., Inder, T.E., Faggian, N., Johnston, L., Warfield, S.K., Anderson, P.J., Doyle, L.W., Egan, G.F., 2011. Characterization of the corpus callosum in very preterm and full-term infants utilizing MRI. NeuroImage 55, 479–490. https://doi.org/10.1016/j.neuroimage.2010.12.025

Torgerson, C.M., Irimia, A., Goh, S.M., Van Horn, J.D., 2015. The DTI connectivity of the human claustrum. Hum. Brain Mapp. 36, 827–838.

Twilhaar, E.S., Kieviet, J.F. de, Aarnoudse-Moens, C.S., Elburg, R.M. van, Oosterlaan, J., 2018a. Academic performance of children born preterm: a meta-analysis and meta-regression. Arch. Dis. Child. - Fetal Neonatal Ed. 103, F322–F330. https://doi.org/10.1136/archdischild-2017-312916

Twilhaar, E.S., Wade, R.M., de Kieviet, J.F., van Goudoever, J.B., van Elburg, R.M., Oosterlaan, J., 2018b. Cognitive Outcomes of Children Born Extremely or Very Preterm Since the 1990s and Associated Risk

Factors: A Meta-analysis and Meta-regression. JAMA Pediatr. 172, 361–367. https://doi.org/10.1001/jamapediatrics.2017.5323
van Opbroek, A., Ikram, M.A., Vernooij, M.W., de Bruijne, M., 2015. Transfer Learning Improves Supervised Image Segmentation Across Imaging Protocols. IEEE Trans. Med. Imaging 34, 1018–1030. https://doi.org/10.1109/TMI.2014.2366792
Vangberg, T.R., Skranes, J., Dale, A.M., Martinussen, M., Brubakk, A.-M., Haraldseth, O., 2006. Changes in white matter diffusion anisotropy in adolescents born prematurely. NeuroImage 32, 1538–1548. https://doi.org/10.1016/j.neuroimage.2006.04.230
Vasung, L., Huang, H., Jovanov-Milošević, N., Pletikos, M., Mori, S., Kostović, I., 2010. Development of axonal pathways in the human fetal fronto-limbic brain: histochemical characterization and diffusion tensor imaging. J. Anat. 217, 400–417. https://doi.org/10.1111/j.1469-7580.2010.01260.x
Vollmar, C., O'Muircheartaigh, J., Barker, G.J., Symms, M.R., Thompson, P., Kumari, V., Duncan, J.S., Richardson, M.P., Koepp, M.J., 2010. Identical, but not the same: Intra-site and inter-site reproducibility of fractional anisotropy measures on two 3.0T scanners. NeuroImage 51, 1384–1394. https://doi.org/10.1016/j.neuroimage.2010.03.046
Volpe, J.J., 2019. Dysmaturation of Premature Brain: Importance, Cellular Mechanisms, and Potential Interventions. Pediatr. Neurol. 95, 42–66. https://doi.org/10.1016/j.pediatrneurol.2019.02.016
Volpe, J.J., 2009. Brain injury in premature infants: a complex amalgam of destructive and developmental disturbances. Lancet Neurol. 8, 110–124. https://doi.org/10.1016/S1474-4422(08)70294-1
Volpe, J.J., 1996. Subplate Neurons-Missing Link in Brain Injury of the Premature Infant? Pediatrics 97, 112–113.
Wang, W., Yu, Q., Liang, W., Xu, F., Li, Z., Tang, Y., Liu, S., 2022. Altered cortical microstructure in preterm infants at term-equivalent age relative to term-born neonates. Cereb. Cortex bhac091. https://doi.org/10.1093/cercor/bhac091
Ward, P., Counsell, S., Allsop, J., Cowan, F., Shen, Y., Edwards, D., Rutherford, M., 2006. Reduced Fractional Anisotropy on Diffusion Tensor Magnetic Resonance Imaging After Hypoxic-Ischemic Encephalopathy. Pediatrics 117, e619–e630. https://doi.org/10.1542/peds.2005-0545
Ward, R.M., Beachy, J.C., 2003. Neonatal complications following preterm birth. BJOG Int. J. Obstet. Gynaecol. 110, 8–16. https://doi.org/10.1046/j.1471-0528.2003.00012.x
Watanabe, K., Iwase, K., Hara, K., 1974. Development of Slow-wave Sleep in Low-birthweight Infants. Dev. Med. Child Neurol. 16, 23–31. https://doi.org/10.1111/j.1469-8749.1974.tb02707.x
Watson, C., Puelles, L., 2017. Developmental gene expression in the mouse clarifies the organization of the claustrum and related endopiriform nuclei. J. Comp. Neurol. 525, 1499–1508.
Wehrle, F.M., Latal, B., O'Gorman, R.L., Hagmann, C.F., Huber, R., 2017. Sleep EEG maps the functional neuroanatomy of executive processes in adolescents born very preterm. Cortex J. Devoted Study Nerv. Syst. Behav. 86, 11–21. https://doi.org/10.1016/j.cortex.2016.10.011
Weishaupt, D., Köchli, V.D., Marincek, B., 2009. Wie funktioniert MRI?: Eine Einführung in Physik und Funktionsweise der Magnetresonanzbildgebung, 6th ed. Springer-Verlag, Berlin Heidelberg. https://doi.org/10.1007/978-3-642-41616-3
White, M.G., Panicker, M., Mu, C., Carter, A.M., Roberts, B.M., Dharmasri, P.A., Mathur, B.N., 2018. Anterior Cingulate Cortex Input to the Claustrum Is Required for Top-Down Action Control. Cell Rep. 22, 84–95. https://doi.org/10.1016/j.celrep.2017.12.023
Wisse, L.E.M., Kuijf, H.J., Honingh, A.M., Wang, H., Pluta, J.B., Das, S.R., Wolk, D.A., Zwanenburg, J.J.M., Yushkevich, P.A., Geerlings, M.I., 2016. Automated Hippocampal Subfield Segmentation at 7T MRI. Am. J. Neuroradiol. 37, 1050–1057. https://doi.org/10.3174/ajnr.A4659
Wolke, D., Johnson, S., Mendonça, M., 2019. The life course consequences of very preterm birth. Annu. Rev. Dev. Psychol. 1, 69–92.
Woodward, L.J., Anderson, P.J., Austin, N.C., Howard, K., Inder, T.E., 2006. Neonatal MRI to Predict Neurodevelopmental Outcomes in Preterm Infants. N. Engl. J. Med. 355, 685–694. https://doi.org/10.1056/NEJMoa053792
Yushkevich, P.A., Piven, J., Hazlett, H.C., Smith, R.G., Ho, S., Gee, J.C., Gerig, G., 2006. User-guided 3D active contour segmentation of anatomical structures: Significantly improved efficiency and reliability. NeuroImage 31, 1116–1128. https://doi.org/10.1016/j.neuroimage.2006.01.015
Zhang, H., Schneider, T., Wheeler-Kingshott, C.A., Alexander, D.C., 2012. NODDI: practical in vivo neurite orientation dispersion and density imaging of the human brain. NeuroImage 61, 1000–1016. https://doi.org/10.1016/j.neuroimage.2012.03.072

Zilles, K., Palomero-Gallagher, N., Amunts, K., 2013. Development of cortical folding during evolution and ontogeny. Trends Neurosci. 36, 275–284. https://doi.org/10.1016/j.tins.2013.01.006

## Supplement

The Supplement includes, first, the protocol for manual claustrum segmentation in neonatal brain MRI, and second, the detailed results of the claustrum covariance analysis split up into individual regions.

## Supplement A: Claustrum segmentation protocol for neonatal brain MRI

Protocol reproduced with added Figure captions from the Online Supplement of Neubauer et al. (2022), used under CC By:

T2-weighted images are provided by the developing Human Connectome Project (http://www.developingconnectome.org/project/).

1 Find a slice in axial sight where you can easily recognize the claustrum. Then adjust the image contrast to optimize the differentiation of the claustrum in comparison to surrounding white matter.

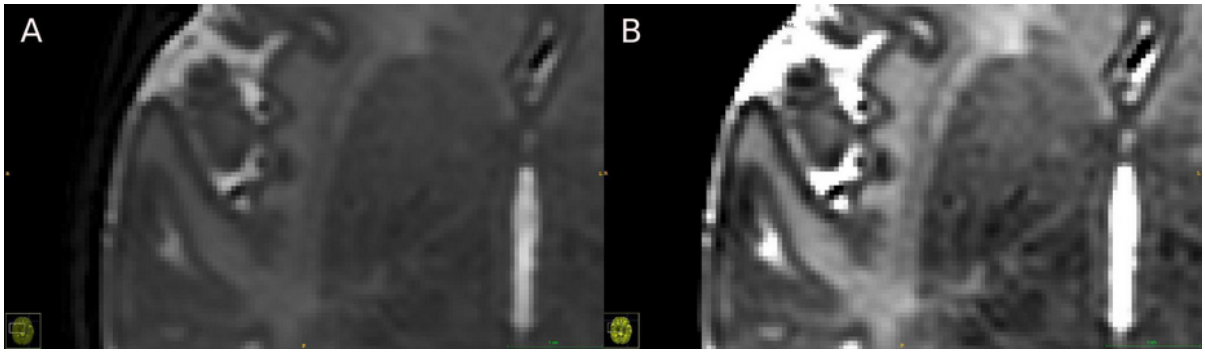


***Figure A1: Image section with the right claustrum of a T2-weighted neonatal brain MRI.***

2 Select the axial plane and zoom in. The favored extract captures the claustrum and adjacent anatomical structures like the putamen and the insula for orientation. Single voxels should be identifiable without struggle.

3 To start with actual segmentation, focus on the claustrum of interest. In this protocol, all integrated figures show sections with the right claustrum. Choose a slice with visible claustrum with long continuous appearance in anterior-posterior dimension and trace it with a selected label. Avoid marking any voxel which is part of the insular cortex or the basal ganglia. If the claustrum seems to be directly next to them try to leave a small distance between segmentation and neighboring structure.

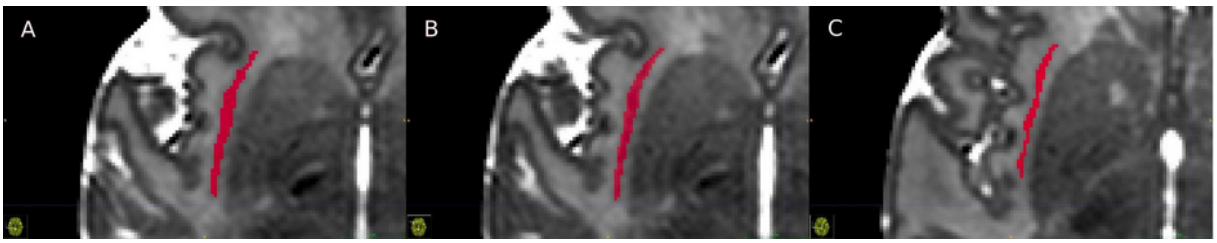


***Figure A2: Axial MRI slices with manual claustrum segmentation.***

4 Continue with the slice below and go on until you can not surely define the measure of the claustrum anymore. In general, do not include rays of gray matter which sometimes emerge from the claustrum. Only incorporate voxels at the same level like the residual claustrum surface.

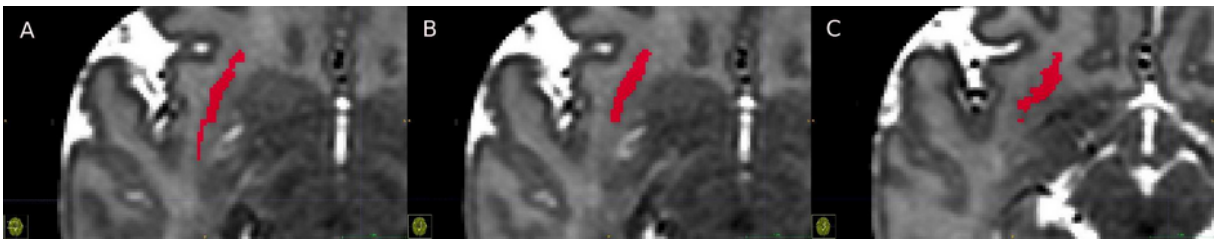


***Figure A3: Ventral axial MRI slices with manual claustrum segmentation.***

5 Go back to your starting slice and repeat the previous step but in the dorsal direction. In this direction, the visible claustrum is often separated in several parts.

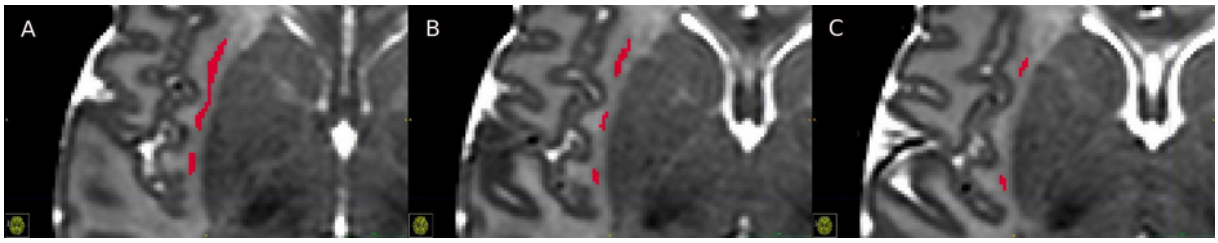


***Figure A4: Dorsal axial MRI slices with manual claustrum segmentation.***

6 Afterward, switch to the coronal plane and again start with a central slice and go backward slice per slice, then forward. Supplement the segmentation especially the ventral part of the claustrum which expands under the putamen. It is easier to assess this area in coronal than in axial view. Correct the tracing if necessary by using the "clear label“. Therefore, it is helpful to modulate the opacity of the label.

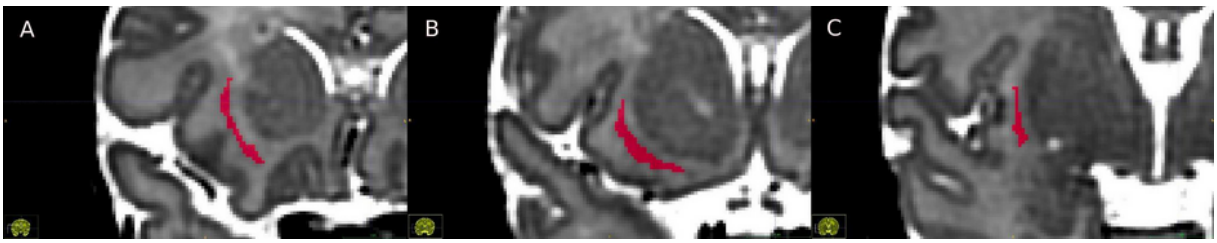


***Figure A5: Coronal MRI slices with manual claustrum segmentation.***

7 Return to the axial plane and correct details where needed to enhance reliability. Again, mind a small distance between segmented claustrum and other structures.

8 To trace the second claustrum, repeat steps three to seven with another label if requested.

## Supplement B: Correlation analysis of the claustrum

Detailed results of the claustrum covariance analysis. The results are split up into the individual brain regions defined by the Draw-EM segmentation provided by the developing Human Connectome Project.

***Table B1: Claustrum covariance with other brain regions regarding the absolute volume.***

| Region | PT (right cla) | FT (right cla) | p_FDR (right cla) | PT (left cla) | FT (left cla) | p_FDR (left cla) |
|---|---|---|---|---|---|---|
| lh hippocampus | 0.527 | 0.465 | 0.986 | 0.486 | 0.341 | 0.965 |
| rh hippocampus | 0.523 | 0.418 | 0.986 | 0.500 | 0.319 | 0.965 |
| lh amygdala | 0.753 | 0.599 | 0.986 | 0.738 | 0.507 | 0.965 |
| rh amygdala | 0.663 | 0.648 | 0.986 | 0.616 | 0.532 | 0.965 |
| lh ant. temp. med. GM | 0.363 | 0.269 | 0.986 | 0.311 | 0.156 | 0.965 |
| rh ant. temp. med. GM | 0.338 | 0.324 | 0.986 | 0.309 | 0.233 | 0.965 |
| lh ant. temp. lat. GM | 0.511 | 0.289 | 0.986 | 0.421 | 0.173 | 0.965 |
| rh ant. temp. lat. GM | 0.368 | 0.353 | 0.986 | 0.328 | 0.255 | 0.965 |
| lh ant. parahippocampal GM | 0.726 | 0.363 | 0.966 | 0.656 | 0.256 | 0.829 |
| rh ant. parahippocampal GM | 0.566 | 0.424 | 0.986 | 0.494 | 0.328 | 0.965 |
| lh sup. temp. middle gyrus GM | 0.423 | 0.380 | 0.986 | 0.384 | 0.229 | 0.965 |
| rh sup. temp. middle gyrus GM | 0.372 | 0.441 | 0.986 | 0.361 | 0.275 | 0.965 |
| lh med.-inf. temp. ant. gyrus GM | 0.495 | 0.502 | 0.986 | 0.424 | 0.343 | 0.965 |
| rh med.-inf. temp. ant. gyrus GM | 0.370 | 0.412 | 0.986 | 0.376 | 0.358 | 0.965 |
| lh lat. occ.-temp. ant. gyrus GM | 0.434 | 0.290 | 0.986 | 0.313 | 0.257 | 0.965 |
| rh lat. occ.-temp. ant. gyrus GM | 0.465 | 0.393 | 0.986 | 0.394 | 0.256 | 0.965 |
| lh cerebellum | 0.366 | 0.443 | 0.986 | 0.283 | 0.310 | 0.965 |
| rh cerebellum | 0.357 | 0.445 | 0.986 | 0.283 | 0.312 | 0.965 |
| brainstem | 0.612 | 0.618 | 0.986 | 0.571 | 0.469 | 0.965 |
| rh insula GM | 0.508 | 0.571 | 0.986 | 0.532 | 0.427 | 0.965 |
| lh insula GM | 0.528 | 0.601 | 0.986 | 0.548 | 0.469 | 0.965 |

| | | | | | | |
|---|---|---|---|---|---|---|
| rh occipital GM | 0.547 | 0.555 | 0.986 | 0.473 | 0.419 | 0.965 |
| lh occipital GM | 0.479 | 0.611 | 0.986 | 0.432 | 0.495 | 0.965 |
| rh post. parahippocampal GM | 0.282 | 0.430 | 0.986 | 0.253 | 0.360 | 0.965 |
| lh post. parahippocampal GM | 0.389 | 0.338 | 0.986 | 0.342 | 0.269 | 0.965 |
| rh lat. occ.-temp. post. gyrus GM | 0.462 | 0.295 | 0.986 | 0.380 | 0.203 | 0.965 |
| lh lat. occ.-temp. post. gyrus GM | 0.432 | 0.360 | 0.986 | 0.364 | 0.235 | 0.965 |
| rh med.-inf. temp. post. gyrus GM | 0.470 | 0.461 | 0.986 | 0.411 | 0.386 | 0.965 |
| lh med.-inf. temp. post. gyrus GM | 0.491 | 0.567 | 0.986 | 0.472 | 0.448 | 0.965 |
| rh sup. temp. post. gyrus GM | 0.351 | 0.393 | 0.986 | 0.294 | 0.313 | 0.965 |
| lh sup. temp. post. gyrus GM | 0.360 | 0.365 | 0.986 | 0.338 | 0.245 | 0.965 |
| rh ant. cingulate gyrus GM | 0.399 | 0.398 | 0.995 | 0.435 | 0.321 | 0.965 |
| lh ant. cingulate gyrus GM | 0.202 | 0.235 | 0.986 | 0.270 | 0.199 | 0.965 |
| rh post. cingulate gyrus GM | 0.412 | 0.436 | 0.986 | 0.437 | 0.308 | 0.965 |
| lh post. cingulate gyrus GM | 0.351 | 0.500 | 0.986 | 0.324 | 0.380 | 0.965 |
| rh frontal GM | 0.541 | 0.576 | 0.986 | 0.470 | 0.408 | 0.965 |
| lh frontal GM | 0.564 | 0.574 | 0.986 | 0.492 | 0.405 | 0.965 |
| rh parietal GM | 0.398 | 0.440 | 0.986 | 0.377 | 0.331 | 0.965 |
| lh parietal GM | 0.453 | 0.466 | 0.986 | 0.414 | 0.329 | 0.965 |
| rh caudate nucleus | 0.805 | 0.623 | 0.986 | 0.764 | 0.551 | 0.965 |
| lh caudate nucleus | 0.835 | 0.654 | 0.986 | 0.770 | 0.578 | 0.965 |
| rh thalamus high T2 intensity | 0.532 | 0.585 | 0.986 | 0.490 | 0.481 | 0.985 |
| lh thalamus high T2 intensity | 0.529 | 0.616 | 0.986 | 0.502 | 0.562 | 0.965 |
| rh subthalamic nucleus | 0.462 | 0.572 | 0.986 | 0.476 | 0.474 | 0.992 |
| lh subthalamic nucleus | 0.537 | 0.642 | 0.986 | 0.528 | 0.513 | 0.968 |
| rh lentiform nucleus | 0.542 | 0.654 | 0.986 | 0.512 | 0.554 | 0.965 |
| lh lentiform nucleus | 0.636 | 0.736 | 0.986 | 0.616 | 0.624 | 0.985 |
| corpus callosum | 0.396 | 0.551 | 0.986 | 0.431 | 0.507 | 0.965 |
| lh ant. temp. med. WM | 0.247 | 0.142 | 0.986 | 0.200 | 0.032 | 0.965 |
| rh ant. temp. med. WM | 0.220 | 0.167 | 0.986 | 0.222 | 0.099 | 0.965 |
| lh ant. temp. lat. WM | 0.474 | 0.289 | 0.986 | 0.321 | 0.159 | 0.965 |
| rh ant. temp. lat. WM | 0.379 | 0.347 | 0.986 | 0.285 | 0.251 | 0.965 |
| lh ant. parahippocampal WM | 0.478 | 0.373 | 0.986 | 0.280 | 0.282 | 0.992 |
| rh ant. parahippocampal WM | 0.390 | 0.359 | 0.986 | 0.279 | 0.336 | 0.965 |
| lh sup. temp. middle gyrus WM | 0.493 | 0.361 | 0.986 | 0.484 | 0.353 | 0.965 |
| rh sup. temp. middle gyrus WM | 0.451 | 0.589 | 0.986 | 0.506 | 0.547 | 0.965 |
| lh med.-inf. temp. ant. gyrus WM | 0.488 | 0.382 | 0.986 | 0.448 | 0.319 | 0.965 |
| rh med.-inf. temp. ant. gyrus WM | 0.418 | 0.280 | 0.986 | 0.449 | 0.426 | 0.965 |
| lh lat. occ.-temp. ant. gyrus WM | 0.353 | 0.099 | 0.986 | 0.214 | 0.096 | 0.965 |
| rh lat. occ.-temp. ant. gyrus WM | 0.410 | 0.289 | 0.986 | 0.317 | 0.232 | 0.965 |
| rh insula WM | 0.875 | 0.746 | 0.986 | 0.941 | 0.621 | 0.829 |
| lh insula WM | 0.818 | 0.661 | 0.986 | 0.883 | 0.539 | 0.829 |
| rh occipital WM | 0.723 | 0.657 | 0.986 | 0.717 | 0.608 | 0.965 |
| lh occipital WM | 0.588 | 0.669 | 0.986 | 0.688 | 0.733 | 0.965 |
| rh post. parahippocampal WM | 0.545 | 0.452 | 0.986 | 0.491 | 0.405 | 0.965 |
| lh post. parahippocampal WM | 0.476 | 0.309 | 0.986 | 0.386 | 0.315 | 0.965 |
| rh lat. occ.-temp. post. gyrus WM | 0.438 | 0.464 | 0.986 | 0.407 | 0.432 | 0.965 |

| | | | | | | |
|---|---|---|---|---|---|---|
| lh lat. occ.-temp. post. gyrus WM | 0.583 | 0.390 | 0.986 | 0.567 | 0.314 | 0.965 |
| rh med.-inf. temp. post. gyrus WM | 0.648 | 0.426 | 0.986 | 0.713 | 0.569 | 0.965 |
| lh med.-inf. temp. post. gyrus WM | 0.471 | 0.525 | 0.986 | 0.629 | 0.678 | 0.965 |
| rh sup. temp. post. gyrus WM | 0.299 | 0.388 | 0.986 | 0.330 | 0.383 | 0.965 |
| lh sup. temp. post. gyrus WM | 0.337 | 0.394 | 0.986 | 0.290 | 0.317 | 0.965 |
| rh ant. cingulate gyrus WM | 0.505 | 0.398 | 0.986 | 0.587 | 0.327 | 0.965 |
| lh ant. cingulate gyrus WM | 0.335 | 0.285 | 0.986 | 0.332 | 0.244 | 0.965 |
| rh post. cingulate gyrus WM | 0.510 | 0.384 | 0.986 | 0.520 | 0.206 | 0.829 |
| lh post. cingulate gyrus WM | 0.504 | 0.474 | 0.986 | 0.436 | 0.342 | 0.965 |
| rh frontal WM | 0.635 | 0.609 | 0.986 | 0.661 | 0.593 | 0.965 |
| lh frontal WM | 0.656 | 0.650 | 0.986 | 0.707 | 0.625 | 0.965 |
| rh parietal WM | 0.525 | 0.482 | 0.986 | 0.592 | 0.538 | 0.965 |
| lh parietal WM | 0.539 | 0.519 | 0.986 | 0.620 | 0.569 | 0.965 |
| rh thalamus low T2 intensity | 0.262 | 0.395 | 0.986 | 0.215 | 0.301 | 0.965 |
| lh thalamus low T2 intensity | 0.271 | 0.412 | 0.986 | 0.220 | 0.242 | 0.965 |
| rh claustrum | infinity | infinity | - | 1.335 | 1.176 | 0.965 |
| lh claustrum | 1.335 | 1.176 | 0.986 | infinity | infinity | - |

*The Pearson's correlation coefficients r for right and left claustrum were transformed to z-scores by Fisher transformation. The z-scores of preterm- and term-born neonates were compared for significant differences. There was no significant difference after false discovery rate correction for multiple testing (p_FDR < 0.05). Table reproduced from the Online Supplement of Neubauer et al. (2023), used under CC By. Ant. = anterior, cla = claustrum, FT = full term, GM = gray matter, inf. = inferior, lat. = lateral, lh = left hemisphere, med. = medial, occ. = occipital, post. = posterior, PT = preterm, rh = right hemisphere, sup. = superior, temp. = temporal, WM = white matter.*

***Table B2: Claustrum covariance with other brain regions regarding the total brain volume-relative volume.***

| Region | PT (right cla) | FT (right cla) | p_FDR (right cla) | PT (left cla) | FT (left cla) | p_FDR (left cla) |
|---|---|---|---|---|---|---|
| lh hippocampus | 0.191 | 0.139 | 0.958 | 0.156 | 0.108 | 0.978 |
| rh hippocampus | 0.202 | 0.017 | 0.736 | 0.203 | 0.009 | 0.978 |
| lh amygdala | 0.402 | 0.292 | 0.881 | 0.440 | 0.290 | 0.978 |
| rh amygdala | 0.279 | 0.364 | 0.897 | 0.265 | 0.338 | 0.978 |
| lh ant. temp. med. GM | -0.028 | -0.147 | 0.881 | -0.107 | -0.206 | 0.978 |
| rh ant. temp. med. GM | -0.106 | -0.241 | 0.851 | -0.164 | -0.236 | 0.978 |
| lh ant. temp. lat. GM | -0.048 | -0.238 | 0.736 | -0.210 | -0.330 | 0.978 |
| rh ant. temp. lat. GM | -0.239 | -0.231 | 0.991 | -0.329 | -0.280 | 0.978 |
| lh ant. parahippocampal GM | 0.424 | 0.094 | 0.410 | 0.362 | 0.041 | 0.613 |
| rh ant. parahippocampal GM | 0.141 | 0.066 | 0.924 | 0.064 | 0.043 | 0.984 |
| lh sup. temp. middle gyrus GM | -0.291 | -0.338 | 0.958 | -0.345 | -0.475 | 0.978 |
| rh sup. temp. middle gyrus GM | -0.375 | -0.298 | 0.924 | -0.353 | -0.462 | 0.978 |
| lh med.-inf. temp. ant. gyrus GM | -0.167 | -0.185 | 0.991 | -0.307 | -0.324 | 0.984 |
| rh med.-inf. temp. ant. gyrus GM | -0.346 | -0.357 | 0.991 | -0.325 | -0.272 | 0.978 |
| lh lat. occ.-temp. ant. gyrus GM | 0.103 | -0.182 | 0.480 | -0.039 | -0.154 | 0.978 |

| | | | | | | |
|---|---|---|---|---|---|---|
| rh lat. occ.-temp. ant. gyrus GM | -0.035 | -0.132 | 0.881 | -0.127 | -0.212 | 0.978 |
| lh cerebellum | -0.184 | -0.126 | 0.958 | -0.297 | -0.200 | 0.978 |
| rh cerebellum | -0.223 | -0.109 | 0.881 | -0.320 | -0.178 | 0.978 |
| brainstem | 0.258 | 0.344 | 0.897 | 0.259 | 0.283 | 0.978 |
| rh insula GM | -0.123 | -0.012 | 0.881 | -0.058 | -0.070 | 0.987 |
| lh insula GM | -0.108 | 0.054 | 0.813 | -0.053 | 0.007 | 0.978 |
| rh occipital GM | -0.095 | -0.144 | 0.958 | -0.211 | -0.210 | 0.993 |
| lh occipital GM | -0.231 | -0.090 | 0.826 | -0.288 | -0.110 | 0.978 |
| rh post. parahippocampal GM | -0.114 | -0.073 | 0.958 | -0.157 | -0.090 | 0.978 |
| lh post. parahippocampal GM | -0.056 | -0.110 | 0.958 | -0.125 | -0.133 | 0.993 |
| rh lat. occ.-temp. post. gyrus GM | -0.158 | -0.194 | 0.976 | -0.307 | -0.234 | 0.978 |
| lh lat. occ.-temp. post. gyrus GM | -0.038 | -0.085 | 0.958 | -0.136 | -0.171 | 0.978 |
| rh med.-inf. temp. post. gyrus GM | -0.302 | -0.303 | 0.997 | -0.409 | -0.294 | 0.978 |
| lh med.-inf. temp. post. gyrus GM | -0.276 | -0.171 | 0.881 | -0.285 | -0.243 | 0.978 |
| rh sup. temp. post. gyrus GM | -0.293 | -0.225 | 0.937 | -0.371 | -0.228 | 0.978 |
| lh sup. temp. post. gyrus GM | -0.195 | -0.295 | 0.881 | -0.213 | -0.367 | 0.978 |
| rh ant. cingulate gyrus GM | -0.167 | -0.137 | 0.983 | -0.074 | -0.139 | 0.978 |
| lh ant. cingulate gyrus GM | -0.221 | -0.058 | 0.813 | -0.081 | -0.064 | 0.984 |
| rh post. cingulate gyrus GM | -0.261 | -0.214 | 0.958 | -0.185 | -0.288 | 0.978 |
| lh post. cingulate gyrus GM | -0.305 | -0.126 | 0.753 | -0.327 | -0.200 | 0.978 |
| rh frontal GM | -0.299 | -0.256 | 0.958 | -0.489 | -0.424 | 0.978 |
| lh frontal GM | -0.236 | -0.222 | 0.991 | -0.411 | -0.384 | 0.978 |
| rh parietal GM | -0.593 | -0.493 | 0.881 | -0.594 | -0.501 | 0.978 |
| lh parietal GM | -0.469 | -0.453 | 0.991 | -0.545 | -0.558 | 0.987 |
| rh caudate nucleus | 0.454 | 0.244 | 0.736 | 0.458 | 0.255 | 0.978 |
| lh caudate nucleus | 0.500 | 0.268 | 0.688 | 0.465 | 0.281 | 0.978 |
| rh thalamus high T2 intensity | 0.084 | 0.231 | 0.826 | 0.085 | 0.270 | 0.978 |
| lh thalamus high T2 intensity | 0.071 | 0.272 | 0.736 | 0.096 | 0.403 | 0.658 |
| rh subthalamic nucleus | 0.041 | 0.232 | 0.736 | 0.094 | 0.192 | 0.978 |
| lh subthalamic nucleus | 0.083 | 0.359 | 0.480 | 0.107 | 0.267 | 0.978 |
| rh lentiform nucleus | -0.026 | 0.202 | 0.688 | -0.044 | 0.186 | 0.967 |
| lh lentiform nucleus | 0.143 | 0.331 | 0.736 | 0.161 | 0.300 | 0.978 |
| corpus callosum | 0.066 | 0.253 | 0.736 | 0.134 | 0.230 | 0.978 |
| lh ant. temp. med. WM | -0.070 | -0.166 | 0.881 | -0.139 | -0.220 | 0.978 |
| rh ant. temp. med. WM | -0.069 | -0.228 | 0.813 | -0.060 | -0.205 | 0.978 |
| lh ant. temp. lat. WM | -0.002 | -0.209 | 0.736 | -0.236 | -0.308 | 0.978 |
| rh ant. temp. lat. WM | -0.117 | -0.108 | 0.991 | -0.266 | -0.154 | 0.978 |
| lh ant. parahippocampal WM | 0.413 | 0.064 | 0.410 | 0.192 | 0.031 | 0.978 |
| rh ant. parahippocampal WM | 0.333 | 0.091 | 0.688 | 0.217 | 0.169 | 0.978 |
| lh sup. temp. middle gyrus WM | 0.243 | 0.102 | 0.826 | 0.257 | 0.136 | 0.978 |
| rh sup. temp. middle gyrus WM | 0.174 | 0.320 | 0.826 | 0.280 | 0.321 | 0.978 |
| lh med.-inf. temp. ant. gyrus WM | 0.099 | 0.186 | 0.897 | 0.060 | 0.178 | 0.978 |
| rh med.-inf. temp. ant. gyrus WM | -0.007 | 0.064 | 0.929 | 0.065 | 0.291 | 0.967 |
| lh lat. occ.-temp. ant. gyrus WM | 0.030 | -0.270 | 0.480 | -0.158 | -0.221 | 0.978 |
| rh lat. occ.-temp. ant. gyrus WM | 0.120 | 0.001 | 0.881 | -0.000 | 0.024 | 0.978 |
| rh insula WM | 0.664 | 0.307 | 0.410 | 0.761 | 0.270 | 0.083 |

| | | | | | | |
|---|---|---|---|---|---|---|
| lh insula WM | 0.630 | 0.233 | 0.410 | 0.730 | 0.189 | 0.055 |
| rh occipital WM | 0.454 | 0.170 | 0.480 | 0.464 | 0.210 | 0.947 |
| lh occipital WM | 0.224 | 0.224 | 0.997 | 0.382 | 0.416 | 0.978 |
| rh post. parahippocampal WM | 0.466 | 0.180 | 0.480 | 0.399 | 0.163 | 0.967 |
| lh post. parahippocampal WM | 0.242 | 0.112 | 0.858 | 0.119 | 0.167 | 0.978 |
| rh lat. occ.-temp. post. gyrus WM | 0.154 | 0.185 | 0.983 | 0.130 | 0.196 | 0.978 |
| lh lat. occ.-temp. post. gyrus WM | 0.318 | -0.033 | 0.410 | 0.308 | -0.061 | 0.432 |
| rh med.-inf. temp. post. gyrus WM | 0.318 | 0.245 | 0.924 | 0.439 | 0.436 | 0.993 |
| lh med.-inf. temp. post. gyrus WM | 0.107 | 0.275 | 0.813 | 0.372 | 0.470 | 0.978 |
| rh sup. temp. post. gyrus WM | -0.033 | 0.008 | 0.958 | 0.046 | 0.074 | 0.978 |
| lh sup. temp. post. gyrus WM | 0.176 | -0.024 | 0.736 | 0.151 | -0.032 | 0.978 |
| rh ant. cingulate gyrus WM | 0.253 | 0.022 | 0.688 | 0.371 | 0.022 | 0.483 |
| lh ant. cingulate gyrus WM | 0.226 | 0.005 | 0.713 | 0.263 | -0.006 | 0.863 |
| rh post. cingulate gyrus WM | 0.111 | 0.006 | 0.881 | 0.170 | -0.117 | 0.769 |
| lh post. cingulate gyrus WM | 0.209 | 0.065 | 0.826 | 0.133 | -0.009 | 0.978 |
| rh frontal WM | 0.279 | 0.265 | 0.991 | 0.371 | 0.344 | 0.978 |
| lh frontal WM | 0.297 | 0.300 | 0.997 | 0.423 | 0.377 | 0.978 |
| rh parietal WM | 0.056 | 0.084 | 0.983 | 0.234 | 0.268 | 0.978 |
| lh parietal WM | 0.111 | 0.128 | 0.991 | 0.298 | 0.299 | 0.993 |
| rh thalamus low T2 intensity | -0.396 | -0.019 | 0.410 | -0.474 | -0.085 | 0.407 |
| lh thalamus low T2 intensity | -0.220 | 0.121 | 0.410 | -0.286 | -0.043 | 0.967 |
| rh claustrum | infinity | infinity | - | 1.141 | 1.054 | 0.978 |
| lh claustrum | 1.141 | 1.054 | 0.897 | infinity | infinity | - |

*The Pearson's correlation coefficients r for right and left claustrum were transformed to z-scores by Fisher transformation. The z-scores of preterm- and term-born neonates were compared for significant differences. There was no significant difference after false discovery rate correction for multiple testing (p_FDR < 0.05). Table reproduced from the Online Supplement of Neubauer et al. (2023), used under CC By. Ant. = anterior, cla = claustrum, FT = full term, GM = gray matter, inf. = inferior, lat. = lateral, lh = left hemisphere, med. = medial, occ. = occipital, post. = posterior, PT = preterm, rh = right hemisphere, sup. = superior, temp. = temporal, WM = white matter.*

***Table B3: Claustrum covariance with other brain regions regarding the mean diffusivity.***

| Region | PT (right cla) | FT (right cla) | p_FDR (right cla) | PT (left cla) | FT (left cla) | p_FDR (left cla) |
|---|---|---|---|---|---|---|
| lh hippocampus | 0.741 | 0.773 | 0.850 | 0.892 | 0.897 | 0.977 |
| rh hippocampus | 0.564 | 0.791 | 0.213 | 0.447 | 0.738 | 0.167 |
| lh amygdala | 0.614 | 1.068 | 0.030* | 0.741 | 1.132 | 0.068 |
| rh amygdala | 0.666 | 0.806 | 0.426 | 0.622 | 0.734 | 0.540 |
| lh ant. temp. med. GM | 0.397 | 0.669 | 0.140 | 0.507 | 0.757 | 0.239 |
| rh ant. temp. med. GM | 0.386 | 0.593 | 0.252 | 0.451 | 0.638 | 0.309 |
| lh ant. temp. lat. GM | 0.134 | 0.313 | 0.314 | 0.206 | 0.439 | 0.244 |
| rh ant. temp. lat. GM | 0.216 | 0.327 | 0.526 | 0.097 | 0.280 | 0.320 |
| lh ant. parahippocampal GM | 0.662 | 0.930 | 0.141 | 0.719 | 0.946 | 0.244 |
| rh ant. parahippocampal GM | 0.428 | 0.739 | 0.098 | 0.508 | 0.823 | 0.152 |

| | | | | | | |
|---|---|---|---|---|---|---|
| lh sup. temp. middle gyrus GM | -0.088 | 0.317 | 0.045* | -0.125 | 0.353 | 0.027* |
| rh sup. temp. middle gyrus GM | -0.132 | 0.193 | 0.084 | -0.156 | 0.200 | 0.109 |
| lh med.-inf. temp. ant. gyrus GM | 0.042 | 0.222 | 0.314 | 0.031 | 0.233 | 0.285 |
| rh med.-inf. temp. ant. gyrus GM | 0.032 | 0.108 | 0.655 | -0.030 | 0.067 | 0.601 |
| lh lat. occ.-temp. ant. gyrus GM | 0.479 | 0.749 | 0.140 | 0.541 | 0.721 | 0.327 |
| rh lat. occ.-temp. ant. gyrus GM | 0.244 | 0.609 | 0.070 | 0.235 | 0.656 | 0.055 |
| lh cerebellum | 0.589 | 0.740 | 0.394 | 0.650 | 0.878 | 0.244 |
| rh cerebellum | 0.507 | 0.693 | 0.302 | 0.575 | 0.856 | 0.174 |
| brainstem | 0.558 | 0.772 | 0.237 | 0.635 | 0.864 | 0.244 |
| rh insula GM | 0.391 | 0.515 | 0.476 | 0.241 | 0.440 | 0.285 |
| lh insula GM | 0.187 | 0.517 | 0.082 | 0.250 | 0.556 | 0.155 |
| rh occipital GM | -0.100 | 0.262 | 0.070 | -0.058 | 0.250 | 0.154 |
| lh occipital GM | -0.063 | 0.286 | 0.071 | -0.064 | 0.245 | 0.154 |
| rh post. parahippocampal GM | -0.027 | 0.327 | 0.071 | -0.004 | 0.338 | 0.122 |
| lh post. parahippocampal GM | 0.050 | 0.341 | 0.118 | 0.095 | 0.399 | 0.155 |
| rh lat. occ.-temp. post. gyrus GM | -0.047 | 0.351 | 0.045* | -0.039 | 0.311 | 0.112 |
| lh lat. occ.-temp. post. gyrus GM | 0.316 | 0.423 | 0.535 | 0.411 | 0.429 | 0.922 |
| rh med.-inf. temp. post. gyrus GM | -0.239 | -0.011 | 0.212 | -0.247 | -0.051 | 0.288 |
| lh med.-inf. temp. post. gyrus GM | -0.171 | 0.237 | 0.045* | -0.204 | 0.193 | 0.067 |
| rh sup. temp. post. gyrus GM | -0.305 | -0.005 | 0.106 | -0.283 | -0.009 | 0.182 |
| lh sup. temp. post. gyrus GM | -0.250 | 0.240 | 0.023* | -0.273 | 0.234 | 0.024* |
| rh ant. cingulate gyrus GM | -0.030 | 0.604 | 0.003* | -0.011 | 0.637 | 0.004* |
| lh ant. cingulate gyrus GM | -0.074 | 0.552 | 0.003* | -0.000 | 0.579 | 0.011* |
| rh post. cingulate gyrus GM | -0.271 | 0.215 | 0.023* | -0.250 | 0.195 | 0.039* |
| lh post. cingulate gyrus GM | -0.328 | 0.171 | 0.023* | -0.327 | 0.146 | 0.027* |
| rh frontal GM | -0.067 | 0.383 | 0.030* | -0.105 | 0.357 | 0.030* |
| lh frontal GM | -0.104 | 0.378 | 0.023* | -0.074 | 0.402 | 0.027* |
| rh parietal GM | -0.187 | 0.180 | 0.070 | -0.174 | 0.154 | 0.139 |
| lh parietal GM | -0.224 | 0.229 | 0.030* | -0.227 | 0.190 | 0.055 |
| rh caudate nucleus | 0.839 | 1.113 | 0.138 | 0.823 | 1.121 | 0.159 |
| lh caudate nucleus | 0.746 | 1.156 | 0.045* | 0.812 | 1.223 | 0.055 |
| rh thalamus high T2 intensity | 0.902 | 1.051 | 0.394 | 0.976 | 1.023 | 0.821 |
| lh thalamus high T2 intensity | 0.765 | 1.066 | 0.106 | 0.812 | 1.046 | 0.244 |
| rh subthalamic nucleus | 0.382 | 0.890 | 0.023* | 0.420 | 0.899 | 0.027* |
| lh subthalamic nucleus | 0.250 | 0.855 | 0.004* | 0.266 | 0.807 | 0.018* |
| rh lentiform nucleus | 1.149 | 1.353 | 0.255 | 0.907 | 1.115 | 0.273 |
| lh lentiform nucleus | 0.948 | 1.235 | 0.118 | 1.132 | 1.304 | 0.340 |
| corpus callosum | 0.386 | 0.817 | 0.036* | 0.500 | 0.822 | 0.143 |
| lh ant. temp. med. WM | 0.596 | 0.994 | 0.045* | 0.730 | 1.066 | 0.129 |
| rh ant. temp. med. WM | 0.633 | 0.820 | 0.302 | 0.638 | 0.812 | 0.337 |
| lh ant. temp. lat. WM | 0.613 | 0.842 | 0.212 | 0.723 | 0.901 | 0.330 |
| rh ant. temp. lat. WM | 0.623 | 0.710 | 0.611 | 0.543 | 0.627 | 0.654 |
| lh ant. parahippocampal WM | 0.879 | 0.977 | 0.568 | 1.121 | 1.089 | 0.880 |
| rh ant. parahippocampal WM | 0.713 | 0.886 | 0.332 | 0.703 | 0.921 | 0.247 |
| lh sup. temp. middle gyrus WM | 0.711 | 1.084 | 0.067 | 0.940 | 1.163 | 0.247 |
| rh sup. temp. middle gyrus WM | 0.889 | 1.176 | 0.118 | 0.842 | 1.088 | 0.240 |

| | | | | | | |
|---|---|---|---|---|---|---|
| lh med.-inf. temp. ant. gyrus WM | 0.587 | 0.939 | 0.071 | 0.774 | 1.021 | 0.240 |
| rh med.-inf. temp. ant. gyrus WM | 0.675 | 0.932 | 0.159 | 0.537 | 0.827 | 0.167 |
| lh lat. occ.-temp. ant. gyrus WM | 0.729 | 1.078 | 0.071 | 0.863 | 1.094 | 0.244 |
| rh lat. occ.-temp. ant. gyrus WM | 0.642 | 1.072 | 0.036* | 0.593 | 1.007 | 0.055 |
| rh insula WM | 1.545 | 1.695 | 0.394 | 1.140 | 1.360 | 0.247 |
| lh insula WM | 1.079 | 1.403 | 0.084 | 1.642 | 1.620 | 0.906 |
| rh occipital WM | 0.676 | 1.018 | 0.077 | 0.810 | 1.036 | 0.245 |
| lh occipital WM | 0.684 | 0.994 | 0.099 | 0.844 | 0.986 | 0.428 |
| rh post. parahippocampal WM | 0.682 | 0.914 | 0.212 | 0.684 | 0.967 | 0.174 |
| lh post. parahippocampal WM | 0.668 | 0.833 | 0.355 | 0.841 | 1.008 | 0.352 |
| rh lat. occ.-temp. post. gyrus WM | 0.789 | 1.076 | 0.118 | 0.717 | 0.993 | 0.182 |
| lh lat. occ.-temp. post. gyrus WM | 0.693 | 1.055 | 0.070 | 0.902 | 1.122 | 0.247 |
| rh med.-inf. temp. post. gyrus WM | 0.718 | 1.047 | 0.082 | 0.669 | 0.903 | 0.244 |
| lh med.-inf. temp. post. gyrus WM | 0.581 | 0.999 | 0.042* | 0.780 | 1.014 | 0.244 |
| rh sup. temp. post. gyrus WM | 0.637 | 0.763 | 0.473 | 0.654 | 0.683 | 0.887 |
| lh sup. temp. post. gyrus WM | 0.433 | 0.989 | 0.010* | 0.611 | 1.000 | 0.068 |
| rh ant. cingulate gyrus WM | 0.606 | 0.956 | 0.071 | 0.658 | 0.897 | 0.244 |
| lh ant. cingulate gyrus WM | 0.435 | 0.775 | 0.077 | 0.682 | 0.900 | 0.247 |
| rh post. cingulate gyrus WM | 0.536 | 0.890 | 0.071 | 0.531 | 0.853 | 0.143 |
| lh post. cingulate gyrus WM | 0.411 | 0.811 | 0.045* | 0.611 | 0.896 | 0.173 |
| rh frontal WM | 0.907 | 1.168 | 0.152 | 0.892 | 1.057 | 0.353 |
| lh frontal WM | 0.688 | 1.126 | 0.035* | 0.912 | 1.103 | 0.301 |
| rh parietal WM | 0.566 | 0.902 | 0.079 | 0.618 | 0.818 | 0.285 |
| lh parietal WM | 0.581 | 0.916 | 0.079 | 0.756 | 0.905 | 0.406 |
| rh thalamus low T2 intensity | 0.729 | 0.946 | 0.234 | 0.709 | 0.977 | 0.192 |
| lh thalamus low T2 intensity | 0.422 | 0.875 | 0.030* | 0.410 | 0.939 | 0.018* |
| rh claustrum | infinity | infinity | - | 1.233 | 1.533 | 0.157 |
| lh claustrum | 1.233 | 1.533 | 0.106 | infinity | infinity | - |

*The Pearson's correlation coefficients r for right and left claustrum were transformed to z-scores by Fisher transformation. The z-scores of preterm- and term-born neonates were compared for significant differences. The significant differences after false discovery rate correction for multiple testing (p_FDR < 0.05) are marked with an asterisk. Table reproduced from the Online Supplement of Neubauer et al. (2023), used under CC By. Ant. = anterior, cla = claustrum, FT = full term, GM = gray matter, inf. = inferior, lat. = lateral, lh = left hemisphere, med. = medial, occ. = occipital, post. = posterior, PT = preterm, rh = right hemisphere, sup. = superior, temp. = temporal, WM = white matter.*

***Table B4: Claustrum covariance with other brain regions regarding the fractional anisotropy.***

| Region | PT (right cla) | FT (right cla) | p_FDR (right cla) | PT (left cla) | FT (left cla) | p_FDR (left cla) |
|---|---|---|---|---|---|---|
| lh hippocampus | 0.628 | 0.089 | 0.006* | 0.721 | 0.147 | 0.022* |
| rh hippocampus | 0.795 | 0.217 | 0.006* | 0.801 | 0.272 | 0.024* |
| lh amygdala | 0.568 | 0.047 | 0.007* | 0.581 | 0.119 | 0.044* |
| rh amygdala | 0.703 | 0.163 | 0.006* | 0.723 | 0.314 | 0.053 |

| | | | | | | |
|---|---|---|---|---|---|---|
| lh ant. temp. med. GM | 0.769 | 0.291 | 0.013* | 0.693 | 0.424 | 0.221 |
| rh ant. temp. med. GM | 0.736 | 0.262 | 0.013* | 0.748 | 0.307 | 0.047* |
| lh ant. temp. lat. GM | 0.611 | 0.148 | 0.015* | 0.552 | 0.184 | 0.082 |
| rh ant. temp. lat. GM | 0.620 | 0.143 | 0.013* | 0.578 | 0.126 | 0.047* |
| lh ant. parahippocampal GM | 0.943 | 0.243 | 0.001* | 0.972 | 0.421 | 0.022* |
| rh ant. parahippocampal GM | 0.870 | 0.435 | 0.023* | 0.966 | 0.580 | 0.068 |
| lh sup. temp. middle gyrus GM | 0.646 | 0.101 | 0.006* | 0.613 | 0.191 | 0.053 |
| rh sup. temp. middle gyrus GM | 0.669 | 0.089 | 0.006* | 0.605 | 0.142 | 0.044* |
| lh med.-inf. temp. ant. gyrus GM | 0.388 | 0.011 | 0.046* | 0.325 | 0.018 | 0.161 |
| rh med.-inf. temp. ant. gyrus GM | 0.441 | -0.106 | 0.006* | 0.423 | -0.091 | 0.025* |
| lh lat. occ.-temp. ant. gyrus GM | 0.423 | 0.061 | 0.054 | 0.319 | 0.098 | 0.333 |
| rh lat. occ.-temp. ant. gyrus GM | 0.444 | 0.216 | 0.237 | 0.380 | 0.184 | 0.337 |
| lh cerebellum | 0.656 | 0.354 | 0.118 | 0.665 | 0.346 | 0.141 |
| rh cerebellum | 0.569 | 0.332 | 0.224 | 0.634 | 0.400 | 0.292 |
| brainstem | 1.083 | 0.562 | 0.007* | 1.068 | 0.659 | 0.053 |
| rh insula GM | 0.835 | 0.278 | 0.006* | 0.677 | 0.300 | 0.075 |
| lh insula GM | 0.781 | 0.323 | 0.016* | 0.865 | 0.454 | 0.053 |
| rh occipital GM | 0.587 | 0.105 | 0.013* | 0.606 | 0.204 | 0.055 |
| lh occipital GM | 0.575 | 0.156 | 0.026* | 0.531 | 0.226 | 0.161 |
| rh post. parahippocampal GM | 0.654 | 0.180 | 0.013* | 0.651 | 0.290 | 0.082 |
| lh post. parahippocampal GM | 0.638 | 0.219 | 0.026* | 0.581 | 0.376 | 0.337 |
| rh lat. occ.-temp. post. gyrus GM | 0.574 | 0.261 | 0.103 | 0.506 | 0.329 | 0.365 |
| lh lat. occ.-temp. post. gyrus GM | 0.602 | 0.180 | 0.026* | 0.513 | 0.329 | 0.353 |
| rh med.-inf. temp. post. gyrus GM | 0.488 | -0.001 | 0.012* | 0.438 | 0.038 | 0.055 |
| lh med.-inf. temp. post. gyrus GM | 0.446 | 0.064 | 0.044* | 0.420 | 0.137 | 0.208 |
| rh sup. temp. post. gyrus GM | 0.469 | 0.039 | 0.024* | 0.456 | 0.127 | 0.127 |
| lh sup. temp. post. gyrus GM | 0.539 | 0.104 | 0.023* | 0.537 | 0.173 | 0.082 |
| rh ant. cingulate gyrus GM | 0.723 | 0.438 | 0.138 | 0.796 | 0.577 | 0.333 |
| lh ant. cingulate gyrus GM | 0.754 | 0.511 | 0.214 | 0.789 | 0.548 | 0.273 |
| rh post. cingulate gyrus GM | 0.266 | -0.009 | 0.151 | 0.295 | 0.099 | 0.337 |
| lh post. cingulate gyrus GM | 0.364 | 0.001 | 0.054 | 0.278 | 0.088 | 0.340 |
| rh frontal GM | 0.698 | 0.331 | 0.052 | 0.667 | 0.418 | 0.256 |
| lh frontal GM | 0.681 | 0.333 | 0.066 | 0.688 | 0.420 | 0.221 |
| rh parietal GM | 0.552 | -0.003 | 0.006* | 0.542 | 0.100 | 0.047* |
| lh parietal GM | 0.556 | 0.033 | 0.007* | 0.524 | 0.106 | 0.053 |
| rh caudate nucleus | 0.686 | 0.780 | 0.635 | 0.827 | 0.743 | 0.682 |
| lh caudate nucleus | 0.786 | 0.755 | 0.895 | 0.759 | 0.597 | 0.420 |
| rh thalamus high T2 intensity | 0.674 | 0.503 | 0.376 | 0.778 | 0.485 | 0.186 |
| lh thalamus high T2 intensity | 0.729 | 0.577 | 0.445 | 0.636 | 0.492 | 0.469 |
| rh subthalamic nucleus | 0.797 | 0.378 | 0.026* | 0.831 | 0.469 | 0.082 |
| lh subthalamic nucleus | 0.761 | 0.461 | 0.119 | 0.590 | 0.380 | 0.337 |
| rh lentiform nucleus | 1.141 | 0.587 | 0.006* | 0.970 | 0.553 | 0.053 |
| lh lentiform nucleus | 0.907 | 0.588 | 0.097 | 1.066 | 0.798 | 0.221 |
| corpus callosum | 0.751 | 0.485 | 0.166 | 0.733 | 0.527 | 0.337 |
| lh ant. temp. med. WM | 0.682 | 0.725 | 0.862 | 0.765 | 0.832 | 0.727 |
| rh ant. temp. med. WM | 0.756 | 0.705 | 0.857 | 0.830 | 0.777 | 0.794 |

| | | | | | | |
|---|---|---|---|---|---|---|
| lh ant. temp. lat. WM | 0.707 | 0.595 | 0.579 | 0.765 | 0.690 | 0.696 |
| rh ant. temp. lat. WM | 0.635 | 0.599 | 0.891 | 0.781 | 0.589 | 0.340 |
| lh ant. parahippocampal WM | 0.868 | 0.574 | 0.126 | 1.059 | 0.778 | 0.209 |
| rh ant. parahippocampal WM | 1.063 | 0.654 | 0.030* | 1.172 | 0.695 | 0.044* |
| lh sup. temp. middle gyrus WM | 0.948 | 0.740 | 0.274 | 1.083 | 0.868 | 0.335 |
| rh sup. temp. middle gyrus WM | 1.120 | 0.836 | 0.138 | 0.967 | 0.768 | 0.337 |
| lh med.-inf. temp. ant. gyrus WM | 0.805 | 0.813 | 0.959 | 0.880 | 0.862 | 0.918 |
| rh med.-inf. temp. ant. gyrus WM | 0.804 | 0.707 | 0.634 | 0.871 | 0.671 | 0.337 |
| lh lat. occ.-temp. ant. gyrus WM | 0.674 | 0.660 | 0.949 | 0.689 | 0.642 | 0.810 |
| rh lat. occ.-temp. ant. gyrus WM | 0.683 | 0.705 | 0.929 | 0.733 | 0.649 | 0.682 |
| rh insula WM | 1.718 | 1.340 | 0.046* | 1.160 | 1.062 | 0.635 |
| lh insula WM | 1.019 | 1.037 | 0.943 | 1.592 | 1.342 | 0.256 |
| rh occipital WM | 0.999 | 0.787 | 0.268 | 1.046 | 0.913 | 0.505 |
| lh occipital WM | 1.004 | 0.772 | 0.231 | 1.063 | 0.914 | 0.464 |
| rh post. parahippocampal WM | 0.927 | 0.601 | 0.088 | 0.937 | 0.748 | 0.340 |
| lh post. parahippocampal WM | 0.775 | 0.633 | 0.479 | 0.915 | 0.766 | 0.464 |
| rh lat. occ.-temp. post. gyrus WM | 0.917 | 0.706 | 0.269 | 0.788 | 0.642 | 0.465 |
| lh lat. occ.-temp. post. gyrus WM | 0.927 | 0.746 | 0.360 | 0.953 | 0.770 | 0.353 |
| rh med.-inf. temp. post. gyrus WM | 0.968 | 0.746 | 0.248 | 0.853 | 0.721 | 0.505 |
| lh med.-inf. temp. post. gyrus WM | 0.803 | 0.794 | 0.959 | 0.893 | 0.762 | 0.505 |
| rh sup. temp. post. gyrus WM | 0.848 | 0.707 | 0.479 | 0.770 | 0.673 | 0.635 |
| lh sup. temp. post. gyrus WM | 0.761 | 0.621 | 0.479 | 0.799 | 0.718 | 0.687 |
| rh ant. cingulate gyrus WM | 1.012 | 0.613 | 0.035* | 0.901 | 0.652 | 0.256 |
| lh ant. cingulate gyrus WM | 0.955 | 0.727 | 0.237 | 1.027 | 0.837 | 0.340 |
| rh post. cingulate gyrus WM | 0.740 | 0.643 | 0.634 | 0.713 | 0.690 | 0.918 |
| lh post. cingulate gyrus WM | 0.769 | 0.651 | 0.563 | 0.860 | 0.662 | 0.337 |
| rh frontal WM | 1.067 | 1.021 | 0.862 | 1.016 | 0.908 | 0.597 |
| lh frontal WM | 0.986 | 0.954 | 0.895 | 1.017 | 0.940 | 0.696 |
| rh parietal WM | 0.949 | 0.687 | 0.172 | 0.923 | 0.707 | 0.333 |
| lh parietal WM | 0.879 | 0.704 | 0.367 | 0.937 | 0.734 | 0.337 |
| rh thalamus low T2 intensity | 0.371 | 0.094 | 0.151 | 0.514 | 0.157 | 0.085 |
| lh thalamus low T2 intensity | 0.501 | 0.323 | 0.361 | 0.316 | 0.202 | 0.577 |
| rh claustrum | infinity | infinity | - | 1.237 | 1.192 | 0.815 |
| lh claustrum | 1.237 | 1.192 | 0.862 | infinity | infinity | - |

*The Pearson's correlation coefficients r for right and left claustrum were transformed to z-scores by Fisher transformation. The z-scores of preterm- and term-born neonates were compared for significant differences. The significant differences after false discovery rate correction for multiple testing (p_FDR < 0.05) are marked with an asterisk. Table reproduced from the Online Supplement of Neubauer et al. (2023), used under CC By. Ant. = anterior, cla = claustrum, FT = full term, GM = gray matter, inf. = inferior, lat. = lateral, lh = left hemisphere, med. = medial, occ. = occipital, post. = posterior, PT = preterm, rh = right hemisphere, sup. = superior, temp. = temporal, WM = white matter.*

## Acknowledgment

Firstly, I wish to show my appreciation to Prof. Dr. med. Claus Zimmer, head of the Department for Diagnostic and Interventional Neuroradiology at Klinikum rechts der Isar for the generous support and for facilitating this project.

Special thanks should be given to my supervisor PD Dr. med. Christian Sorg for his supervision and constant encouragement, I learned a lot professionally and personally. Furthermore, the personal advice provided by my mentor Dr. Dr. med. Felix Brandl was greatly appreciated. I am also grateful to PD Dr. med. Dennis Hedderich for his introduction to artificial intelligence and comprehensive support. I would like to thank Dr. Hongwei Bran Li for his openness and cooperation which enabled this research, and all my colleagues who have helped me along the way.

Data were provided by the developing Human Connectome Project, KCL-Imperial-Oxford Consortium funded by the European Research Council under the European Union Seventh Framework Programme (FP/2007-2013) / ERC Grant Agreement no. [319456]. I am grateful to the families who generously supported this trial.

Finally, I wish to thank my family for their support and encouragement throughout my study and beyond.

## Publications related to this thesis

Antonia Neubauer*, Hongwei Bran Li*, Jil Wendt, Benita Schmitz-Koep, Aurore Menegaux, David Schinz, Bjoern Menze, Claus Zimmer, Christian Sorg, Dennis M. Hedderich (2022).
**Efficient Claustrum Segmentation in T2-weighted Neonatal Brain MRI Using Transfer Learning from Adult Scans.**
Clinical Neuroradiology, 32, 665-676. https://doi.org/10.1007/s00062-021-01137-8
(*Equal contribution to first authorship.)

Antonia Neubauer, Aurore Menegaux, Jil Wendt, Hongwei Bran Li, Benita Schmitz-Koep, Tobias Ruzok, Melissa Thalhammer, David Schinz, Peter Bartmann, Dieter Wolke, Josef Priller, Claus Zimmer, Daniel Rueckert, Dennis M. Hedderich**, Christian Sorg** (2023).
**Aberrant claustrum structure in preterm-born neonates: An MRI study.**
NeuroImage: Clinical. 37, 103286. https://doi.org/10.1016/j.nicl.2022.103286
(**Equal contribution to senior authorship.)